PATHIRAJA, GAYANI CHATHURIKA. Ph.D. Mechanism and in-situ crystal growth kinetics of ultrathin binary transition metal hydroxide/oxide nanowire self-assembly. (2021)
Directed by Dr. Hemali Rathnayake and Dr. Daniel Herr. 125 pp.

The controlled synthesis of anisotropic one-dimensional metal hydroxide/oxide nanostructures with versatile properties, are most fascinating for applications in electronics, optical, and energy storage devices, due to their superior performance based on quantum confinement and nanoscale size effects. However, the in-depth investigation of their corresponding crystal growth mechanism and kinetics have yet to be clearly understood to tailor their properties for a specific application. Towards this goal, the first part of this dissertation focuses on investigating the nanocrystal growth mechanism and kinetics in a sol-gel colloidal system to make ultrathin metal hydroxide/oxide nanowires. The second part of the project explore the self-assembly pathways to make bionanomaterial of metal hydroxide nanowires with phospholipids. Utilizing base-catalyzed hydrolysis followed by the directed self-assembly and crystal growth of nanocrystals, a novel, facile and environmentally benign sol-gel approach was developed to make ultrathin $Cu(OH)_2$ nanowires. During the subsequent post-annealing process, the $Cu(OH)_2$ nanowires transformed into CuO nanowires. We captured step by step crystal growth process at each stage of the sol-gel process using HR-TEM and optical changes at each stage of the sol-gel process was also examined by UV-visible spectroscopy. We identified an Oriented Attachment (OA) mechanism as the dominant crystal growth process of ultrathin $Cu(OH)_2$ nanowire fabrication using this surfactant free, one-pot sol-gel route. Then, we proposed a new kinetic model for OA-directed crystal growth correlating the chemical reaction kinetics of the stages of sol-gel process for the sol-gel synthesis of $Cu(OH)_2$ nanowire formation. The chemical kinetic model follows the sigmoidal second order growth kinetic for the hydrolysis and condensation process and the sigmoidal zeroth order growth kinetic for the polycondensation step respectively. The $Cu(OH)_2$-decorated bioinspired supramolecular nanowires were fabricated via the developed sol-gel method in the presence of a zwitterionic

phospholipid as a surfactant in $H_2O/CHCl_3$ solvent system. We identified OA-directed controlled crystal growth of synthesized nanowires using HR-TEM and single crystallinity using Fast Fourier Transform analysis. Then powder XRD pattern shows that the prominent crystal growth plane of supramolecular nanowires is [020] due to the preferential adsorption of phospholipids. In conclusion, we fabricated ultrathin $Cu(OH)_2$ nanowires without any surfactants by introducing novel Sigmoidal kinetic models that considers the directed growth of the length. $Cu(OH)_2$-decorated bioinspired supramolecular ultrathin nanowires was also fabricated with the presence of phospholipids using the greener and facile sol-gel route. This research lays the fundamental understanding, which enables the creation of guiding principles that drive the nanocrystal growth of size-and shape-controlled anisotropic metal hydroxides/oxides and bioinspired supramolecular nanowires for potential applications.

MECHANISM AND IN-SITU CRYSTAL GROWTH KINETICS OF ULTRATHIN BINARY TRANSITION METAL HYDROXIDE/OXIDE NANOWIRE SELF-ASSEMBLY

by

Gayani Chathurika Pathiraja

A Dissertation

Submitted to

the Faculty of The Graduate School at

The University of North Carolina at Greensboro

in Partial Fulfillment

of the Requirements for the Degree

Doctor of Philosophy

Greensboro

2021

Approved by

Dr. Hemali Rathnayake
Committee Co-Chair

Dr. Daniel Herr
Committee Co-Chair

APPROVAL PAGE

This dissertation written by GAYANI CHATHURIKA PATHIRAJA, has been approved by the following committee of the Faculty of The Graduate School at The University of North Carolina at Greensboro.

Committee Co-Chair

Dr. Hemali Rathnayake

Committee Co-Chair

Dr. Daniel Herr

Committee Members

Dr. Tetyana Ignatova

Dr. Jeffrey R. Alston

October 27, 2021
Date of Acceptance by Committee

October 27, 2021
Date of Final Oral Examination

ACKNOWLEDGEMENTS

There are many people I need to express my gratitude for providing me their support, guidance, and love during my PhD. First, I would like to sincerely thank my advisors, Dr. Hemali Rathnayake and Dr. Daniel Herr, for their guidance and support that they have given me over past four years. I'm very blessed to have them and their continuous motivation and guidance was incredible. Both of my advisors introduced me to their unique fields of research and helped me in many ways to make my own humble contributions. I feel honored to have worked with them during my PhD and without their advice and continuous encouragement, I would not come this far in my graduate life. I am also grateful to my committee members, Dr. Jeffrey R. Alston, and Dr. Tetyana Ignatova for their interest, inputs, and evaluating of my work.

I would like to acknowledge the financial support for my doctoral studies provided by the Joint School of Nanoscience and Nano engineering (JSNN), collaboration between the University of North Carolina Greensboro and North Carolina A&T State University. I want to extend my thanks to the staff at JSNN for their training, and equipment troubleshooting, particularly Dr. Kyle Nowlin and Dr. Olubunmi Ayodele. Thank you to all my wonderful current and past group members especially Dr. Klinton Davis for providing training on TEM.

Finally, this accomplishment would not have happened without the love of my friends and family. I'm thankful to my friends and peers around me who helped me various ways and making an enjoyable environment. I'm especially grateful to my parents who encouraged me to do higher studies and thank you for being by my side in my every moment. Many thanks to my husband, Manoj provided me incredible support, dedication, unconditional love, and patience throughout these years and to my son, Vethmin, thank you for being the light of my life.

TABLE OF CONTENTS

LIST OF TABLES

LIST OF FIGURES

CHAPTER I: INTRODUCTION

1.1 Overview

The tailoring functional materials, with controlled sizes and morphologies, plays a major role in the growing demand for miniaturized devices.[1,2] For example, recent breakthroughs have enabled the production of ultrathin semiconductor wires.[1] However, the understanding the guiding principles that control the size and shape of a material are necessary to achieve materials with nanoscale precision. Therefore, mechanistic, and kinetic studies of crystal growth are important to tailor these materials with controlled sizes and morphologies and to design functional supramolecular structures for miniature devices. Ostwald ripening (OR) and oriented attachment (OA) represent two reported crystal growth mechanisms proposed to explain solution-based procedures. In colloidal solutions, the formation of metal and metal hydroxide/oxide microstructures is often explained by OR theory. Under OR conditions, crystal growth is controlled by diffusion, where larger particles grow at the expense of smaller particles.[2–4] However, at the nanoscale, the OR mechanism often is not supported by the reported crystal growth of nanomaterials.[5] Oriented attachment (OA), an alternative mechanism, has introduced to better describe aggregation-based crystal growth at the nanoscale. It is the self-assembly of nanocrystals to form a secondary crystal by sharing a common crystallographic orientation.[6,7] This OA-based crystal growth was first described in 1998 for hydrothermally synthesized TiO_2 nanocrystals.[6] This mechanism asserts to explain the formation of various nanostructures including zero-, one-, two-, and three- dimensional nanoscale morphologies of various materials. Transition metal hydroxide/oxide nanowires represent a promising class of materials for many applications, due to their fascinating physical and chemical properties such as electrical, optical, catalytic, and electrochemical properties.[8–11] For many of these systems, the OA mechanism helps to inform effective approaches to prepare size and shape-controlled anisotropic transition metal oxide 1 D nanostructures. OA-based crystal growth is driven by a

thermodynamic reduction in the surface energy of crystal facets.[6,12] The ability to fabricate high purity, crystalline nanomaterials by controlling diameter, length, composition, and crystal structure enabled remarkable success high impact applications in electronic, optical, electrochemical, biological, and energy devices.[13]

The preferential adsorption of soluble organic biomolecules on crystal facets can affect the total crystal surface energy in OA-based crystal growth.[14] Specific biomolecules such as proteins, proteolipids, phospholipids, collagen, and carbohydrates can influence the nucleation, growth, the size, and the orientation of crystals, acting as a surfactant.[15] By mimicking nature, the biomimetic synthesis of transition metal hydroxide/oxide nanowires, via directed self-assembly, have been reported. However, the cost-effective controlled synthesis of ultrathin semiconductor nanowires remains in its preliminary stage. The design of greener and more facile methods for preparing ultrathin, 1D bioinspired metal oxide nanowires with high crystallinity, and reproducibility are greatly needed. A key challenge is the lack of understanding regarding nucleation and crystal growth processes and kinetics for the development of morphology-controlled metal hydroxide/oxide nanowires. Additionally, the design of robust functional nanomaterials requires a foundational understanding of the interaction and selectivity between biomolecules and nanocrystal surfaces during the crystallization process. Such knowledge would help to control the anisotropy and enable further progress towards the scalable fabrication of ultrathin nanowires. As a result, nanostructure morphology could be predicted in the controlled crystallization reaction, which remains a major challenge even with computational modeling.[16]

The existing crystal growth kinetic models help to explain the crystal growth of nanoparticles based on the temporal changes in particle diameter changes.[5] However, these kinetic models cannot explain the crystal growth of one-dimensional nanostructures along certain specific direction. The OA- based elongation kinetics of 1D nanostructures, particularly in the presence of surfactants, represents a key knowledge gap. Therefore, kinetic studies of OA-

directed crystal growth processes will help to address this gap and guide the preparation of size and shape controlled 1D nanostructures.

1.2 Transition metal hydroxide/oxide nanowires

Transition metal oxides are comprised of transition metals and oxygen having ionic–covalent character.[17] They offer very diverse and fascinating physical and chemical properties, which arise from the outer *d* electrons of the transition metal ions.[18] Many transition metals can form a variety of binary oxides with an empirical formula of M_xO_y. Transition metal oxide properties, such as electrical conductivity, can vary widely depending on the metal. The transition metal oxide insulators include CaO, NiO, TiO_2, semiconducting materials include FeO, ZnO, CuO, and TiO, NbO, CrO_2, ReO_3 exhibit metallic properties respectively[19]. Every *3d* transition metal monoxides are widely used in different applications, due to their abundance and low cost compared to *4d* and *5d* transition metal oxides.

Synthesis of transition metal oxide nanowires and nanorods have been reported using different wet chemical synthesis methods. For example, Yang et al summarized recent efforts to control synthesis of metal oxide and hydroxide nanowires/rods/arrays, such as NiO nanorods and Co_3O_4 nanowires, via a hydrothermal route to high performance electrochemical electrodes and catalysts.[20] Another wet chemical synthesis method demonstrated the fabrication of ZnO nanorods, with diameters of ~15 nm by an oriented attachment mechanism.[21] Very recently, our group reported a versatile sol–gel synthesis, combined with a solvothermal process, to make ZnO nanorods for optoelectronic devices.[22] Furthermore, Chaurasiya et al. synthesized TiO_2 nanorods using a wet chemical method for photovoltaic and humidity sensing applications[23]. Additionally, MnO_2 nanorods were fabricated using a hydrothermal method for supercapacitor applications.[24] Hydrothermally grown $Ga(OH)_2$ nanorods with the width of 200-500 nm present a low cost and large scale production strategy to prepare nanorods for practical applications.[25]

While significant work has been devoted to the fabrication of metal hydroxide/oxide nanorods and nanowires, large-scale production of high-quality crystalline ultrathin nanowires

with precise morphological control for higher aspect ratio is rare. Nanowires should have aspect ratios greater than 20, which is defined as the length of the major axis divided by the width of the minor axis.[26] Nanowires with diameters below 10 nm are considered as “ultrathin”.[1] Ultrathin nanowires offer new functional surface structures by tuning the surface chemistry that allows fabrication of hybrid materials using chemisorption, Langmuir-Blodgett technique and layer-by-layer assembly methods.[27] Furthermore, ultrathin nanowires exhibit intrinsically high surface to volume ratios, which vary inversely with nanowire diameter. Increased colloidal stability is another property that varies inversely with nanowire diameter.[1] Therefore, improving overall properties of ultrathin nanowire properties, such as quantum conductance,[28] negative magnetoresistance,[29] low thermal conductivity,[30] and ferromagnetism[31] are of great interest for variety of applications.

1.2.1 Copper hydroxide and copper oxide

Among all transition metal elements, copper (Cu) has received considerable attention in recent years as an alternative element for expensive silver and gold, due to its high electrical conductivity and higher abundance. Copper oxide in its hydroxide form ($Cu(OH)_2$), is belongs to orthorhombic crystal lattice and an indirect band gap of 1.97 eV.[32,33] Its metal monoxide, cupric oxide (CuO), is a p-type semiconductor with narrow and indirect energy bandgap of ~1.2 eV and monoclinic crystal structure. Each copper atom in CuO is coordinated to four coplanar oxygen atoms at the corner in a parallelogram manner.[19] It has intriguing properties such as environmental benign, chemical stability, high catalytic activity, easy synthesis route, electrochemical activity, antimicrobial activity, and higher abundance than rare earth metals. They can form diverse nanoscale morphologies, such as nanowires[34,35], nanoflowers[36–38], nanorods[39–41], nanoplatelets[42], nanotubes[40], nanobelts[34], nanoparticles[39,41], nanoleaves[38,43], and many more. Therefore, it has been extensively investigated for diverse applications including for gas sensors, solar cells, heterogeneous catalysts, lithium ion batteries, supercapacitors.[36–38,41,43–45]

$Cu(OH)_2$, and CuO nanowires (NWs) typically synthesize via vapor phase evaporation[46,47] and direct thermal oxidation procedures.[35,48–52] Moreover, these methods require complicated experimental procedures, high-cost, sophisticated equipment, and rigorous experimental conditions, such as high temperature, pressure, inert atmosphere, and long reaction time. Therefore, a wet chemical synthetic approach is the most promising route to synthesize metal oxides in terms of cost, throughput, greener chemistry, and the potential for large-scale production in industry.[53,54] There is a considerable body of reported work on $Cu(OH)_2$ and CuO nanostructures with different morphologies using wet chemical synthesis, such as hydrothermal synthesis, and solvothermal methods.[38,53–57] However, only very few reports are about ultrathin $Cu(OH)_2$/CuO NWs. These ultrathin NWs were synthesized using either weak and strong bases[34], i.e. aqueous ammonia and NaOH/KOH solutions, or by the interaction between a copper complex and NaOH at the aqueous-organic interface.[56]

1.3 Crystal growth mechanisms

In this section, different crystal growth mechanisms are being discussed for the growth of various nanostructures. The Lamer mechanism is a classical mechanism that generally describes a nanoparticle growth in a wet synthesis.[58] It is an instantaneous nucleation process followed by diffusion controlled growth.[59] Apart from the Lamer mechanism, the two other main crystal growth mechanisms, i.e., Ostwald ripening and oriented attachment, are discussed below.

1.3.1 Ostwald ripening (OR) mechanism

OR is a classical crystallization mechanism, by which smaller crystallites grow into the larger crystallites according to the Gibbs–Thomson relation (equation 1).[2–4] According to this mechanism, particles of various sizes dispersed in the solution achieve the competitive growth of particles via diffusion. This controlled crystal growth process achieves the minimum energy state by decreasing the total interfacial area within the agglomerated nanoparticle.[60]

$$C_r = C_e exp\left[\frac{2\gamma\Omega}{RTr}\right] \quad \text{.....(1)}$$

where, C_r is the equilibrium concentration at the surface of the particle, C_e is the equilibrium concentration at a plane interface, γ is the surface free energy, R is the universal gas constant, Ω is the molar volume of the particle, T is the temperature, and r is the radius of the particle.

According to the OR mechanism, the particle diameter increases with the addition of ions from smaller particles to the larger particle surface. This results a concentration gradient at surface of particles in the solution, as shown in Figure 1.

Figure 1: Schematic Representation of OR-Based Crystal Growth

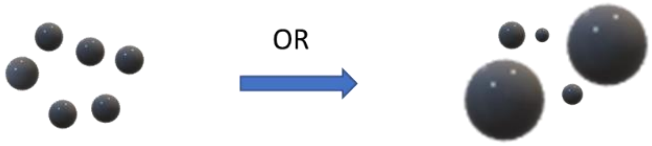

Usually, the OR-based crystal growth processes yield spherical particles, with diameters in the micro-meter range. It can also yield particles with similar crystal symmetry and crystal facet surface energies.[4] However, for crystals in the nanometer regime, the crystal growth kinetics can neither be explained by OR nor fitted by its kinetic model. Therefore, the nanoscopic growth mechanism is controlled by another mechanism.

1.3.2 Oriented attachment (OA) mechanism

The oriented attachment (OA) is often known to explain the self-assembly of nanocrystals to form anisotropic structures at nanoscale by sharing a common crystallographic orientation.[6,7] In 1998, Penn et al. observed the anisotropic chain of TiO_2 anatase crystals attachment across the {112} facets using a high-resolution transmission electron microscope (HR-TEM). They proposed a nonclassical phenomenon of crystal growth called “oriented attachment” or “oriented aggregation” to explain the nanoscopic growth dynamics.[2,4,6,61] OA

involves the spontaneous assembly of adjacent primary nanocrystals into secondary crystals, through Brownian motion, which share a common crystallographic orientation (Figure 2 (a)). OA-based crystal growth is driven by the thermodynamic reduction of surface energy.[6,12] The primary nanocrystal colloids in a solution rotate for a crystal lattice match and then start the coalescence of nanocrystals, merging interfaces and reducing the system's surface energy.[62,63] Highly ordered monocrystalline materials can be formed through OA, which is a versatile approach for the preparation of anisotropic nanostructures.

Figure 2: A Schematic Representation of OA-Based Crystal Growth and A Grain-Rotation-Induced Grain Coalescence Mechanism.

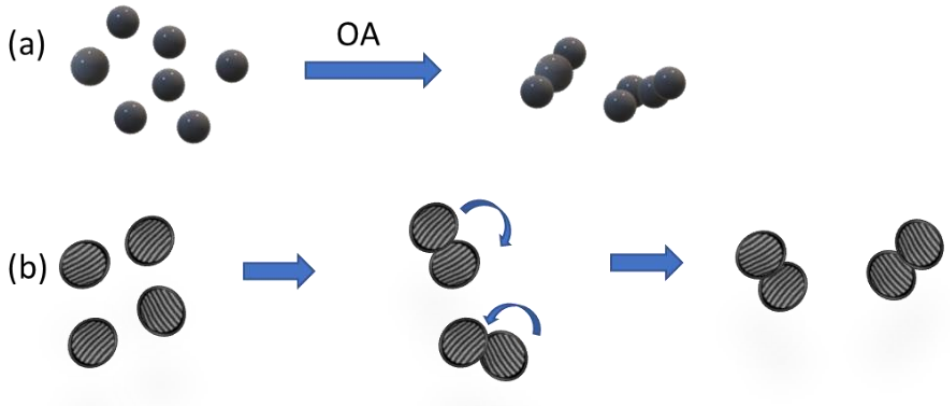

Moldovan et al. proposed a Grain-Rotation-Induced Grain Coalescence (GRIGC) mechanism to describe the grain growth process of OA-based nanomaterials[64]. It is illustrated in Figure 2 (b). According to this model, the driving force for the rotation of crystals is to achieve a perfect coherent grain–grain interface, which leads to the coalescence of neighboring crystals to eliminate the common grain boundaries and form a single larger crystal. Therefore, this mechanism is correlated to the reduction of the surface energy by minimizing the area of high energy surfaces. Leite et al. experimentally observed this mechanism in the room temperature growth of SnO_2 nanocrystals.[65] Recently, Li and coworkers directly observed the OA mechanism of iron oxyhydroxide nanoparticles using a fluid-cell high-resolution transmission electron microscope.[66]

The ultrathin nanowires produced by the OA process provide unique features, such as constant nanowire diameter during growth by direct attachment of nanocrystals to the tip of the growing nanowire, similar to polymerization reactions.[67] Therefore, the nanowire diameter can be predetermined by the diameter of the nanocrystals, which are monodispersed. However, disadvantages of OA-based nanowire synthesis methods include low yields and residues of ligands and solvents attached to the nanowire.[1]

1.3.3 In situ investigation of crystal growth

The recent emergent advances of liquid-phase transmission electron microscopy provide great opportunities for the direct visualization of crystallization pathways of different nanomaterials.[66,68–71] The selective area electron diffraction (SAED) and energy-dispersive X-ray spectroscopy (EDS) coupled with liquid-phase TEM help to track the crystallinity and compositional transformation during crystal formation.[72] In situ TEM with high spatial and temporal resolution serves as an appropriate tool for understanding the underlying growth mechanism and reaction kinetics of materials by monitoring reactions in real time and on an atomic scale. Furthermore, it provides enhanced understanding of crystal defect formation during the nanocrystal's attachment along a common crystallographic orientation by the OA mechanism.[73] Consequently, our understanding of nanocrystal nucleation, growth processes, and their dynamics have been accelerated by the application of liquid-phase TEM. Very recently, Wang et al directly observed the initiation and neck growth during oriented attachment of PbSe nanocrystals using in situ liquid cell TEM.[74] The oriented attachment growth of Pb_3O_4 nanocrystals were observed along the [002] direction using liquid cell TEM and their monomer growth rate and coalescence rate were determined.[75] However, this technique needs to be carefully interpreted. Thus far, its application is limited to a few synthetic systems due to the electron beam effect, substrate effect, and the complexity of general synthesis procedures.[76,77]

1.4 Current State of Art

Due to the remarkable physical properties of 1 D transition metal hydroxide/oxide nanostructures, the fabrication of anisotropic metal hydroxide/oxide nanowires has attracted increasing attention in many applications. However, few reports have demonstrated cost-effective and efficient synthesis routes to fabricate ultrathin copper hydroxide/oxide nanowires. Patel and Bhattacharya reported the synthesis of OA- based CuO nanorods using a plant extract as a surfactant via a sonoemulsion method.[78] Moreover, Sundar et al. demonstrated a bio-surfactant assisted synthesis method to produce CuO nanowires, suggesting the OA crystal growth mechanism.[79] However, the study of crystal growth mechanisms and their kinetics to fabricate anisotropic nanowires are rarely explored.

The controlled synthesis to change the nanowire diameter and aspect ratio is challenging, due to the difficulty of controlling the crystal attachment kinetics and the steric barrier.[13] Bio molecules, surfactants, or organic ligands can be used to direct the oriented attachment process by selectively binding to specific nanocrystal planes to control the crystal growth rate. Examples of different OA based semiconductor nanowires through crystal facet-selective ligand capping include CdTe and CdSe.[80,81] One previous work reported that the selected surfactant can control the length elongation of OA based colloidal CdS and Ag_2S nanorods along a specific growth direction.[82] Another work presented the controlled crystal growth of TiO_2 nanowires in the presence of biomolecules in organic solvents with a nonaqueous sol-gel synthesis.[83] Recently, with the assistance of sodium dodecyl sulfonate (SDSN) as the capping ligand, Wang and coworkers demonstrated the formation of ultralong ZnO nanowires, which has 20-80 μm length by the oriented attachment mechanism.[84]

1.5 General Goals of Research

Overall goal of the dissertation:

The study of nanocrystal growth mechanism and kinetics of ultrathin 1D-metal hydroxide/oxide nanowires, and the in-situ self-assembly with phospholipids during the formation of nanowires by sol-gel synthesis.

Overall dissertation hypothesis:

The oriented attachment-based crystal growth mechanism will drive formation of 1D metal hydroxide nanowires and, in the presence of phospholipids at the oil-water interface, will enable self-assembly into 1D supramolecular bionanomaterials.

Rationale:

The controlled synthesis of ultrathin transition metal hydroxides/oxide nanowires is still in its preliminary stage. Guiding principles for this process, in terms of controlling size and shape, remain elusive. Besides, the crystal growth mechanism(s) and the corresponding fabrication kinetics are poorly understood and rarely explored. The uniformity of ultrathin nanowires, their crystallinity, and their reproducibility using aqueous chemical routes have yet to be reported. Therefore, it is important to explore and report on possible scalable, environmentally benign wet chemical synthesis methods at lower temperatures like room temperature. New kinetic models for the OA-directed crystal growth of one-dimensional nanostructures needs to be developed using experimental data. Finally, this work needs to expand the understanding of crystal growth processes in the presence of biomolecules to make controlled novel supramolecular structures.

Addressing the overall hypothesis, this research proposes two specific aims:

Aim 1: To investigate the oriented attachment crystal growth mechanism of $Cu(OH)_2$ nanocrystals for the formation of $Cu(OH)_2$ nanowires.

Goal 1: To demonstrate a versatile oriented attachment crystal growth process to direct the synthesis of size and shape-controlled binary transition metal hydroxide/oxide nanowires in a surfactant free aqueous medium at room temperature.

Hypothesis: Copper hydroxide nanowire formation in water at room temperature will follow the classical oriented attachment crystal growth mechanism.

Rationale: The oriented attachment crystal growth process provides directional crystal growth along a selective crystal facet of nanocrystals, yielding size and shape-controlled metal hydroxide/oxide nanowires in water at room temperature.

Novelty: This study would be the very first study demonstrating the oriented attachment crystal growth process in water at room temperature to make copper hydroxide nanowires. Also, the versatile synthesis method developed here would be a new discovery and would widely be applicable to make other binary transition metal hydroxide and metal oxide nanowires.

Expected Outcomes: Successful completion of Aim 1 will result in: (1) Ultrathin $Cu(OH)_2$ nanowires formation following the OA crystal growth mechanism, and (2) new kinetic models for the crystal growth of OA- based $Cu(OH)_2$ nanowires, assuming consecutive second order and zeroth order stages of crystal growth.

Aim 2: To investigate $Cu(OH)_2$ nanocrystal growth and formation of $Cu(OH)_2$ nanowires in the presence of phospholipids.

Goal 2: To demonstrate a novel self-assembly process to fabricate colloidal metal hydroxide nanowire supramolecular structures decorated with phospholipids.

Hypothesis: $Cu(OH)_2$ nanocrystals will form 1D nanostructures at the oil-water interface in the presence of phospholipids as a surfactant and adsorb different concentrations of phospholipids on specific crystal faces, which will lead to different morphologies of 1D nanostructures, such as nanorods and nanowires.

Rationale: Surface energy induced nanostructures of phospholipid decorated transition metal hydroxides provide bionanomaterials platforms, with directional growth at the oil/water interface, for the fabrication of ultrathin supramolecular devices.

Novelty: Self-assembly of supramolecular structures from phospholipid decorated transition metal hydroxide nanowires is a novel study and will provide a novel self-assembly process to make supramolecular structures of hybrid bionanomaterials.

Expected Outcomes: Successful completion of Aim 2 will result in developing a novel surfactant-directed crystal growth process based on OA crystal growth with the presence of different concentrations of phospholipids.

The chemical structure of lipid, DPPC, which is used for self-assembly with copper hydroxide is stated in the following Figure 3.

Figure 3: The Chemical Structure of DPPC(1,2-Dipalmitoyl-Sn-Glycero-3-Phosphocholine); M.W.-734 g/mol.

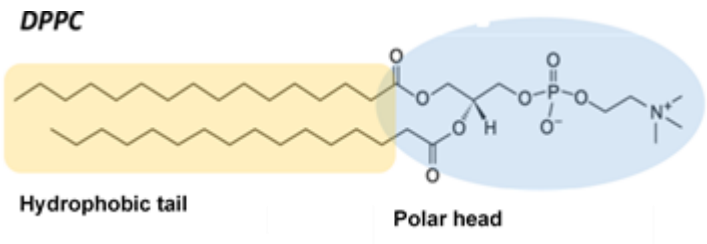

1.6 Dissertation Layout

This dissertation consists with the following six chapters and a brief introduction to each chapter is outlined below. The Chapter 1 starts with an overview of controlled synthesis of 1D nanostructures, transition metal hydroxide/oxide nanowires and two main crystal growth mechanisms in solution-based procedures. This chapter further discusses the importance of preparing ultrathin copper hydroxide nanowires, i.e., to develop a foundational understanding that enables the formation of guiding principles for designing fabrication processes for ultrathin nanowires. Finally, the current state of 1 D transition metal oxide nanostructures and the controlled crystal facets with selective surfactants to tune the dimensions and morphology are discussed. Then, general goals of this dissertation are presented. The Chapter 2 reviews the basic wet chemical synthesis methods, the theoretical background of sol-gel reaction, the

surface energy of crystals, and working principles of transmission electron microscopy for the evaluation of crystal growth processes. Then, two main crystal growth kinetic models and rates and their prior arts are described, while addressing the gap of appropriate kinetic models for anisotropic nanowire growth, based on length. In Chapter 3, synthesis of $Cu(OH)_2$ and CuO colloidal nanowires using a novel, facile and greener synthesis method is discussed. The full description of the materials, the experimental setup used, the characterization techniques used, and an analysis and discussion of results are provided. The Chapter 4 presents the investigation of crystal growth and the kinetics for the formation of ultrathin $Cu(OH)_2$ nanowires using high resolution transmission electron microscopy (HR-TEM) combined with UV-visible spectroscopy. The novel kinetic model developed, along with the full analysis, are demonstrated. In Chapter 5, the crystal growth of phospholipid assisted ultrathin copper hydroxide nanowires is discussed. The fabrication of OA based crystal facet selective controlled growth of supramolecular ultrathin nanowires in the presence of phospholipids is presented. Finally, Chapter 6 provides a summary of the dissertation, along with some suggestions and recommendations for possible future studies.

CHAPTER II: BACKGROUND

2.1 Metal oxide nanowire growth strategies

Typically, metal oxide NWs are produced via top down and bottom-up techniques. Bottom-up techniques are most commonly used due to the high purity of the product, low cost fabrication, and the dimension controllability.[85] Among bottom-up techniques, the controlled fabrication of metal oxide nanowires can be done either by vapor or solution phase growth strategies. Shen and coworkers summarized different 1-D metal oxide nanostructures including nanowires, nanobelts, nanorods, and nanotubes synthesized using vapor or solution phase growth strategies.[86] The controlled pressure of the inert atmosphere and high-temperature vapor-phase approaches are expensive and need sophisticated instruments.[87–90] Examples of vapor phase growth processes are vapor–liquid–solid (VLS), solution–liquid–solid (SLS), vapor–solid–solid (VSS) or vapor–solid (VS) process, physical vapor deposition (PVD), and chemical vapor deposition (CVD). Therefore, solution based wet chemical strategies became popular, as they are inexpensive, energy efficient, excellent control over size and morphologies, with ease of larger scale production.[20] The most common wet chemical strategies are hydrothermal method, thermal decomposition, electrochemical method, solvothermal method, and sol-gel method.[20]

2.1.1 Wet chemical synthesis routes

The wet chemical routes can be performed through precipitation or oxidation of the precursor from a catalyst or surfactants and by heating in an oxygen rich environment to make metal oxide/hydroxide NWs.[91] In a hydrothermal route, heating the precursor solution/ substrate and then annealing in an oxygen environment is required to form metal oxide nanowires.[20] Solvothermal methods are performed by heating a metal precursor solution to a high temperature in the presence of a solvent.[92] Microwave assisted synthesis represents another powerful method that requires heating to a high temperature in a microwave.[93] Therefore, most

wet chemical growth strategies require expensive chemicals, heating procedures, longer reaction times, templates, or impurity removal after the procedure.[91] In contrast, the sol-gel method is a greener and lower temperature method that makes homogeneous, highly stoichiometric, and high quality metal oxide/hydroxide nanowires in a larger scale production.[94,95]

2.1.2 Sol-gel technique

The sol–gel process is a wet-chemical technique widely employed for the fabrication of size and shape-controlled metal hydroxide/oxide nanostructures. Starting from a metal salt as the precursor and catalyzed by base or acid, it forms an integrated network (or gel) of either discrete particles or network polymers. Sol-gel chemistry was first discovered in the 19th century introduced by the hydrolysis and then condensation of silicon alkoxide to form a gel when exposed to an air.[96,97] After the controlled synthesis of monodisperse silica spheres by Stöber[98], the sol-gel method became popular to make different solid networks such as inorganic oxides, organic polymers, organic-inorganic hybrids, and composites. It offers different advantages such as high yield, better reproducibility, low operation temperature and low cost method of highly stoichiometric and homogeneous products.[99–101]

Figure 4: Steps of A Typical Sol-Gel Process

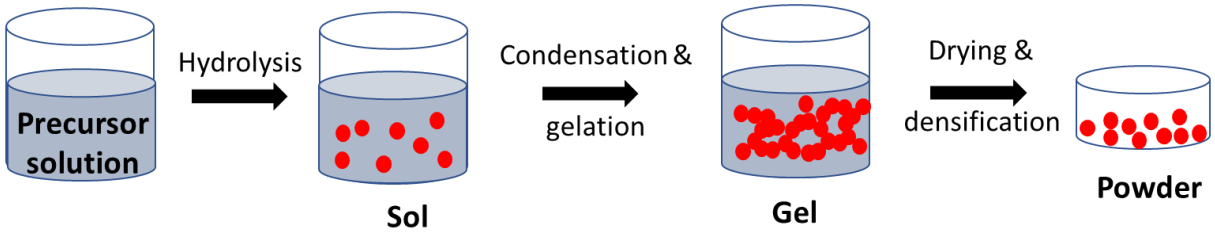

In general, a sol–gel process enables the transition of a liquid solution “sol” into a solid “gel” phase. It is a low temperature multistep processing technique, involving both physical and chemical reactions, such as hydrolysis, condensation, drying, and densification, as shown in Figure 4.[102] When preparing metal oxides, first, the sol is formed from the hydrolysis and condensation of metal alkoxides. The sol is a stable dispersion of colloidal particles in a liquid

solution, and the particles can be amorphous or crystalline. Then the gel is formed through polycondensation and aging to form a gel network using metal–oxo–metal or metal–hydroxy–metal coordinate bonds. The conventional sol-gel process (equation H1 to H3) is hydrolytic and oxo ions are originated from water in the reaction medium. Nonhydrolytic sol–gel process pathways (equation N1 to N2) were developed later using organic solvents as reagents in the medium and the oxygen atoms originated from the organic O-donor.[99,103–105] However, both sol-gel processes have their own limitations with different metal precursors.[99,105]

Hydrolytic sol-gel formation

$$\equiv M{-}OR + H_2O \rightarrow \equiv M{-}OH + ROH \quad \text{Hydrolysis} \ldots\ldots\ldots\ldots\ldots\ldots H1$$

$$\left.\begin{array}{l} \equiv M{-}OH + \equiv M{-}OR \rightarrow \equiv M{-}O{-}M{\equiv} + ROH \\ \equiv M{-}OH + \equiv M{-}OH \rightarrow \equiv M{-}O{-}M{\equiv} + H_2O \end{array}\right\} \text{Condensation}$$

$\ldots\ldots\ldots\ldots\ldots H2$

$\ldots\ldots\ldots\ldots\ldots H3$

Nonhydrolytic sol-gel formation

$$\equiv M{-}OR + M{-}X \rightarrow \equiv M{-}O{-}M{\equiv} + R{-}X \quad (X = OR, Cl, OOCR) \ldots\ldots\ldots\ldots\ldots\ldots N1$$

$$\equiv M{-}OR + RO{-}M \rightarrow \equiv M{-}O{-}M{\equiv} + R{-}O{-}R \quad \ldots\ldots\ldots\ldots\ldots\ldots N2$$

Here, M denotes the metal.

Drying and densification involve condensing the gel by collapsing the porous gel network. Although inorganic crystal shapes often are related to the intrinsic unit cell structure, the same material can exhibit diverse crystalline morphologies. The morphology is influenced by either different surface energies of the crystal faces or the external growth environment, which combines with different factors such as precursor to base concentration, solvent polarity, temperature, and crystal growth mechanism. Different types of metal oxides have been synthesized using the sol-gel route, exhibiting different morphologies such as nanoparticles, nanorods, nanoplatelets, and wires.[106–110]

2.1.2.1 Chemical rates of a sol-gel reaction

Sol-gel reactions consist of three main chemical processes, which include acid or base catalyzed hydrolysis, condensation and polycondensation, followed by gelation. The chemical kinetics of each process can be studied to understand the crystal growth process, size and shape formations of the metal oxide/hydroxide nanostructures. Chemical reaction rates can be expressed as the changes in concentrations of the reactants or products per unit time. For example, consider the reaction of reactant A transforming into product B, i.e., $\mathrm{A} \rightarrow \mathrm{B}$. Then, for this single step reaction, the rate can be expressed as $-{}^{\mathrm{d[A]}}/_{\mathrm{dt}}$, in terms of disappearance of reactants A or $+{}^{\mathrm{d[B]}}/_{\mathrm{dt}}$, in terms of appearance of product B.

The chemical kinetic rate law can be represented in the form of

Rate = $k[A]^x$ ……..……..(1)

where x is the order of the reaction with respect to A and k is the rate constant.[111]

As a result, the rate law depends on the concentration of reactant(s). Straightforward reactions under homogeneous conditions may exhibit simple first-order, second-order, or zeroth order kinetic behavior. The exponent x, order of reaction is experimentally determined and does not reflect the stoichiometry of the chemical equation in every reaction. The slowest step in the mechanism is the rate limiting step, which controls the rate of the entire reaction.

For a reaction; A→ B

(1) First order reaction

The rate law; $\mathrm{Rate} = \mathrm{k[A]} = -{}^{\mathrm{d[A]}}/_{\mathrm{dt}}$----------(2)

By rearranging and integrating equation (2); $-\int_{[\mathrm{A_0}]}^{[\mathrm{A_t}]} \frac{\mathrm{d[A]}}{\mathrm{[A]}} = \mathrm{k}\int_0^{\mathrm{t}} \mathrm{dt} - - - (3)$

$$\ln \frac{\mathrm{A_0}}{\mathrm{A_t}} = \mathrm{kt} - - - - (4)$$

Therefore, the integrated law is $\ln[\mathrm{A}]_{\mathrm{t}} = -\mathrm{kt} + \ln[\mathrm{A}]_0$---------(5)

By plotting the graph of $\ln[A]_t$ vs t using this linear form of equation, the rate of the reaction can be found out using its slope.

(2) Second order reaction

For a reaction: A + A→ B, where the rate limiting step is the collision of two molecules of reactant A, then

The rate law; $\text{Rate} = k[A]^2 = -{}^{d[A]}/_{dt}$---------(6)

By rearranging and integrating equation (6); $-\int_{[A_0]}^{[A_t]} \frac{d[A]}{[A]^2} = k\int_0^t dt$--------(7)

$${}^{1}/_{[A]_t} - {}^{1}/_{[A]_0} = kt$$------(8)

Therefore, the integrated law is ${}^{1}/_{[A]_t} = kt + {}^{1}/_{[A]_0}$--------(9)

By plotting the graph of ${}^{1}/_{[A]_t}$ vs t using this linear form of equation, the rate of the reaction can be found out using its slope.

(3) Zeroth order reaction

When the overall rates appear to be independent of the concentration of reactant A, then the reaction may be zero or pseudo-zero order. This can occur when the concentration of A is high and the initial reaction consumes <1% of A or when the collision of two As to form an [A-A] complex is fast and the transition of that complex to the product, B, is the rate limiting step.

The rate law; $\text{Rate} = k = -{}^{d[A]}/_{dt}$-------(10)

By rearranging and integrating equation (10); $-\int_{[A_0]}^{[A_t]} d[A] = k\int_0^t dt - (11)$

$$[A]_0 - [A]_t = kt - - - (12)$$

Therefore, the integrated law is $[A]_t = -kt + [A]_0 - - - (13)$

By plotting the graph of $[A]_t$vs t using this linear form of equation, the rate of the reaction can be found out using its slope.

(4) N[th] order reaction

The rate law; $\text{Rate} = k[A]^n = -{}^{d[A]}/_{dt}$-------(14)

By rearranging and integrating equation (14); $-\int_{[A_0]}^{[A_t]} \frac{d[A]}{[A]^n} = k\int_0^t dt$------(15)

$$\frac{1}{[A]^{(n-1)}} - \frac{1}{[A_0]^{(n-1)}} = (n-1)kt \quad (16)$$

Therefore, the integrated law is $(n-1)kt = \frac{1}{[A]^{(n-1)}} - \frac{1}{[A_0]^{(n-1)}}$----(17)

By plotting the graph of $\frac{1}{[A]^{(n-1)}}$ vs t using this linear form of equation, the rate of the reaction can be obtained from its slope.

2.2 Crystal growth kinetic models and rates

2.2.1 OR kinetic model

Lifshitz and Slyozov discovered the OR mechanism and Wagner proposed the corresponding LSW kinetic model, which can be expressed as equation 18.[5,112] It is attributed to first order chemical reactions with the linear growth rate described by an exponential function.[60]

$$D^n - D_0^n = k(t - t_0) \ldots\ldots\ldots\ldots (18)$$

where *D* and D_0 are the mean particle sizes at time t and t_0, k is a temperature-dependent rate constant, n is an exponent relevant to the coarsening mechanism through the diffusion.

2.2.2 OA kinetic model

The following three kinetic models for OA-based crystal growth were developed to explain the 1D crystal growth kinetics of nanocrystals and to fit the experimental growth curves.[5,113]

(1) A_1+A_1 model

When two primary nanoparticles in the colloidal solution collide and coalescence each other, they make a secondary nano particle according to the following reaction. Therefore, it can be described by second order chemical reactions.

$$A_1 + A_1 \longrightarrow A_2$$

where, A_1 is the primary particle, A_2 is the secondary particle and k_1 is the rate constant.

The direct attachment of two primary particles is only considered in this model and schematic representation has shown in Figure 5.

Figure 5: The Schematic Representation of A_1+A_1 Model

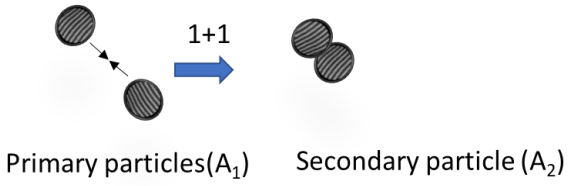

According to the principle of mass balance of primary particles and secondary particle, the number of mature secondary particles can be estimated by the following equation 19.[4,5]

$$\frac{1}{6}\pi\rho Do^3 No = \frac{1}{6}\pi\rho Do^3 N_{(t)} + \frac{1}{6}\pi\rho D_2{}^3 N_{2(t)} \quad \text{.....(19)}$$

where, primary the particle diameter and number are D_0 and N_0, respectively, at t = 0. The secondary particle diameter at time t and the number of secondary particles are D_2 and $N_{2(t)}$, respectively. ρ is density of the particle.

Here, $V_2 = 2V_0$

$$D_2 = \sqrt[3]{2}\, D_0 \quad \text{.....(20)}$$

$$N_{2(t)} = (N_0 - N_{(t)})/t \quad \text{.....(21)}$$

The second order reaction for the disappearance of primary particles per unit time can be written as

$$-\frac{dN(t)}{dt} = kN(t)^2 \quad \text{.....(22)}$$

By integrating $\frac{1}{N(t)/(N0)} = k_1 t + 1$ ....(22)

where, $k_1=kN_0$

The average particle diameter is estimated according to the Scherrer method in XRD data analysis that used to calculate the average crystallite size of a sample and is expressed in the following equation.

$$D = \frac{N(t)D_0^4 + N_2(t)D_2^4}{N(t)D_0^3 + N_2(t)D_2^3} \quad \text{.....(23)}$$

The A_1+A_1 growth model can be stated as equation 7**,**

$$d = \frac{d_0\left(\sqrt[3]{2}k_1 t+1\right)}{(k_1 t+1)} \quad \text{.....(24)}$$

where, d_0 is the mean diameter at time t=0 for the primary nano particle and d is the mean diameter at time t for the secondary nanoparticle.

Therefore, this model assumes only primary particles and secondary particles in a system.

(2) A_1+A_i model

The collision between a primary particle and a multilevel particle also occurs in a system as follows.

$A_1 + A_1 \longrightarrow A_2$

$A_1 + A_{i-1} \longrightarrow A_i$

where, A_1 is the primary nanoparticle, A_i is the particle containing *i* primary particles.

Therefore, this model only considers about the direct attachment between primary particle and multilevel particles. When all the primary particles are consumed in the solution, the reaction stops immediately.

This scenario hypothesizes that the reaction between A_i and A_j $(i \geq 2, j \geq 2)$ is neglected due to its lower probability of interaction and the irreversibility of the reaction.

Figure 6 illustrates the growth model of direct attachment of a primary particle and a multilevel particle.

Figure 6: The Schematic Representation of The A_1+A_i Model, i.e., The Direct Attachment of A Primary Particle And A Multilevel Particle, Such As (A_1+A_2), (A_1+A_3), (A_1+A_4), and etc.

The time evolution of the concentration of A_1 is

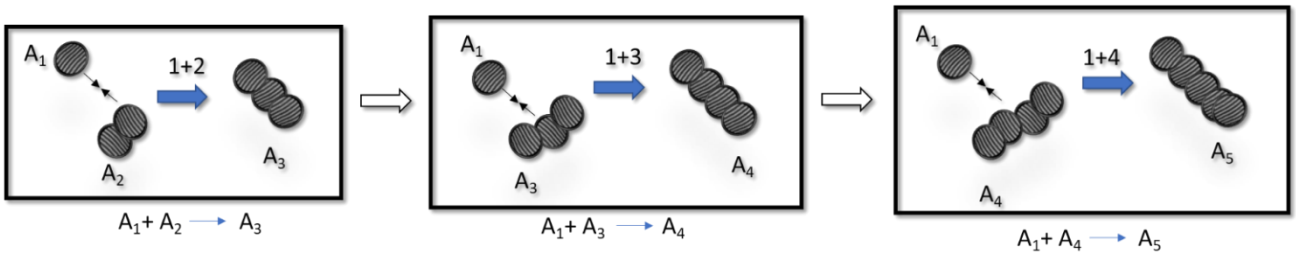

$$\frac{dN_1}{dt} = -2k_1N_1^2 - N_1\sum_{i=2}^{\infty} k_iN_i \quad \text{.....(25)}$$

where, N_1 is the concentration of primary particles and N_i is the concentration of growth particle A_i for a period of time, t.

The time evolution of the concentration of A_i is

$$\frac{dN_i}{dt} = k_{i-1}N_1N_{i-1} - k_iN_1N_i \quad (i\geq 2)\text{.....(26)}$$

where, N_{i-1} is the concentration of multilevel particles, A_{i-1} for a period of time, t.

The aggregation of nanocrystals can be described using the time evolution size distribution of the nanocrystals, developed by Smoluchowski.[5] According to the Smoluchowski equation, the rate constant for this reaction is

$$k_i = 4\Pi(R_1 + R_i)D_1 \quad \text{.....(27)}$$

where, R_i is the radius of the nanoparticle containing i primary particles, and D_1 is the particle diffusion coefficient.

According to the equivalent volume relation, $R_i = i^{1/3}R_1$.

For equations 25-27, a numerical simulation is used to estimate the particle distribution at different stirring and growth times. Euler's polygon method can be applied, assuming a first order Taylor series approximation as follows

$$N_{(i,t+\Delta t)} = N_{(i,t)} + \frac{\partial N_{(i,t)}}{\partial t}\Delta t \quad \text{.....(28)}$$

To ensure the accuracy of the result, Δt should be small. Usually, $\Delta t = {}^{1}/_{N.D_1}$ is used for the calculations and N is the number of particles.

The average size, d_{eq}, at a certain time can be obtained by equation (26), below,

$$d_{eq} = \sum N_k d_k^4 / \sum N_k d_k^3 \quad \text{.....(29)}$$

where, d_k is the size of the secondary particle containing k primary particles and N_k is the number of secondary particles.

(3) (A_i+A_j) multistep kinetic model

When the base concentration is high, the surface adsorption becomes rapid in the system, and hence coarsening is stable. Therefore, the probability of collision between multilevel particles increases. This model only considers the growth mechanism of two multilevel particles in the solution. As the coalescence of multilevel particles increases particle

sizes and decreases their mobility with time, this reaction slows down rapidly and finally stops. In that case, the multistep kinetic model can be given as the following.

$A_i + A_j \longrightarrow A_k$ (i, j, k=1,2,…..) and k=i+j

where, A_k is the nanoparticle which contains primary particles of number k

The collision between multilevel particles takes place in the multistep reaction model as illustrated in Figure 7.

Figure 7: The Schematic Representation of A_i+A_j Model, i.e., The Direct Attachment of Two Multilevel Particles, Such As (A_2+A_1), (A_2+A_2), (A_3+A_2), And Further Reaction Steps.

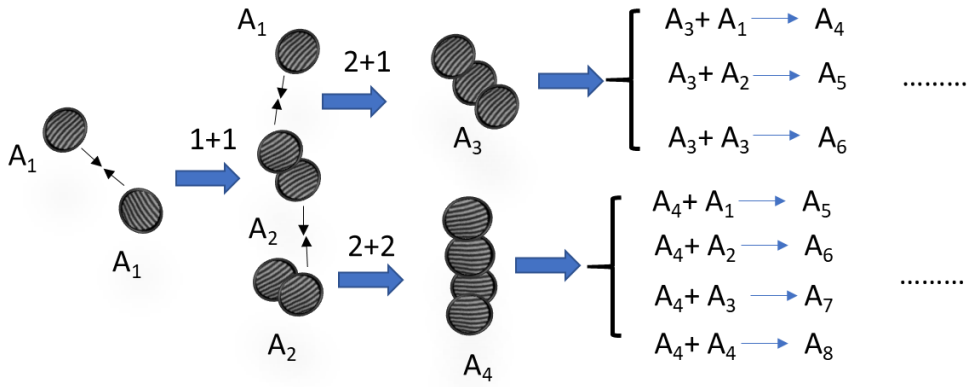

The time evolution of the concentration of A_k can be defined as

$$\frac{dN_k}{dt} = \frac{1}{2}\sum_{i+j=k} K_{ij}\, N_i N_j - N_k \sum_j K_{kj} N_j \quad \text{.....(30)}$$

where, N_k is the concentration A_k and K_{ij} is the rate constants for the reaction between the particles.

According to the Smoluchowski equation, the rate constant for this reaction is

$$k_{ij} = 4\Pi(R_i + R_j)(D_i + D_j) \quad \text{.....(31)}$$

where, R_i and D_i are the radius and diffusion coefficient of the particle containing i primary particles, respectively.

$$k_{ij} = 4\Pi R_1 D_1 \left(i^{1/3} + j^{1/3}\right)(i^{\propto} + j^{\propto}) \quad \text{.....(32)}$$

where, R_1 and D_1 are the radius and diffusion coefficient of primary particle and α is a constant.

For equations 30-32, a numerical simulation is used to estimate the particle distribution at different stirring and growth times. As above, Euler's polygon method is applied, assuming a first order Taylor's formula, to yield

$$N_{(i,t+\Delta t)} = N_{(i,t)} + \frac{\partial N_{(i,t)}}{\partial t}\Delta t \quad \text{.....(33)}$$

To ensure the accuracy of the result, Δt should be small. Usually, $\Delta t = {}^{1}/_{N.D_{max}}$ is used for the calculations, N is the number of particles, and D_{max} is the maximum diffusion coefficient for any of the particles in the system.

The average particle size, d_{eq} , at a certain time can be obtained by following equation

$$d_{eq} = \sum N_k d_k^4 / \sum N_k d_k^3 \quad \text{.....(34)}$$

where, d_k is the size of the secondary particle containing k primary particles and N_k is the number of secondary particles.

2.2.3 The prior art of crystal growth kinetic models

Crystal growth kinetics depends on the nature of the material, crystal facet interfaces, the working temperature, the type of surrounding solution, and the concentration of the solution.[114] Most often, OR and OA mechanisms occur simultaneously or coexist in the same model. However, by introducing surfactants to strongly adsorb onto crystal surfaces, it has been reported that a solo OA mechanism causes to grow the nanocrystals by hindering the OR mechanism at initial stages.[114,115] Moreover, the OA mechanism dominates in unsaturated solutions by suggesting that the OR mechanism can be thermodynamically disfavored without having a high enough concentration to dissolve nanoparticles.[116] The prior art of these existing

kinetic models, used to understand the crystal growth mechanism by fitting the experimental observation of different nanocrystals, is summarized in the Table 1.

Table 1: Summary of nanocrystal growth models studied from years 2003 to 2020.

Growth system	Capping ligands	Model	Kinetic equation	Published year
Nano ZnS	Mercaptoethanol	"1+1" sequential OA + OR	1st stage-OA; $D = \frac{D_0(\sqrt[3]{2}k_1 t+1)}{k_1 t+1}$ 2nd stage-OR; $D^n - D_0^n = k(t - t_0)$	2003[113]
Nano ZnS	NaOH	"i+j" sequential OA + OR	1st stage-OA; $d_{eq} = \sum N_k d_k^4 / \sum N_k d_k^3$ 2nd stage-OR; $D^n - D_0^n = k(t - t_0)$	2006[114], 2007[118]
Thiol-capped PbS nanoparticles	Ligand free (water)	"i+j" OA and "1+1" OA+ OR	First stage-OA; $d_{eq} = \sum N_k d_k^4 / \sum N_k d_k^3$ 2nd stage-$D = \frac{D_0(\sqrt[3]{2}k_1 t+1)}{k_1 t+1} + k_2 t^{\frac{1}{n}}$	2007[115]

SnO_2 nanoparticles	Ligand free (water)	"i+j" OA	$d_{eq} = \sum N_k d_k^4 / \sum N_k d_k^3$	2006[119], 2009[116]
CdS Nanorods	Amine	"i+j" OA	$d_{eq} = \sum N_k d_k^4 / \sum N_k d_k^3$	2010[120]
TiO_2 anatase nanoparticles	Succinic acid	"1+1" OA, shrinkage, and OR	1st stage-OA; $D = \frac{D_0(\sqrt[3]{2}k_1 t+1)}{k_1 t+1}$ 2nd stage- shrinkage 3rdstage-OR; $D^n - D_0^n = k(t - t_0)$	2010[121]
(TGA)-capped CdTe nanoparticles	Ligand free (water)	"1+1" mixed OA + OR	$D = \frac{D_0(\sqrt[3]{2}k_1 t + 1)}{k_1 t + 1} + k_2 t^{\frac{1}{n}}$	2011[122]
ZnO QDs	Ethanol	"1+1" sequential OA + OR	1st stage-OA; $D = \frac{D_0(\sqrt[3]{2}k_1 t+1)}{k_1 t+1}$	2012[123]

			2nd stage-OR; $D^n - D_0^n = k(t - t_0)$	
CdS QDs	TGA	"1+1" mixed OA + OR	$D = \frac{D_0(\sqrt[3]{2}k_1 t + 1)}{k_1 t + 1} + k_2 t^{\frac{1}{n}}$	2013[124]
CdTe QDs	Mercaptopropionic acid	"1+1" mixed OA + OR	$D = \frac{D_0(\sqrt[3]{2}k_1 t + 1)}{k_1 t + 1} + k_2 t^{\frac{1}{n}}$	2014[125]
Co_2FeO_4	Polypeptide c25-mms6	"1+1" sequential OA + OR	1st stage-OA; $D = \frac{D_0(\sqrt[3]{2}k_1 t+1)}{k_1 t+1}$ 2nd stage-OR; $D^n - D_0^n = k(t - t_0)$	2014[126]
Gd_2O_3 nanorods	Ligand free (water)	"1+1" OA	$D = \frac{D_0(\sqrt[3]{2}k_1 t + 1)}{k_1 t + 1}$	2016[127]
ZnO QDs	Ligand free (water)	"1+1" mixed OA + OR	$D = \frac{D_0(\sqrt[3]{2}k_1 t + 1)}{k_1 t + 1} + k_2 t^{\frac{1}{n}}$	2019[128]

Considering the state-of-art for crystal growth kinetics in Table 1, all the existing kinetic models were developed based on particle diameter growth. Two reports qualitatively attempted to explain the kinetic rate for the elongation of one-dimensional nanorods by considering dipole attraction for their alignment.[120,127] Up to now, none of the studies reported about the oriented attachment crystal growth kinetics of nanowire that explains the 1D growth of the length into a specific direction.

2.3 Surface energy of nanocrystals

Nanocrystal surface energy(γ) is a fundamental property that is a function of each crystal facet, which determines the crystal's shape and eventually the morphology of a nanostructure.[129,130] Anisotropic nanocrystal growth is directly related to the surface energy of different crystal planes. The different crystal facets grow along different planes at different rates, which determines the final shape. This surface phenomenon is most significant at the nanoscale, due to the higher surface area to volume ratio, versus that in bulk materials.

2.3.1 Wulff construction

Miller indices represent crystal planes in the lattice with three parameters {hkl}, which are composed of the reciprocals of the intercepts of three crystal axes in the crystal plane.[131] Some examples of Miller indices in a cubic nanowire are shown in Figure 8. The surface energy of a crystal is estimated using the "broken-bond" model. Different crystal planes have a different number of broken bonds on the surface of the crystal, leading to different surface energies.[130] For example, atomic packing of (*010*), (*001*), and (*111*) crystal planes in copper hydroxide crystal structure shows different number of undercoordinated bonds, as shown in Figure 9. Therefore, the equilibrium shape of the crystal is determined by the sum of the total surface energies of different crystal planes. A Wulff plot (γ-plot) describes this property and minimizes the surface energy by reducing the number the broken bonds of an isolated single crystal.[130,132]

Theoretical approaches have been developed to explain the relationship between the morphology and the crystal structure of a material.[133] However, they are limited to surface energy calculations of simple crystal systems and a general understanding of the growth rates. The understanding of surface energy correlations between the growth rate of different crystal planes in a nanostructure is of great importance to understand the surface properties of the material.[130]

Figure 8: Miller Indices of a Cubic Nanowire

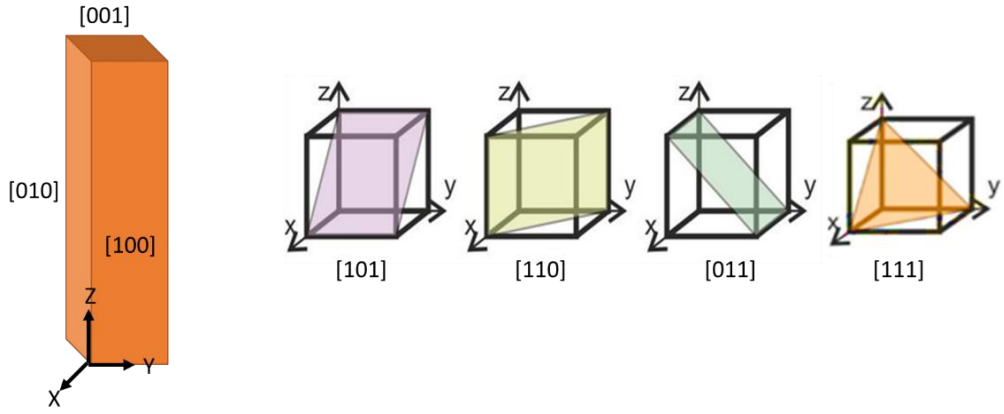

Figure 9: Crystal Planes of (010), (001), and (111) In Copper Hydroxide Crystal Structure (Crystal Planes Were Modeled Using Vesta Software)

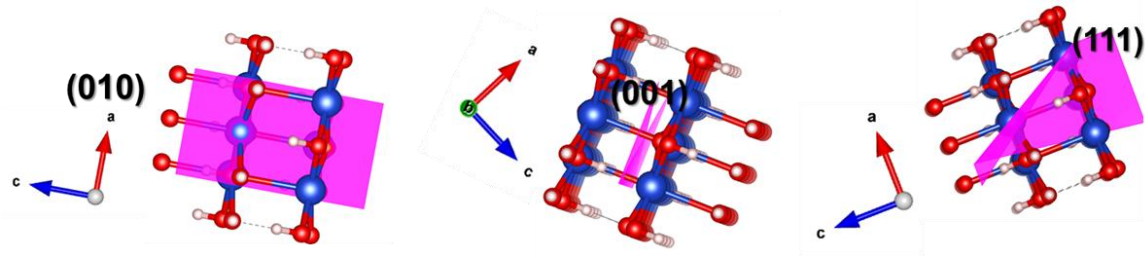

2.3.2 Surfactant assisted crystal growth

OA based one-dimensional nanostructures exhibit crystal growth along a specific crystallographic direction, which is determined by the different surface energies associated with their crystal facets.[134] The crystal growth rate is correlated exponentially to the surface energy.[135] The higher surface energy planes grow faster, while keeping the lower surface energy planes as the facets of the product. It has been reported that anatase TiO_2 nanocrystals grew in OA based one-dimensional necklace-shaped nanostructures along the [001] direction, which has the lowest surface energy, after the growth of {001} and {101} crystal faces.[136]

Surfactants are considered as a shape control tool, acting as a adsorbates or capping agents that significantly affect the formation and the growth rate of nanocrystals.[137] They can

interact with the reacting species in the growing nanocrystals and influence the growth kinetics, as well as the final shape of a material. They also can self-assemble in the solution to act as a template to tailor a material's shape.[138] Adsorption of solvents or surfactants to the growing nanocrystals can enhance or reduce the total crystal surface energy by selectively adsorbing into specific crystal facets with different binding affinities for the nanocrystal.[139] For example, when lauric acid was added to TiO_2 anatase nanocrystals, it adsorbed to the {001} crystal facet. It acted as a surfactant and reduced the surface energy in the [001] direction. This interaction resulted in the formation of nanorods by reducing the growth rate along [001] direction.[140] Cao-Thang et al. reported that TiO_2 nanocrystal morphologies, such as rhombic, spherical particles, and nanodots, were influenced by changing the molar concentration ratio of two surfactants, oleic acid and oleylamine.[141] These surfactants selectively bind {001} and {101} crystal faces with different binding strengths, which controls the growth rate of the TiO_2 nanocrystals. Therefore, nanocrystal shape is determined by the cooperative effects of growth of two crystal facets, between the [001] and [101] directions. This interaction yielded different morphologies at different molar ratios of surfactants.[141]

2.3.3 Role of bio-amphiphiles

While metal oxide syntheses have been reported in aqueous systems for decades, some limitations arise when preparing ultrathin nanowires. The major challenges include lack of crystallinity and making complex structures, due to the high reactivity of the metal precursors and the water, which is acting as ligand and solvent in the system.[142] Interestingly, biomimetic synthesis approaches, which involve surfactants or capping ligands in the reaction, overcome of this problem of synthesizing various ultrathin metal oxide nanostructures at low temperatures.[143,144] Selected examples of useful bio amphiphiles are proteins, peptides, cholesterol, collagen and lipids.

Amphiphiles are composed of hydrophilic and hydrophobic segments. For example, a phospholipid is the most important component in cell membranes. The bilayer membrane is a

self-assembled nanostructure whose function is to maintain membrane stability. The phospholipid can be anionic, cationic, zwitterionic, or non-ionic depending on the overall charge of the molecule. The driving force for the self-assembly of liposomes is the hydrophilic-hydrophobic interaction between the polar head group and the fatty acid tail. The polar head of amphiphiles enables them to coordinate with metals at the metal oxide surface in a relatively strong manner. The metal coordination strength strongly depends on the nature of the functional groups of amphiphile's polar head, their number, shape, and position of the function group in the molecule.[145] Further, the properties of the final structure can be controlled by tuning the properties of the building blocks in the self-assembly process.[146] Such properties are determined by the preparation conditions and the chemical nature of the biomolecule. These organic biomolecules can control the nucleation, crystal growth rate, and crystallographic facet of metal oxides, so as to effect the size and morphology of the final product.[147] Therefore, recently, the fabrication of novel complex hierarchical structures using hybrid inorganic–organic building blocks has gained more attention. This process exhibits the potential to achieve superior electrical, catalytic and optical properties, with applications from the semiconductor and electronics industries to the biosensor, biotechnology, and biomedical engineering sectors.[14,147]

2.3.4 Self-assembly of copper oxides with bio-amphiphiles

Several groups report the synthesis of CuO nanoparticles using various plant extracts[148–154] for different applications, such as antimicrobial activity,[155] electrochemical sensors,[156] catalysts,[157] and electrochemical capacitors.[158] Other organisms that are capable of synthesizing copper oxide nanoparticles include fungi[159], bacteria[160–162], and algae.[163,164] While there is considerable work on 2D and 3D CuO nanostructures, very few reports can be found on the biosynthesis of 1D nanostructures. Few years ago, self-assembled CuO nanorods were successfully synthesized with Aloe vera gel as a surfactant using a sonoemulsion method.[78] These researchers suggested that the mechanism of nanorod formation could be attributed to the oriented self-aggregation of the nanoparticles. Further, they also inferred that the reduction

of the crystal energy was driven by Aloe vera gel to only grow in one direction. Vey recently, Sundar et al. synthesized CuO nanowires using a fruit extract, which shows remarkable electrocatalytic property.[79] They mention that the possible mechanism for forming wire like structures may be due to OA based crystal growth.

2.4 Importance of transmission electron microscopy as an investigation tool for 1D nanostructures

Transmission electron microscopy (TEM) is a powerful instrument for obtaining structural and chemical information of nanoscale materials such as materials size, shape, crystallinity, composition, and elemental mapping.[165] This technique employs a high accelerating energy beam of electrons transmitted through a thin specimen. The general Bright-field TEM imaging mode enables characterization of the size, shape, and uniformity of a nanomaterial.[165] For nanocrystalline materials, electron diffraction (ED) associated with the TEM imaging mode is used to determine the crystal structure and the crystallographic orientation in a selected area.[166] With the advancement of TEMs, the scanning transmission electron microscope (STEM) mode generates images by performing a raster scan on the surface of the nanomaterial, coupled with a high-angle annular dark-field (HAADF) detector.[165] A relative quantitative elemental analysis can be performed with the energy-dispersive X-ray detector (EDX or EDS). It helps to confirm the chemical composition of the nanomaterials.[167] High-resolution TEM (HR-TEM) provides the crystal lattice structure and lattice spacing of a material. It is an invaluable tool to investigate crystal defects like twins, misorientation, and stacking faults, as well as phase transformation to study kinetics at the atomic level.[165,168]

Cryo-transmission electron microscopy (Cryo-TEM) can work with materials that are highly beam sensitive, like biological samples in a frozen-hydrated state, to reveal the crystallization pathways and kinetics.[169] More recently, in-situ and direct visualization using liquid-phase TEM greatly expanded the analytical power of the TEM. For example, some researchers investigated the crystallization pathways for different nanomaterials using liquid-

phase TEM.[68,170,171] Li and coworkers observed the oriented attachment of iron oxyhydroxide nanoparticles and calculated their relative translational and angular speeds using liquid-cell TEM.[66] Very recently, Song et al. studied the formation mechanism of five-fold twinned crystal domains using real time HR-TEM imaging.[172] This technique can help to clarify our understanding of crystallization dynamics and mechanisms. Therefore, Liquid-phase TEM serves as a critical tool for investigating crystal growth mechanism and their driving forces. Consequently, the rate of understanding of crystallization, nanocrystal nucleation, and corresponding growth processes and their dynamics using liquid-phase TEM will continue to grow for the foreseeable future.

CHAPTER III: SYNTHESIS OF ULTRATHIN $Cu(OH)_2$ AND CuO COLLOIDAL NANOWIRES

3.1 Introduction

Among all transition metal elements, copper (Cu) recently has received considerable attention as an alternative for expensive silver and gold, due to its high electrical conductivity and abundance. Copper hydroxide ($Cu(OH)_2$) is the hydroxide form, having an orthorhombic crystal structure and an indirect band gap of 1.97 eV.[32,33] Its metal oxide, cupric oxide (CuO) is a p-type semiconductor with a narrow and indirect energy band-gap of ~1.2 eV[19] with intriguing properties like environmental benignity, chemical stability, high catalytic activity, easy synthesis route, electrochemical activity, antimicrobial activity, abundance. CuO shows diverse morphologies at the nanoscale as such nanowires[34,35], nanoflowers[36–38], nanorods[39–41], nanoplatelets[42], nanotubes[40], nanobelts[34], nanoparticles[39,41], nanoleaves[38,43] and many more[2,9]. Therefore, it has been extensively investigated for diverse applications such as field emission, solar cells, heterogeneous catalysts, lithium ion batteries, high temperature superconductors[36–38,41,43–45]. However, the synthesis of one-dimensional nanostructures is most fascinating for wide range applications in electronic, magnetic and photonic devices due to their unique properties[173–175]. CuO NWs typically are synthesized via vapor phase evaporation[46,47] and direct thermal oxidation procedures[35,48–52]. However, most of these methods require complicated experimental procedures, high-cost, sophisticated equipment, rigorous experimental conditions, such as high temperature, pressure, inert atmosphere, and long reaction time. Fortunately, wet chemical synthesis represents a promising route in terms of cost, throughput, greener chemistry, and its potential for large-scale production in the industry[53,54]. Very few reports have been published for the synthesis of $Cu(OH)_2$ and CuO NWs using wet chemical synthesis, which often yielded other morphologies[38,53–57]. These syntheses often used either weak and strong bases, i.e. aqueous ammonia and NaOH/KOH solutions, or by the interaction between a copper complex and NaOH at the aqueous-organic interface. Despite this significant research

endeavor, there remains a lack of effective methods for large-scale production of high-quality ultrathin nanowires with precise morphological control for higher aspect ratio. Nanowires typically have aspect ratios greater than 20, which is defined as the length of the major axis divided by the width of the minor axis[26]. For one pot syntheses, a quick and simple reaction with the proper molar ratio of precursors for higher aspect ratio is still lacking. Therefore, we need to develop a simple and effective method to synthesize $Cu(OH)_2$/CuO nanowires at lower temperatures and shorter reaction times, which can easily scale up for production.

The sol–gel process is a widely used greener wet-chemical technique for the fabrication of different metal oxides nanostructures via low temperature multistep processes, such as hydrolysis, condensation, drying, and densification[102]. While the shape of metal oxide crystals is often related to the intrinsic unit cell structure, the same material can exhibit diverse crystal morphologies. These outcomes are influenced by the surface energies of the crystal facets and by the external growth environment, i.e., the growth rate of a crystal facet. For non-classical crystal growth, oriented attachment (OA) of nanoscale “building blocks” represents as significant mechanism for growing to nucleated seeds[176]. The OA mechanism differs significantly from random coalescence (RC) in the orientation of the crystal lattice at the grain boundary. In the RC process, there is no particular preference for the attachment and the lattice planes are randomly orientated between domains[177]. In contrast, with the OA mechanism, the nanoparticles attach in a common crystallographic orientation and there is a perfect alignment of the planes. Highly ordered monocrystalline materials can be formed through OA, which is a versatile approach for the preparation of anisotropic nanostructures.

In this work, we explore a facile and cost-effective route to synthesize $Cu(OH)_2$ and CuO nanowires by sol-gel hydrolysis followed by the directed self-assembly and crystal growth of nanocrystals at room temperature in DI water. The optical properties of the synthesized nanowires were investigated by UV-Vis spectroscopy. The time-dependent analyses were performed using transmission electron microscopy to identify the OA crystal growth process for

the formation of 1D nanostructures. The crystallinity was evaluated from powder X-ray diffraction traces of nanowires. The chemical composition and formula of the nanowires were analyzed by x-ray photon spectroscopy (XPS).

3.2 Materials and methodology

3.2.1 Materials

Copper(II)acetate monohydrate (98-102.0 % powder) was purchased from Alfa Aesar. Sodium hydroxide (98 % purity) and ethanol (anhydrous, 99.5 % purity) were obtained from Sigma Aldrich. They used as received without any purification otherwise specified.

3.2.2 Synthesis of $Cu(OH)_2$ colloidal nanowires and CuO nanowires

To a 10 mL volumetric flask, copper(Ⅱ)acetate monohydrate ($Cu(CH_3COO)_2.H_2O$, 40 mg, 0.2 mmol) was dissolved in 10 mL deionized (DI) water to make 0.02 M Cu^{+2} homogeneous stock solution. Separately, to a 10 mL volumetric flask, sodium hydroxide (NaOH, 40 mg, 1.0 mmol) was dissolved in 10 mL DI water to form a homogenous solution. To a 20 mL glass vial, the Cu^{+2} precursor solution (1.25 mL) taken from the stock solution was added. While it was stirring gently in a magnetic stirrer, the base, NaOH (1.25 mL) from the stock solution was added slowly at the rate of 0.25 mL/min over 5 minutes to yield a blue color suspension. The experimental setup was illustrated in Figure 3.1. Then the reaction was capped and stirred for 4 hours at room temperature (24 °C) while monitoring the reaction progress at different time intervals. With the reaction proceeds, initial blue color was changed to blueish green over 4 hr period. The suspension prepared in this manner was kept in the refrigerator at 5 °C for 24 hours aging. The color of the reaction mixture was changed from blueish green to green during the aging process. The green suspension was centrifuged and washed with DI water three times to remove salts and leftover starting materials. Without air drying, the wet green solid of $Cu(OH)_2$ nanowires was resuspended in DI water (~1 mL) and transferred to a glass vial to yield a wet paste. The furnace was preheated to 300 °C and the sample in the glass vial was

annealed at 300 °C for one hour to yield a black powder of CuO nanowires (~1.5 mg). The annealing process was also conducted for a drop-casted sample on Si wafer and performed the morphology and composition analysis (SEM, and XPS) along with the sample annealed on the Si wafer.

Figure 10: Experimental Setup of Fabrication of $Cu(OH)_2$/CuO NWs

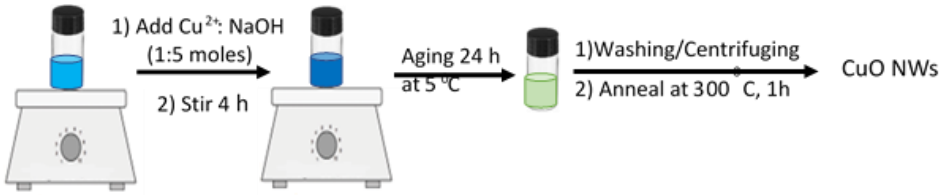

3.2.3 Characterization

The morphologies and dimensions of all nanomaterials were analyzed using transmission electron microscopy (TEM Carl Zeiss Libra 120 and JEOL 2100PLUS HR-TEM) at 120 keV and 200 keV and scanning electron microscopy (Zeiss Auriga FIB/FESEM). SEM analysis was performed as prepared samples on the Si substrate without sputter coating for any additional conductive layer on it. The Atomic concentrations and binding energies of all the elements present in nanowires were obtained from X-ray photoelectron spectroscopy (XPS) using XPS-Escalab Xi+ Thermo Scientific electron spectrometer. The UV-visible spectra of $Cu(OH)_2$ nanowires while stirring at different time intervals were obtained in the solution without washing, using ultraviolet-visible spectroscopy (Varian Cary 6000i). The re-suspended product was drop casted on a cleaned Si substrate and XPS spectra was performed after dried it completely in the fume hood. The powder XRD analysis was conducted using Cu Ka radiation (40 kV, 40 mA, k=1.54 °A) with a speed of 90 s on the X-ray diffractometer (XRD, Agilent technologies Gemini). The powder XRD spectra of $Cu(OH)_2$ NWs were obtained for the glass fibers coated with washed wet green suspension and dried completely in the fume hood. For CuO NWs, the glass fibers coated with washed wet green suspension was annealed at 300 °C

for one hour in a preheated furnace. The visualization software VESTA was used to compute the theoretical XRD from the CIF files. The experimental XRD was matched with the simulated XRD pattern.

3.3 Results and discussion

3.3.1 The directed self-assembly process for the formation of $Cu(OH)_2$ nanoarrays and CuO nanowires

The $Cu(OH)_2$ nanocrystals were prepared from the NaOH base-catalyzed hydrolysis of an aqueous solution of copper acetate ($Cu(CH_3COOH)_2$) at room temperature. The molar ratio of the precursor to the base was maintained at 1:5 to yield nanowire structures. The $Cu(OH)_2$ sols were prepared from the sol-gel hydrolysis process and then colloidal self-assembly of nanocrystals were grown the 1 D $Cu(OH)_2$ nanowires after aging at 5^0C. After annealing of $Cu(OH)_2$ nanowires at 300 ^{0}C at 1 hr, the CuO nanowires were fabricated, as shown in Figure 11.

Figure 11: The Chemistry and Self-Assembly Process For The Formation of $Cu(OH)_2$ Nanoarrays and CuO Nanowires.

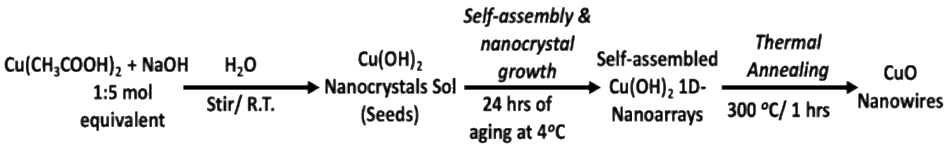

3.3.2 The UV-vis analysis of $Cu(OH)_2$ colloidal NWs

The UV-visible absorption spectra of the reaction mixture were taken at each stage of the process, i.e., after NaOH was added, at different stirring time intervals, and after aging. As in Figure 12(a), the initial absorption maxima of the precursor solution ($Cu(CH_3COOH)_2$) was observed at 770 nm. After the addition of NaOH progresses, the absorption band shifted to a shorter wavelength region at 660 nm. This absorption band shift supports changes in the

electronic properties of the material after the addition of NaOH. The broad peak at 660 nm can be assigned to the Cu(II) d–d transition of $Cu(OH)_2$ NWs.[178] After stirring the mixture for 4 hrs, the reaction mixture was aged for 24 hrs at 5 ^{0}C. Figure 12 (a & b) shows the UV-visible spectra at different stirring time intervals and different stirring time intervals.

Figure 12: UV-visible Spectra Taken At Different Stirring Time Intervals In The Suspension and (b) After 24 hrs Aging During The Synthesis of $Cu(OH)_2$ Nanowires.

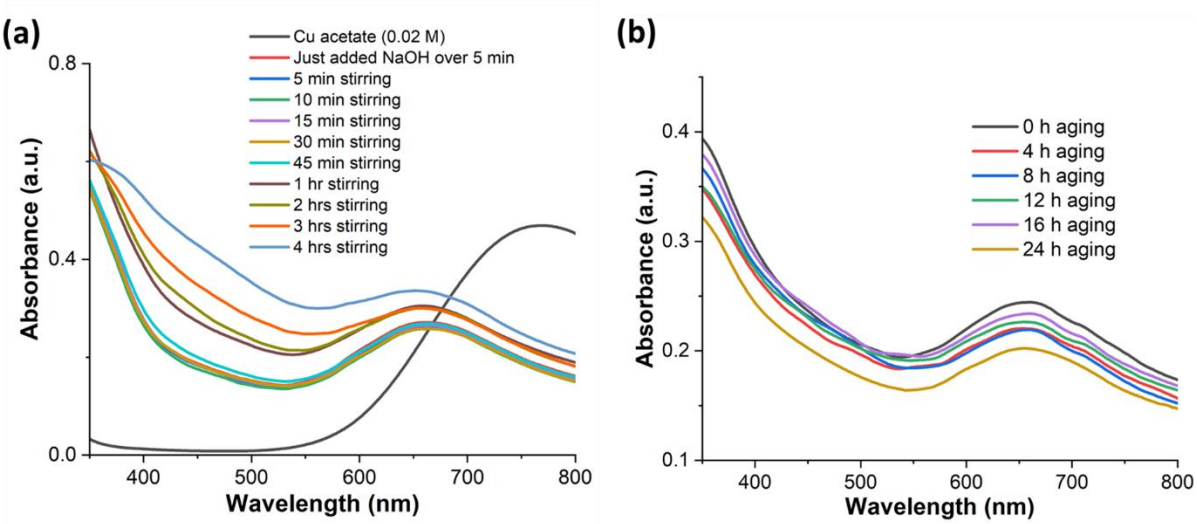

The Gauss peak fitting was performed to quantitatively estimate the maximum peak wavelength for the distorted UV-vis spectra at different stirring times and aging times. The peak wavelength was reported after fitting each spectrum with a single Gaussian peak, after subtracting the background using a polynomial curve at different time intervals, as shown in Appendix A.[179] The regression coefficients of all the fitted curves were maintained at ≥0.999 precision. The average peak wavelength is 663.2±1.6 nm, as shown in Table 2, which confirms the formation of $Cu(OH)_2$ nanowires. These findings confirm the electronic structure changes due to the chemical reactions of $Cu(OH)_2$ in the sol-gel process.

Table 2: Summary of Gauss peak fitting analysis at different time intervals (Just added NaOH over 5 min was added to the total stirring time).

Time	Max. peak wavelength after Gauss fitting (nm)	SD (±nm)	Absorbance at 660 nm (a.u.)
5 min stirring	663.6	0.1	0.21
10 min stirring	662.7	0.1	0.21
15 min stirring	663.4	0.1	0.20
20 min stirring	663.1	0.1	0.21
35 min stirring	663.1	0.1	0.20
50 min stirring	662.7	0.1	0.21
65 min stirring	660.8	0.1	0.26
125 min stirring	661.4	0.1	0.26
185 min stirring	665.2	0.1	0.27
245 min stirring	664.6	0.1	0.24
4 hrs aging	661.9	0.1	0.22
8 hrs aging	659.1	0.1	0.23
12 hrs aging	659.5	0.1	0.23
16 hrs aging	660.0	0.1	0.23
24 hrs aging	664.5	0.1	0.20
Average ±SD	662.4± 1.6		

The variation of absorbance intensity at 660 nm which corresponds to the changes in chemical reactions of $Cu(OH)_2$ during each stirring and aging time intervals of the sol-gel process is shown in Table 2. The absorbance intensity after addition of NaOH to 50 min stirring is constant (~ 0.20) and then has increased to 0.26) at 65 min stirring. The steady absorbance maxima can be seen from 65 min stirring to 185 min stirring time intervals. During aging, the

absorbance was decreased to 0.23 at 4 hours and then absorbance is constant until 16 hours aging and finally at 24 hours aging it was decreased to 0.20. This absorbance intensity changes indicate the chemical processes consisted in the sol-gel process.

3.3.3 The effect of stirring and aging on morphology of nanowires

Figure 13: TEM Images Taken At Different Time Intervals Over 4 hrs Just After The Addition of NaOH Solution.

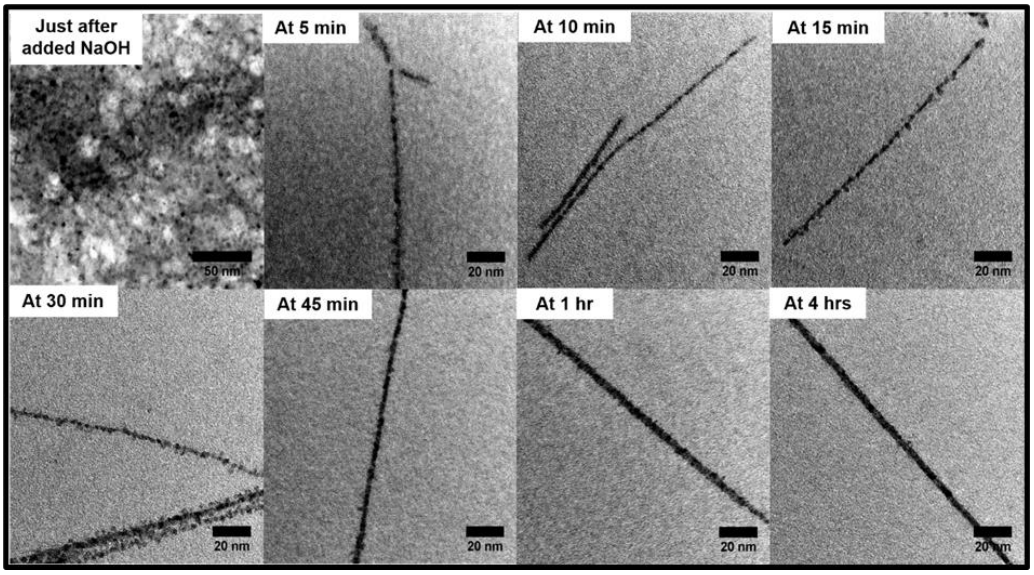

The self-assembly of nanocrystals and nanowire formation at each time interval were also monitored with a TEM to provide insight into the OA-based crystal growth mechanism. As shown in Figure 13, the TEM image just after adding NaOH shows highly aggregated, irregular shapes, and small nanocrystals with sizes ranging from 2-4 nm. After 5 minutes stirring, these small nanocrystals have started to self-assemble into one direction, with the nanocrystals coalescing in a specific crystallographic orientation. After 1 hr and 4 hrs stirring, the colloidal nanowires tend to form smooth surfaces and single elongated nanocrystals. The dimensional analysis of $Cu(OH)_2$ nanowires at different stirring time intervals is shown in Table 3. Between 15 minutes and 4 hrs of stirring, the average diameter remained constant at 5±2 nm throughout the reaction. The crystal growth was observed along the long axes of nanocrystals and

increased the average nanowire length. The initial length of nanowires after 5 minutes stirring is 46.1 ± 26.8 nm. After 4 hrs stirring, the nanowires reached an average length of 119.4± 72.5 nm. The high standard deviation attributes the wide length distribution of nanowires.

Table 3: The dimension analysis of $Cu(OH)_2$ nanowires at different stirring time intervals (Sample size = 50) (The addition of NaOH over 5 minutes was included to the total stirring time)

Stirring time (min)	Average length (nm) ± SD (1σ)	Average diameter(nm) ± SD (1σ)
5	44.2± 30.7	2.8± 0.7
10	46.1± 26.8	2.8± 0.7
15	57.4± 33.6	3.2± 0.5
20	62.4± 43.7	3.2± 0.7
35	75.6± 41.7	3.6± 0.7
50	83.3± 44.1	3.5± 0.8
65	87.9± 47.2	3.7± 1.0
125	101.2± 64.3	4.2± 1.0
185	114.3± 70.3	4.2± 1.2
245	119.4± 72.5	4.2± 1.1

Table 4 summarizes the dimensional analysis of nanowires after aging at 5 ^{0}C. The average nanowire diameter is appeared to be constant throughout aging time. The average maximum nanowire length further increased up to 12 h aging and then it is constant for 24 h aging. The synthesized ultrathin $Cu(OH)_2$ nanowires after 24 h aging were fully grown with an average length of 172.2±98.3 nm. Figure 14 shows the TEM images of fully grown $Cu(OH)_2$ nanowires after aging that exhibit stacks of hair like wires.

Table 4: Length and diameter of $Cu(OH)_2$ NWs with respect to different aging time after 4hrs of stirring. (Sample size = 50)

Aging time (h)	Average length (nm) ± SD (1σ)	Average diameter(nm) ± SD (1σ)
0	119.4± 72.5	4.2± 1.1
4	140.1± 99.9	3.9± 1.0
8	147.6± 84.5	3.9± 1.0
12	171.3± 128.5	4.6± 1.1
16	176.2± 105.8	4.1± 1.5
24	172.2±98.3	4.2± 1.3

Figure 14: TEM Images of Fully Grown $Cu(OH)_2$ Nanowires After (a) 6 hrs (b) 24 hrs Aging.

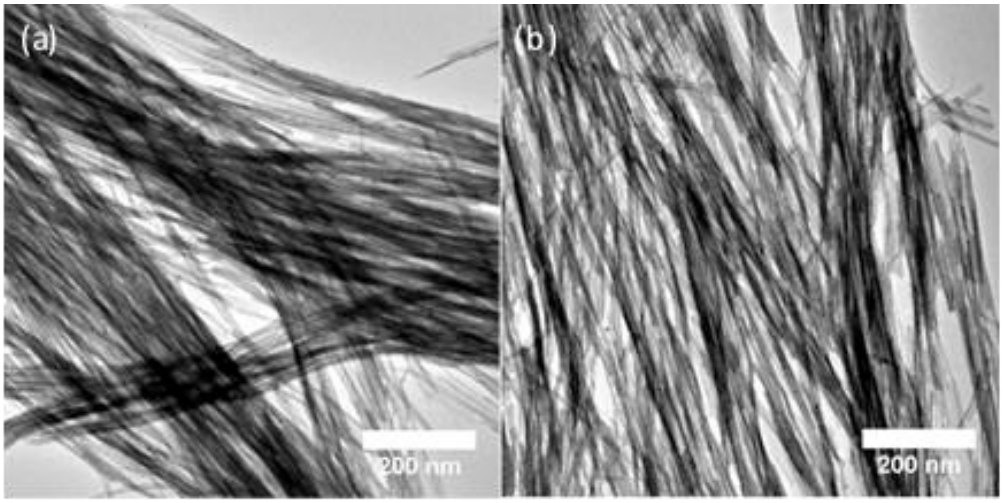

3.3.4 The time-dependent study on nanocrystals growth and crystallinity of $Cu(OH)_2$ nanowires

The crystal growth mechanism was further investigated by the time-dependent study on nanocrystals growth of $Cu(OH)_2$ nanowires using XRD, and determined their crystallinity from

Selected Area Electron Diffraction (SAED) patterns, as shown in Figure 15. The SAED patterns exhibit the gradual growth of ring patterns with increasing stirring time. For example, after 30 minutes stirring, the SAED pattern shows a few dot patterns with discontinuous rings. The synthesized $Cu(OH)_2$ nanowires after 24 hr aging show well-resolved dense crystal dot pattern with a clear trend in directional crystal growth. These observations confirm the assertion that $Cu(OH)_2$ nanowires have higher crystallinity.

Time-dependent powder XRD analysis revealed the gradual coalescence, re-orientation, and growth of crystal facets with different stirring and aging times. The synthesized $Cu(OH)_2$ NWs after 24 hrs aging are highly crystalline and exhibit six main diffraction planes; (020), (021), (002), (130), (150), and (152) at 2Ɵ (16.80^0, 23.93^0, 34.05^0, 39.81^0, 53.41^0, 63.02^0) values that can be indexed to the orthorhombic crystal unit cell of $Cu(OH)_2$.[180] With longer stirring, two less intense broader Bragg's peaks are visible, corresponding to [150] and [152] reflection planes, along with three main reflection planes. After 45 minutes stirring, the [020] crystal diffraction plane emerges, demonstrating nanowire growth by fusing nanocrystals along the [020] crystal facet. The synthesized NWs after 24 hrs aging exactly match the simulated diffraction pattern of the orthorhombic unit crystal (Figure 16), confirming the formation of $Cu(OH)_2$ nanowires.

Figure 15: Time Dependent SAED Patterns Along With Powder XRD Traces of $Cu(OH)_2$ Colloidal Nanocrystals At The Stirring Time of: (a) 30 min, (b) 45 min, (c) 1 hr, (d) 2 hr, (e) 3 hr, (f) 4 hr, and (g) 4 hr Followed By 24 hr Aging.

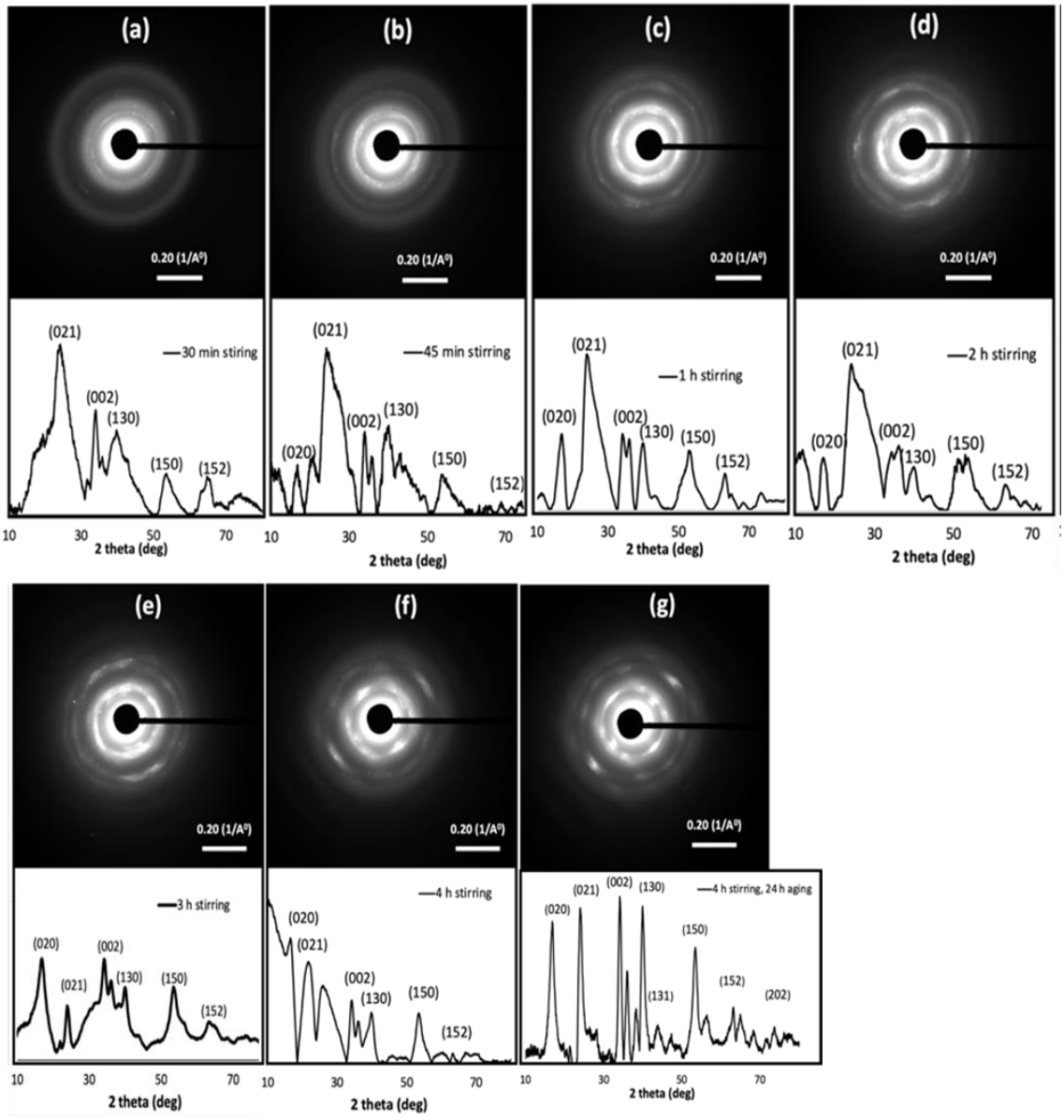

Figure 16: (a) The Simulated And Experimental Powder XRD Patterns of $Cu(OH)_2$ Nanowires (b) Orthorhombic Crystal Unit Cell Obtained From The Crystallographic Open Database (COD #9007849)

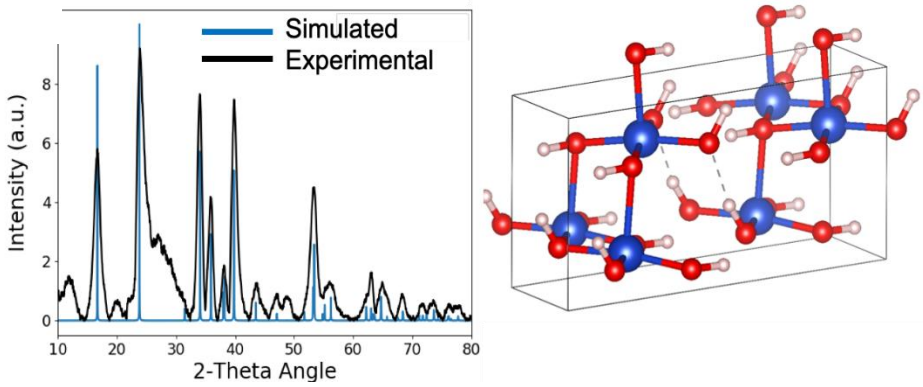

3.3.5 The composition and oxidation states of $Cu(OH)_2$ nanowires

To investigate the elemental composition and oxidation states of synthesized nanowires, X-ray photoelectron spectroscopy (XPS) analysis was conducted (Figure 17). The XPS survey spectra confirms the presence of Cu and O, with an atomic ratio of 1:2, as depicted in Table 5. It confirms the chemical composition of $Cu(OH)_2$ nanowires and the formation of high purity $Cu(OH)_2$ nanowires. The binding energy spectra for Cu *2p* and O *1s* have are shown in Figure 17 (b) and (c), respectively. Two major peaks in the Cu *2p* binding energy spectrum, at 933.9 eV and 954.7 eV, are attributed to the binding energy states for Cu $2p_{1/2}$ and Cu $2p_{3/2}$ of Cu–O bonds in $Cu(OH)_2$.[181] The presence of two less intense satellite peaks along with two major peaks indicate the presence of Cu(II) ions.[181] The more positive binding energies of the Cu *2p* energy state and the corresponding larger FWHM (Full Width at Half Maximum) of 6.05 eV, confirms the presence of the hydroxide form. Furthermore, there is a well-resolved single peak for O *1s* at 530. 5 eV, with a larger FWHM (4.47 eV), which supports the chemical bonding state of O^{-2} with the hydroxide form.

Table 5: XPS analysis of $Cu(OH)_2$ nanowires

Peak	Position BE (eV)±0.10 eV	FWHM (eV) ±0.20 eV	Atomic Con. (%)
Cu $2p_{1/2}$; Cu $2p_{3/2}$	934.9, 955.0	6.05	31.82
O 1S	530.5	4.47	62.54

Figure 17: The XPS Spectra of $Cu(OH)_2$ Nanowires; (a) The Survey XPS Spectrum, And The Binding Energy Spectra of: (b) Cu *2p* and (c) O *1s*

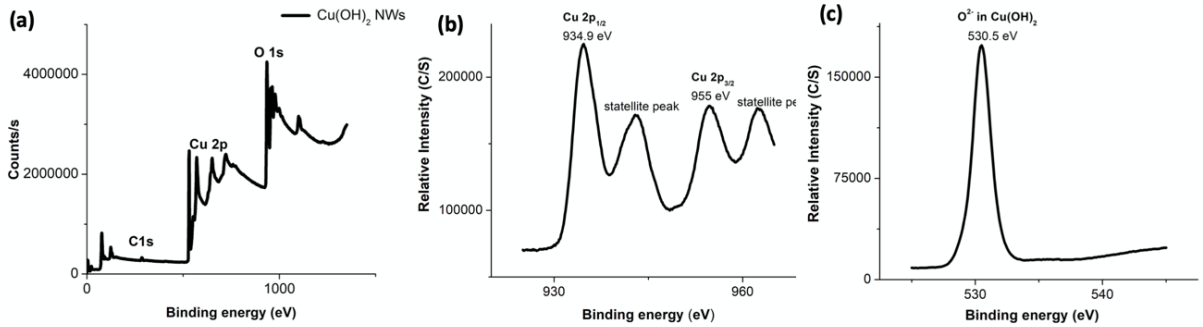

3.3.6 The thin film UV-visible analysis of CuO nanowires

The thin film UV-visible spectrum obtained after annealing $Cu(OH)_2$ nanowires at 300 °C shows an absorption maximum at 292 nm, as shown in Figure 18. It This spectrum supports the formation of CuO from the $Cu(OH)_2$ after the annealing.

Figure 18: The Thin Film UV-visible Spectrum of CuO Nanowires

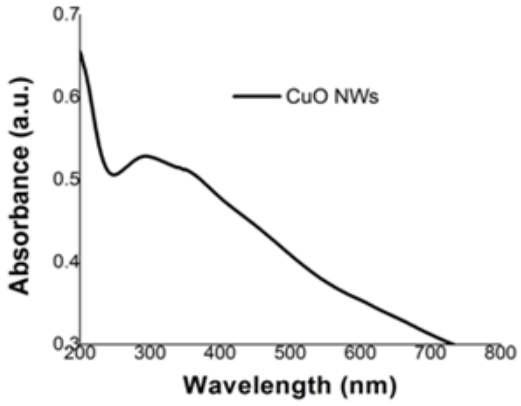

3.3.7 The crystallinity of CuO nanowires

After annealing, the synthesized CuO NWs are highly crystalline, as that exhibited in the characteristic diffraction pattern shown in Figure 19, which is different from the corresponding pattern for $Cu(OH)_2$ NWs. The XRD pattern of CuO NWs has diffraction peaks, which index to [110], [002], [111], [112], [020], [202], [113], [220] and [004] planes. These data confirm the formation of pure CuO NWs, indicating that $Cu(OH)_2$ is completely converted to CuO upon annealing. There are two main diffraction planes in the XRD pattern; [002]/[$^{-}$111], and [111] at 2Ɵ (35.55° and 38.81°) values, respectively. These observations support the favorable crystal growth direction of NWs as the along the both crystal facets of the [$^{-}$111] and [111] planes. The simulated XRD pattern matched the experimental XRD pattern, as depicted in Figure 20, confirming the monoclinic crystal structure of CuO NWs.

Figure 19: **The Powder XRD Spectrum of CuO Nanowires**

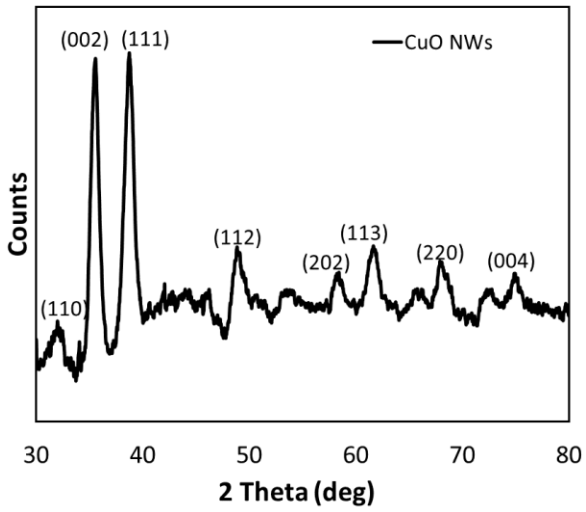

Figure 20: (a) The Simulated and Experimental Powder XRD Patterns of CuO Nanowires (b) Monoclinic Crystal Unit Cell Obtained from The Crystallographic Open Database (COD #9016326)

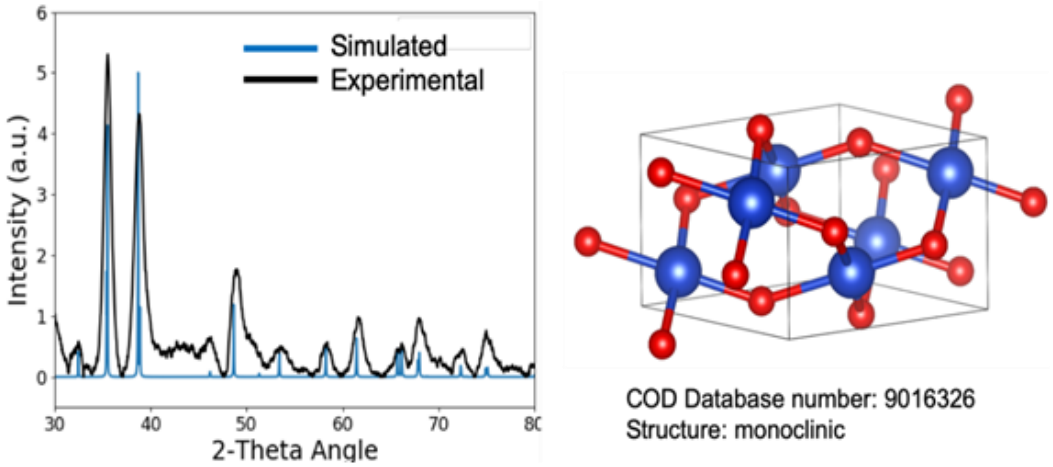

3.3.8 The composition and oxidation states of CuO nanowires

As depicted in Figure 21(a), the XPS spectrum shows the presence of Cu and O elements with an atomic ratio is ~1:1, further supporting the purity of CuO NWs. The binding energy spectrum corresponds to Cu *2p,* as shown in Figure 21(b), shows the two dominant peaks at 933.1 and 953.5 eV with their respective less intense satellite peaks. It further confirms the presence of divalent Cu rather than Cu(0).[181–183] The binding energy spectrum corresponds to O *1s* in Figure 22(c) has a well-resolved single peak at 528. 7 eV. As in Table 6, the binding energy of CuO is ~1.8 eV lower than the O *1s* binding energy of synthesized $Cu(OH)_2$ NWs. Also, the FWHMs of 3.02 eV and 0.94 eV are narrower for Cu *2p* and O *1s*, respectively. Since the binding energy of O *1s* for the oxide form is usually lower by ~ 1.2 eV, with a very narrow FWHM, it further confirms the oxygen chemical bonding state of O^{-2} in the oxide form.

Table 6: XPS analysis of CuO nanowires

Peak	Position BE (eV)±0.10 eV	FWHM (eV) ±0.20 eV	Atomic Con. (%)
Cu $2p_{1/2}$; Cu $2p_{3/2}$	933.1, 953.0	3.02	40.50
O 1S	528.7, 530.5	0.94	42.96

Figure 21: The XPS Spectra (a-c) of CuO NWs; (a) The Survey XPS Spectrum, and The Binding Energy Spectra of: (b) Cu *2p* and (c) O *1s*

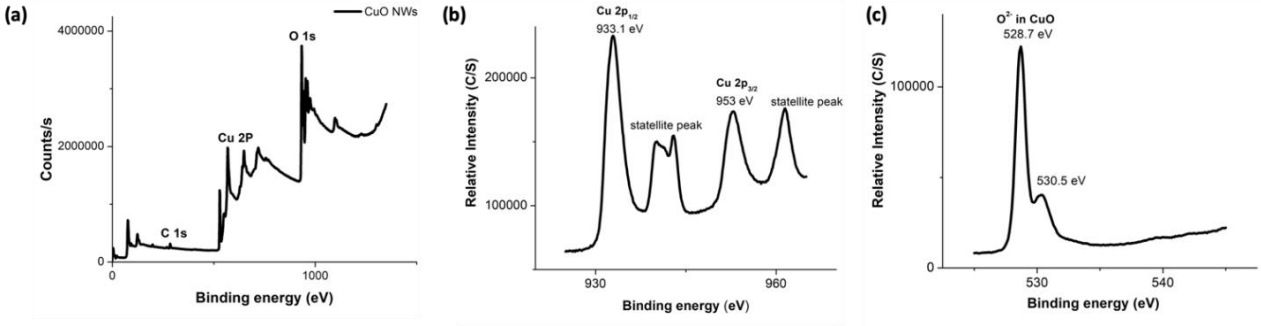

3.3.9 The morphology of CuO nanowires

As shown in Figure 22, the morphology of CuO nanowires exhibits stacks of very thin hair like, continuous single crystalline wires with very smooth surfaces. However, in some circumstances, e.g., 1 hr stirring followed by 6 hrs aging and annealed, we can see that nanowires disassembled into nanocrystals after the annealing process, as shown in Figure 22(b). These nanocrystal seeds are the building blocks, that eventually grow into the colloidal nanocrystal arrays. This temperature induced assembly and disassembly behavior may be due to the incomplete nanocrystal fusion and growth processes to form single nanowires, with the lower stirring and aging times. The dimensional analysis of CuO nanowires with different aging times are presented in Table 7. The average diameter was found to be constant at 27±3 nm, independent of the aging time. Moreover, the average diameter of CuO nanowires are ~4-fold larger than the average diameter of $Cu(OH)_2$ nanowires. However, the maximum average length

of synthesized CuO nanowires was 7.4±0.3 µm, which is ~10-fold shorter than the average length of $Cu(OH)_2$ nanowires. Correspondingly, the calculated aspect ratio of fabricated CuO nanowires is 280.9±18.0, which is estimated by dividing the average maximum average length divided by the average diameter of the nanowires.

Figure 22: SEM Images of CuO Nanowires Fabricated From $Cu(OH)_2$ Nanowires, (a), (b) After 1 hr Stirring Time Followed By 6 hr aging, and (c), (d) After 4 hrs Stirring Time Followed By 24 hrs Aging; Upon Annealing On Si-substrate At 300 °C, An Hour.

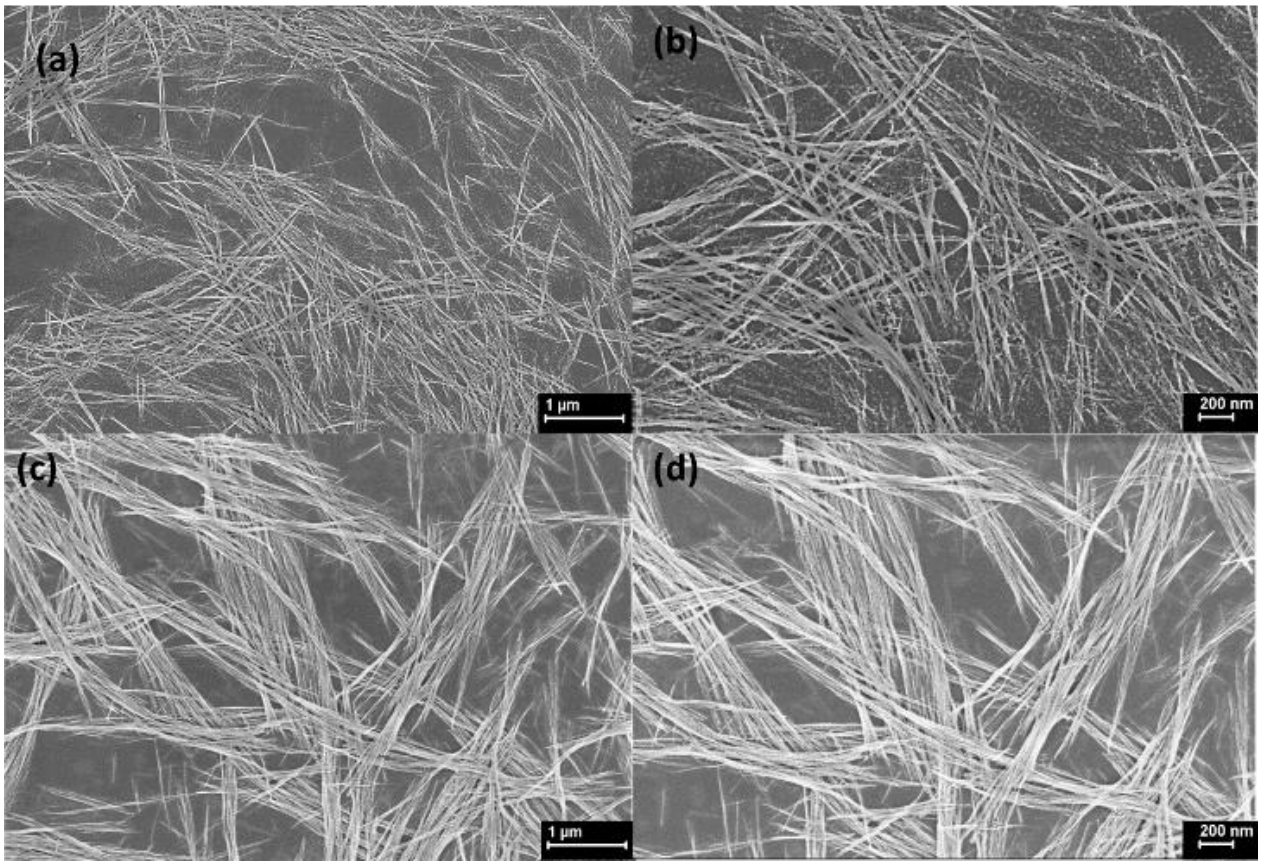

Table 7: Length and diameter of CuO NWs produced upon annealing $Cu(OH)_2$ nanowires, which were made at 4 hours stirring followed by 6 hours and 24 hours aging respectively. The powder samples of $Cu(OH)_2$ nanowires were annealed at 300 °C, an hour. (Sample size = 50)

Aging time [h]	Average Maximum Length(μm) ± SD	Average Diameter (μm) ± SD
6	5.5±0.1	27.9±3.5
24	7.4±0.3	26.5±2.4

3.4 Conclusions

Here, we developed a facile, greener, base-catalyzed sol-gel approach, followed by directed self-assembly and OA-directed nanocrystal crystal growth, to make ultrathin $Cu(OH)_2$ and CuO nanowires. After the synthesis and 24 h aging, the average length and diameter of fully grown $Cu(OH)_2$ nanowires is 172.2± 98.3 and 4.2± 1.3 nm, respectively. We performed in situ monitoring of $Cu(OH)_2$ nanocrystal self- assembly and growth under the transmission electron microscope at different reaction time intervals to observe the OA crystal growth process to form ultrathin $Cu(OH)_2$ nanowires. The time dependent powder XRD traces and SAED TEM patterns show the crystallinity of produced nanowires. Also, XRD analysis shows the packing pattern of $Cu(OH)_2$ nanowires can be indexed to orthorhombic crystal unit cell. The powder XRD trace analysis confirms crystal growth of OA directed $Cu(OH)_2$ nanowires are along the [020] and [021] crystal facets. The respective XRD and XPS spectroscopies confirm the chemical composition of $Cu(OH)_2$ nanowires and their purity. High aspect ratio of 1D CuO nanowires were fabricated via post annealing of $Cu(OH)_2$ nanowires. Their average length is 7.4 ± 0.3 μm and average diameter is 26.5± 2.4nm, with an aspect ratio of 280 ±18. XRD analysis shows the crystallinity of CuO nanowires and their crystal growth along the crystal facets of [002] and [111]

reflection planes. Overall, we demonstrated the OA-directed crystal growth approach to make ultrathin 1D $Cu(OH)_2$ and CuO nanowires. This process for fabricating ultrathin $Cu(OH)_2$ nanowires and high aspect ratio CuO nanowires could serve as a cheap and effective methodology for the semiconductor industry, electronics industry, and sensors, enabling wide applicability in 21st century emerging technologies, such as dissolvable prosthetics.

CHAPTER IV: MECHANISTIC CRYSTAL GROWTH STUDIES OF ANISOTROPIC ULTRATHIN $Cu(OH)_2$ NANOWIRES

4.1 Introduction

The crystallization and growth of crystals from solution through classical and non-classical pathways is very important fundamental processes in the field of nanoscience. Considerable attention has been devoted to tailor the size and shape of crystalline semiconductor nanomaterials to obtain their desired properties for a variety of applications such as electronic devices, energy storage devices, optical devices, and gas sensors.[8–11] The crystal growth mechanism, phase transformation, and kinetics for different solution-based synthetic procedures are reported for diverse morphologies.[5,113,114,184,185] However, efforts to study the detailed formation of anisotropic nanomaterials have only recently begun. Numerous sources of evidence challenge several current in-situ interpretations of anisotropic crystal growth mechanisms at atomic-scale.[186] The real time crystallization dynamics of these one-dimensional (1D) nanostructures, including the emergence of individual nanocrystals and their self-assemblies into ordered structures, remain elusive and are crucial to understand the guiding principles that control the anisotropy of these nanomaterials.

Recent emergent techniques, such as liquid-phase atomic force microscopy and cryo-transmission electron microscopy (Cryo-TEM), reveal the real-space imaging of nuclei, intermediate structure formation, and crystallization kinetics.[187–189] More recently, the in-situ and direct visualization of crystallization pathways for different nanomaterials has been experimentally investigated using liquid-phase TEM.[66,68–71] Consequently, the rate of understanding of crystallization, nanocrystal nucleation, and corresponding growth processes and their dynamics using liquid-phase TEM continues to grow. However, this technique requires careful interpretation and is limited to a few synthetic systems, due to the electron beam and substrate effects and to the complexity of synthetic procedures.[76,77] Therefore, time-resolved,

static, high-resolution TEM (HR-TEM) images that show nucleation and self-assemblies of nanocrystals have been frequently accepted as experimental evidence for clarifying the crystallization dynamics and formation mechanisms.

The classical Ostwald ripening crystal growth mechanism (OR) is mainly described as the diffusion controlled coarsening mechanism to decrease the total surface free energy of particles. It asserts that the concentration of atomic species is higher at the surface of small particles than large particles. Therefore, the evolution of the particle size distribution in a solution, due to competitive growth, induces a concentration gradient around the surface of these particles caused by the thermodynamic demand.[190] The phenomenon is well-described by the Gibbs-Thompson relation, as the dissolution of small clusters to grow larger clusters at near equilibrium conditions.[191,192] However, the OR mechanism fails to explain the crystal growth of particles in many circumstances, especially in the nano regime.[5]

The Oriented attachment (OA) mechanism is non-classical growth path that is often observed and recognized as a fundamental nanoscale nanoparticle growth mechanism.[5,6] OA growth involves spontaneous self-organization of adjacent particles through Brownian motion along a specific crystallographic orientation. The primary nanocrystal colloids in a solution rotate for a crystal facet match and initiate the coalescence of nanocrystals, eliminating their misaligned interfaces and reducing their combined surface energy. Therefore, OA-based crystal growth is thermodynamically controlled, reducing the surface energy by minimizing the area of high energy crystal surfaces.[5–7] This mechanism exhibits unprecedented advantages for the formation of different anisotropic nanomaterials with uniform diameter.[185] For example, ultrathin nanowires, with diameters <10 nm, offer interesting characteristics such as new surface determined structures, with tunable surface chemistries, higher surface area, and higher colloidal stability.[1,193] These improved overall features are of great of interest in a variety of optical, electrochemical, thermoelectric and electronic applications.[29,30,194,195] OA offers a most

promising strategy to fabricate ultrathin nanowires with constant diameter, which follows the diameter of the primary nanocrystals.[1]

In OA growth, the crystal growth rate correlates exponentially with the surface energy.[135] The higher surface energy planes grow faster, while keeping the lower surface energy planes as facets of the product. Adsorption of solvents, surfactants, or ligands to the growing nanocrystals can enhance or reduce the total crystal surface energy by selectively adsorbing onto specific crystal facets with different nanocrystal binding affinities.[139] For example, when lauric acid is added to anatase TiO_2 nanocrystals, it adsorbs onto the {001} crystal facet. It acts as a surfactant, thereby reducing the surface energy along the [*001*] direction. It formed of nanorods by reducing the growth rate along the [*001*] direction.[196] Cao-Thang et al reported the shape control of TiO_2 nanocrystals, such as rhombic, spherical particles, and nanodots, by changing the molar concentration ratio of two surfactants, oleic acid and oleylamine.[141] These surfactants selectively bind to {001} and {101} crystal faces, respectively, with different binding strengths, which control the growth rate of the TiO_2 nanocrystals. Therefore, Nanocrystals shape is determined by a cooperative effect of growth rates of two crystal facets between the [*001*] and [101] directions, which yields different morphologies at different surfactant molar ratios.[141]

Crystal growth kinetics mainly depend on the nature of the material, the crystal facet interface, the reaction temperature, the type of surrounding solution, and the concentration of the surfactant.[114] Both OR and OA kinetic models were developed based on the nanoparticle's diameter growth.[4,5,113] Two reports attempted to explain the elongation kinetics of one-dimensional nanorods by considering dipole attraction for their alignment.[120,127] Up to now, none of the studies considered oriented attachment crystal growth kinetics, with respect to length, for making nanowires. Therefore, the development of new kinetic models is needed to understand, prepare, and control morphology of 1D nanostructures, such as metal hydroxide/oxide nanowires.

This work describes crystal growth mechanisms that explain the formation of ultrathin $Cu(OH)_2$ nanowires using time dependent in-situ high-resolution transmission electron microscopy (HR-TEM) imaging combined with UV-visible spectroscopy. It also predicts the driving forces and controlling factors in this novel, sol-gel derived synthesis. We introduce a novel kinetic model for size and shape-controlled 1D nanostructures, such as metal hydroxide/oxide nanowires, that considers the directed growth of the length. Here, using time-dependent HR-TEM imaging, we show nanocrystals formation, i.e., sol formation, self-assembly of nanocrystal seeds to one orientation, and nanowire formation. The time dependent HR-TEM shows the crystal lattices and their crystallographic direction, which enable to explain the crystal growth mechanism during each stage of the sol-gel process, which particularly involve three major stages – hydrolysis and condensation, polycondensation, and gelation. The hydrolysis and condensation process yields sol by base catalyzed hydrolysis. The condensation step follows the self-assembled nanocrystal growth along a selected crystal facets by condensation of nanocrystals. The gelation is the second stage of the polycondensation, which results elongation of single crystals to yield nanowires. Thus, the chemical changes (concentration changes) at each stage can be interpreted using relatively simple kinetic models by assuming our sol-gel colloidal solution is a quasi-homogeneous system.

The reaction rates can be expressed as the changes in concentrations of the reactants or products per unit time. The nanowire dimensions are a representation of the physical changes due to the chemical changes in their respective reactions. The growth of primary $Cu(OH)_2$ nanocrystals and their self-assembly to form nanocrystal chains during the hydrolysis and condensation step can be considered as a second order chemical reaction. We hypothesize that concentration of nanocrystals and self-assembled $Cu(OH)_2$ nanoarrays are proportional to their volume. For the polycondensation process in the second stage of stirring and aging intervals, the longitudinal growth of nanowires follows the zeroth order kinetic rate equation. Therefore, the potential crystal growth processes can be identified and tested assuming specific

rate limiting steps and testing the corresponding kinetic expressions with the data. The reaction orders and rates in the sol-gel reaction are calculated from suitable fitting parameters.

In this work, the time-dependent three key stages in sol-gel process are identified using higher magnification TEM images at each stirring time and aging time interval. We report, for the first time, the assessment of correlations between the observed growth rates and various fitted kinetic models. This assessment provides insight into the foundational mechanisms for various stages of the linear and lateral growth processes of metal oxide/metal hydroxide nanomaterials formation. Our hypothesis here is that the OA mechanism will drive the formation of $Cu(OH)_2$ nanowires, which follows second order kinetics during the hydrolysis period and zeroth order kinetics for the polycondensation and gel formation processes. The squared of correlation coefficient (R^2) of the fitted curves and the 95% levels of confidence for three replicate sets of trials are used to test and verify the proposed kinetic models.

4.2 Materials and Methodology

4.2.1 Chemicals and Materials

Copper(II)acetate monohydrate (98–102.0% powder) was purchased from Alfa Aesar. Sodium hydroxide (98% purity) was obtained from Sigma Aldrich. Unless otherwise specified, all chemicals were used as received.

4.2.2 Synthesis of colloidal $Cu(OH)_2$ NWs

To a 10 mL volumetric flask, copper(II)acetate monohydrate ($Cu(CH_3COO)_2.H_2O$, 40 mg, 0.2 mmol) was dissolved in 10 mL deionized (DI) water to make a 0.02 M Cu^{+2} homogeneous stock solution. Separately, to a 10 mL volumetric flask, sodium hydroxide (NaOH, 40 mg, 1.0 mmol) was dissolved in 10 mL of DI water to form a homogenous solution. The Cu^{+2} precursor solution (10 mL) taken from the freshly prepared stock solution was added to a 20 mL glass vial. While it was stirred gently at 500 rpm with a magnetic stirrer, the base, NaOH (10 mL) from the freshly prepared stock solution was added drop wise using a glass syringe over 5 minutes (rate

of 2 mL/min) at 25 °C in a water bath to yield a blue color suspension. The synthesis was run for 4 hours, stirring at 500 rpm using a Corning PC-620D magnetic stirrer in a water bath at 25 °C temperature. The suspension prepared in this manner was kept in the refrigerator at 5 °C and aged for 24 hours. During the aging process, the color of the reaction mixture changed from blueish green to green.

4.2.3 In-situ monitoring $Cu(OH)_2$ nanowire growth at different stirring and aging time intervals

To prepare TEM grid for in-situ monitoring of dimension analysis, collected suspensions at different stirring time intervals and aging time intervals (after adding NaOH, 5 min stirring, 10 min stirring, 15 min stirring, 30 min stirring, 45 min stirring, 1 h stirring, 1½ h stirring, 2 h stirring, 2½ h stirring 3 h stirring, 3½ h stirring 4 h stirring, 4½ h stirring, 5 h stirring, 5½ h stirring, 6 h stirring, 4 h aging, 8 h aging, 12 h aging, 16 h aging, 24 h aging) were micro centrifuged in 0.6 mL Eppendorf tubes for 1 min. Then, the precipitate was separated out, added ~0.5 mL of DI water to dilute the precipitate, and drop casted on the carbon coated copper TEM grid. The grids were air dried for 1 h under the hood.

4.2.4 Data collection and statistical analysis

Data collection:

Fifty individual nanowires were randomly selected in the entire TEM grid, which was scanned under higher magnification (100 kx, 160 kx) and their length and diameter were measured using ImageJ software at each stirring and aging time. To ensure the randomness, we used only these magnifications to avoid the bias for sizes of nanowires. The diameter measurements were taken only at 160 kx magnification to get higher magnification with better resolution. Three replicates (150 individual NWs) were performed in each stirring and aging time to perform the statistical analysis and validate the kinetic model.

Statistical analysis:

Diameter measurements: The average diameter of nanowire was calculated for each replicate (sample size is 50) and then median value of three replicates (150 NWs) were reported at each stirring and aging time. The 1σ (68.2%) standard deviation of experimental data was reported each stirring and aging time.

Length measurements: The standard deviation of experimental data is high with respect to their average length and the corresponding histogram appears to deviate from a normal distribution in each stirring and aging time. Since the sample distribution in the histogram shows positive skewness, we found out that a Gaussian distribution correlated well with the experimental data. Therefore, each length measurement analysis was based on a Gaussian fit of histograms, with three replicates (150 NWs) at different stirring time and aging time. The appropriate number of bins of the histogram for sample sizes of 150 observations, the number of bins varied between 7-12 bins to maximize R^2.[197] On the use of R^2 and 95% confidence bands are used to test and validate the proposed kinetic model. The square of the correlation coefficient (R^2) is a magnitude of the relationship's strength between experimental and predicted values of curve fitting. In our case, the Gaussian distribution curve fitting for the experimental length data (150 NWs) at all stirring and aging time intervals were maintained >0.90 R^2 values.

A sample uncertainty of plus and minus two standard deviations (±2 σ) quantifies the expected variability for 95% of the observed experimental mean or average of the normal distribution.[198] Therefore, to test and validate the proposed Sigmoidal Boltzmann kinetic model, we computed the R^2 values of the corresponding curve fitted to the experimental data. We report this data and the 2σ (95%) confidence bands in all figures. (Note that 1 standard deviation (1σ) = 68.2%, 2 standard deviation (2σ) = 95.4%, 3 standard deviation (3σ) = 99.7%[198]). The R^2 values and prediction bands were computed using Origin Pro 2021b software. For each experiment, Pearson's simple correlation (r) was estimated at a significance threshold,

(*P*), of 0.01 to test whether the agreement between the data and the proposed kinetic results was statistically significant.[199]

4.2.5 Characterization

In-situ monitoring of $Cu(OH)_2$ nanowire dimensions was performed using a transmission electron microscope ((TEM Carl Zeiss Libra 120) operated at 120 kV. Fifty individual nanowires were randomly selected in the entire grid, which was scanned under higher magnification (100 kx, 160 kx) and their length and diameter were measured using ImageJ software. The diameter measurements were taken only at 160 kx magnification. Time dependent crystal lattice spacings and crystallographic orientation were observed using the HR-TEM (JEOL 2100PLUS) with STEM/EDS capability.

4.3 Results and discussion

4.3.1 Real-time monitoring of $Cu(OH)_2$ crystal growth in a sol-gel system

In our recent study, we developed a facile sol–gel approach, which utilizes a base-catalyzed hydrolysis followed by condensation directed self-assembly and directed polymeric nanocrystal growth to prepare ultrathin $Cu(OH)_2$ nanowires, augmenting the previously reported OA based crystal growth process.[200] As depicted in Figure 23, the chemical processes in the previously developed sol-gel synthesis method show the self-assembly of $Cu(OH)_2$ nanocrystals guided by the OA crystal growth process to form ultrathin 1 D $Cu(OH)_2$ nanowires in water.

Figure 23: Synthetic Scheme For The Preparation of OA-based $Cu(OH)_2$ Nanowires

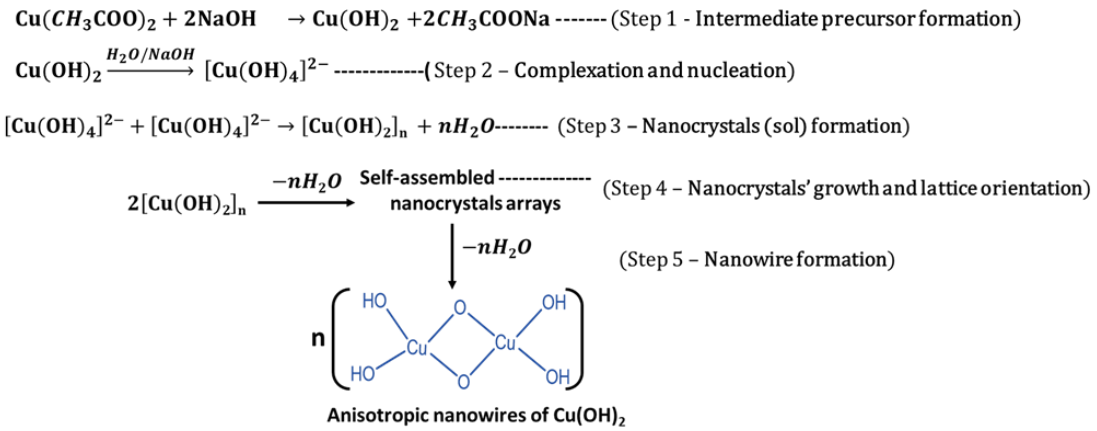

The reaction of copper acetate and NaOH formed the intermediate precursor, $Cu(OH)_2$, to initiate the sol-gel reaction via a double- displacement (salt metathesis) reaction (*step 1*). It is a rapid reaction and immediately begins the nucleation process in step 2 with base catalyzed hydrolysis to form tetrahydroxylated copper complex, $[Cu(OH)_4]^{2-}$. This hydrolysis is fast, facilitated by the charge density on the Cu^{+2} cation.[201] The tetrahydroxylated copper complex acts as nucleation sites and make $[Cu(OH)_2]_n$ nanocrystals (sol) during the hydrolysis and condensation process, as shown in step 3. Just after adding the base NaOH over 1 min, quasi-spherical, small, homogeneous colloidal primary nanocrystals form, with observed diameters of 1−3 nm as depicted in Figure 24(a). This colloidal formation is indicative of sol preparation in the sol-gel synthesis. The selected area electron diffraction (SAED) pattern shown in Figure 24(b), corresponds to the TEM image of primary nanocrystals and confirms their crystallinity. The lattice d-spacing measured from the HR-TEM images (Fig. 24 (c)) further confirms the formation of $Cu(OH)_2$, which has a lattice spacing of 2.3 Å along the a-axis.[202] Some nanocrystals exhibit different crystallographic orientations, and we observed a discernible neck initiation between two nanoparticles in some places, as shown in Figure 24 (c). Similarly, Wang et al. also reported the initiation of necks between oriented-attached PbSe nanocrystals using direct in-situ liquid cell TEM.[74]

Figure 24: (a) TEM Images of Sol Preparation After Adding NaOH Over 1 min To Copper Acetate Solution In The Sol-gel Synthesis And (b) Its SAED and (c) HR-TEM Image With Respective Lattice d- spacing For $Cu(OH)_2$.

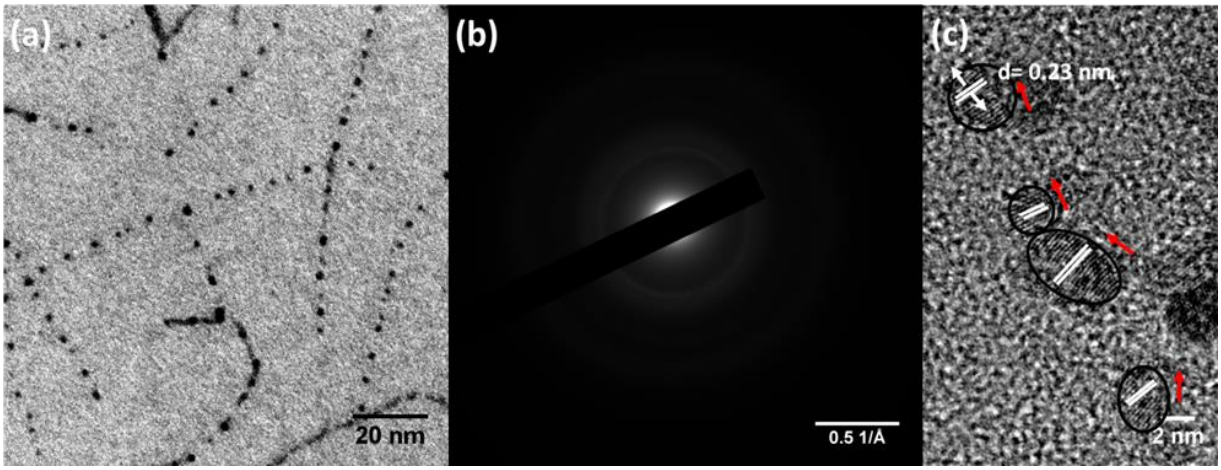

The next process, *step 4* is $[Cu(OH)_2]_n$ nanocrystals self-assemble to form anisotropic nanocrystal chains/arrays into specific crystallographic orientation via condensation. This condensation reaction could clearly be observed from the time-dependent TEM images taken just after adding NaOH over 5 min to 50 min of stirring time. During this time, we observe the self-assembly of nanocrystals with rough and irregular surfaces, as the nanocrystals roughly align in one direction, as shown in Figure 25. We reported a similar observation in our previous study.[200] To explore the driving force for the directed self-assembly of $Cu(OH)_2$ along one direction, HR-TEM imaging was performed. We can clearly see a discernible neck between nanocrystals and these nanocrystals are aligned into a specific crystallographic orientation in some places through rotation after 5 minutes stirring time, as revealed in Fig 26. Wang et al. also suggested that the growth of a neck occurs due to the diffusion of surface atoms on the lateral facets into the interface.[74] The clear, visible lattice fringes in most places enables us to calculate their d-spacing, i.e., ~2.3 Å and constant in all places, confirming the chemical structure of $Cu(OH)_2$. In figure 26, some lattice spacings are not visible due to the defocus caused by the three-dimensional variability of the nanowire. Although the coalescence of nanocrystals into a nanowire is incomplete, the alignment of nanocrystals through high energy

crystal facet rotation and interaction results in the reduction of total surface energy, which drives OA crystal growth.[185] Thus, this observation clearly indicates that the spontaneous self-organization of adjacent particles along a specific crystallographic direction of a nanocrystal's facet is the guiding principle for the size-controlled crystal-growth of nanowire formation.

Figure 25: Time Dependent In-situ TEM Images of $Cu(OH)_2$ Nanowires at Different Stirring Time Intervals (The addition of NaOH Over 5 Minutes Was Included To The Total Stirring Time)

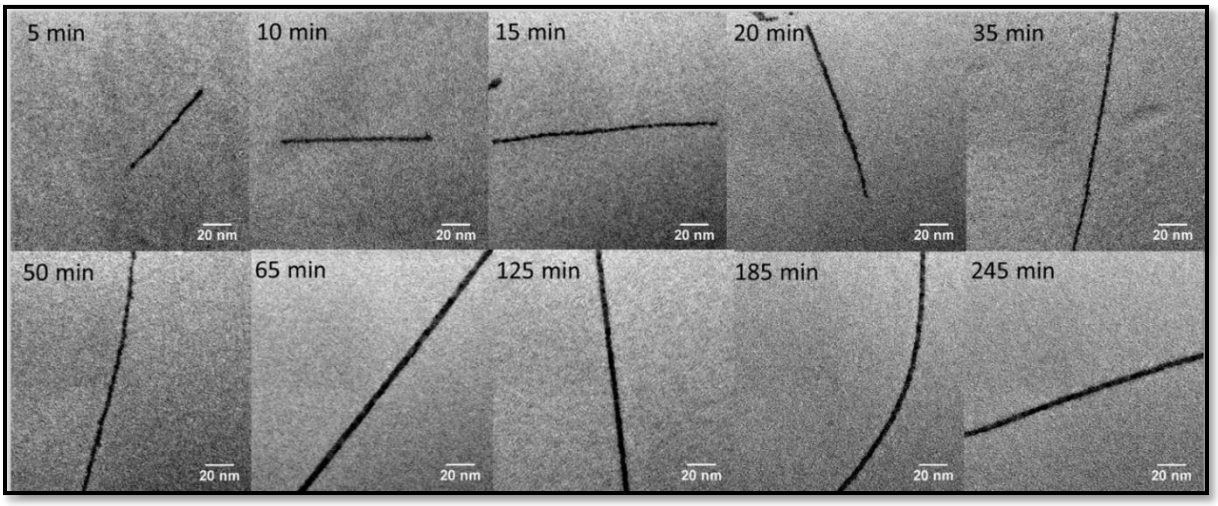

In *step 5*, the colloidal suspension transitions to nanocrystal growth and initial polycondensation to form a polymeric network of $Cu(OH)_2$ nanowires, which is a viscous, gelatinous material known as the "gel" in this synthesis. After adjacent nanocrystals coalesce over 1 h to 4 h stirring, these nanocrystals gradually evolved smoother surfaces, exhibiting nanowire structures, as depicted in Figure 25. A similar straightening process was observed by Zheng and co-workers. They reported the growth of large–aspect ratio, Pt_3Fe nanorods from the initially twisted nanoparticles observed using real-time liquid phase HRTEM/STEM.[203] They observed neck elimination between two particles and the straightening process to form nanorod structures. The complete reduction of interfaces between two particles, by eliminating crystal defects, possibly reduces the total surface energy in this system.

Figure 26: Time Dependent In-situ HR-TEM Images of $Cu(OH)_2$ Nanowires After Just Added NaOH Over 5 Min With Stirring. Arrowhead Marks Indicates The Neck Between Two Nanocrystals.

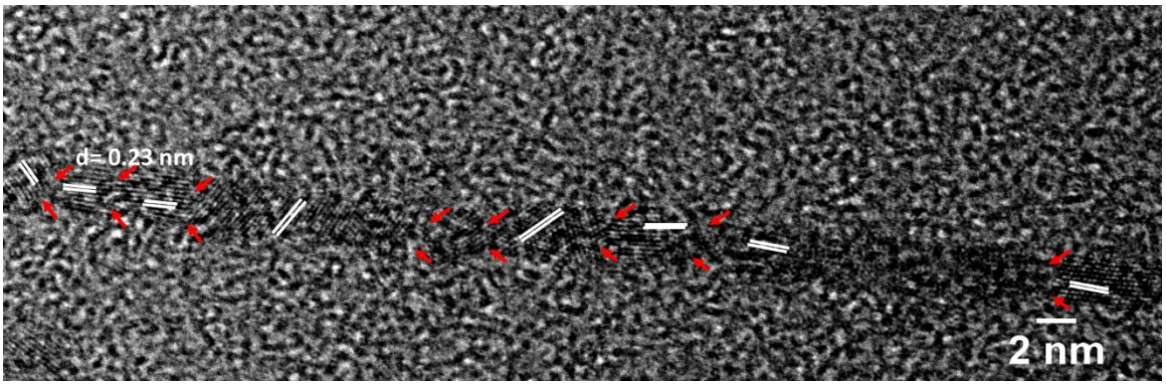

Aging studies at 5 ^{0}C reveal that the colloidal suspension undergoes further final stage of nanocrystal growth and complete polycondensation, as in *step 5*. It creates further oxygen bridging bonds between two copper atoms and networks in the system to yield stiffness and strengthened nanowires. These nanowires also have smoother surfaces, due to completion of the coalescence and smoothening processes, as shown in Fig 27.

Figure 27: Time Dependent In-situ TEM Images of $Cu(OH)_2$ Nanowires At Different Aging Time Intervals.

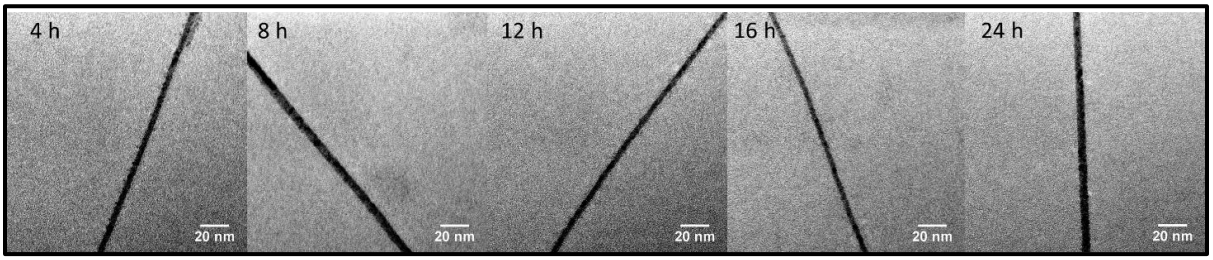

The plot of the absorbance maxima at λ_{max} of 660±1.6 nm at stirring and aging time intervals, as shown in Figure 28 exhibits variations in absorbance intensity with respect to stirring and aging times. It indicates changes in chemical reaction kinetics during each stage of the sol-gel process. The constant absorbance intensity corresponds to the sol formation and self-assembled nanochains. The concentration of $Cu(OH)_2$ nanocrystals and their self-assembly reaches to steady stage from 65 min to 200 min indicating that there is no further increase in the diameter of nanocrystals. It represents the first stage of polycondensation step that occurs

anisotropic lattice orientation, and longitudinal growth of nanowires along a specific crystallographic orientation. During aging, the steady absorbance intensities represent the second stage of polycondensation step that occur nanowire formation.

Figure 28: The UV- Visible Plot of Absorbance Maxima at 660 nm at (a) Stirring Time and (b) Aging Time Intervals (Experimental Error Bars Are Represented In Each Plot)

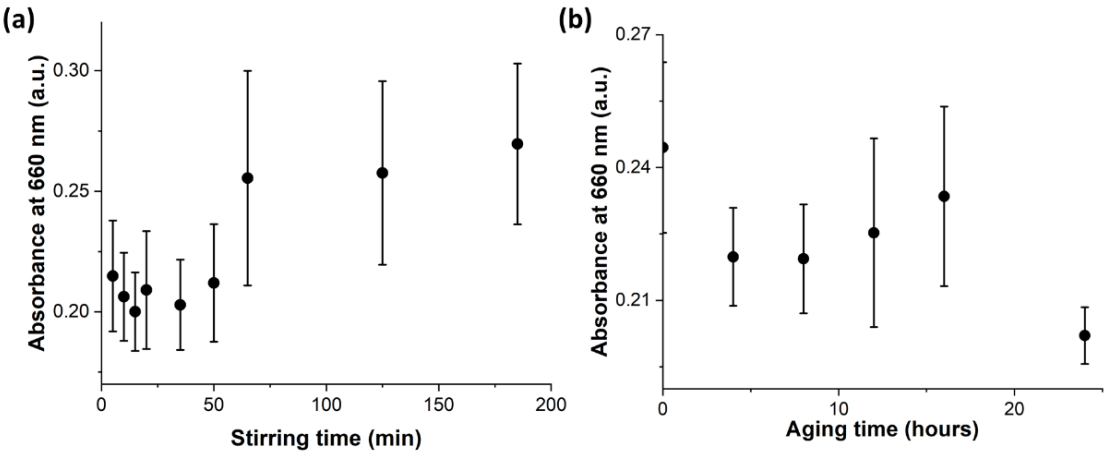

4.3.2 Development of a kinetic model for OA crystal growth of $Cu(OH)_2$

The time-dependent nanocrystal growth and nanowire formation were further explored by studying the mechanism and kinetics of size-controlled crystal growth. The dimensional analysis at different stirring (Table 8) and aging time (Table 9) intervals supports a new kinetic model for the evolution of the crystal growth elongation process. To validate this kinetic model, the statistical analyses were performed using three sets of replicates for each trial.

Table 8: The dimension analysis of $Cu(OH)_2$ nanowires at different stirring time intervals

Time (min)	Gauss fitted length (nm) ± SD (1σ)	Median diameter (nm) ± SD (1σ)	Volume (nm^3)
5	41.8± 1.7	2.7± 0.7	239.4
10	52.9± 4.5	2.8± 0.7	325.9

15	55.7± 3.6	3.1± 0.8	420.6
20	62.3± 2.6	3.2± 0.7	501.2
35	75.4± 2.2	3.1± 0.9	569.3
50	79.7± 2.6	3.4± 0.9	723.9
65	84.0± 8.9	3.4± 1.0	763.0
95	77.9± 5.1	3.9± 1.1	931.0
125	93.5± 5.4	3.6± 1.1	952.1
155	124.7± 5.9	3.8± 1.3	1414.8
185	94.2± 1.3	3.7± 1.1	1013.3
215	114.8± 5.7	4.1± 1.3	1516.3
245	114.5± 4.7	4.0± 1.3	1439.4
275	117.1± 6.5	4.5± 1.5	1863.1
305	107.9± 7.8	4.2± 1.3	1495.5
335	146.5± 5.0	4.3± 1.7	2128.3
365	148.6± 4.7	4.1± 1.4	1962.7

Table 9: The dimension analysis of $Cu(OH)_2$ nanowires at different aging time intervals.

Time (h)	Gauss fitted length (nm) ± SD (1σ)	Median diameter(nm) ± SD (1σ)	Volume (nm^3)
0	114.5± 4.7	4.0± 1.3	1439.4
4	115.2± 5.2	3.9± 1.0	1376.7
8	111.6± 13.9	3.9± 1.0	1333.7
10	120.7± 4.1	3.8± 1.3	1368.9
12	129.5± 4.1	4.3± 1.2	1881.4
14	135.0± 4.3	4.1± 1.2	1782.4

16	167.3± 4.6	4.1± 1.5	2209.7
24	160.8± 6.0	4.2± 1.3	2228.7

As a first order approximation, we assumed that each nanowire can be represented as a cylinder. The volume (V) of this cylindrical nanowire can be estimated through the geometric relation of a cylinder, as shown in equation 1, where, D and L are the observed nanowire diameter and length, respectively, of the nanowire.

$$\pi.\left(\frac{D}{2}\right)^2 L \text{.....(1)}$$

As reported in Table 8, just after adding the base over 5 minutes, the median diameter of colloidal nanowires is 2.7± 0.7 nm, which increases to 4.0± 1.3 nm after 4 hours of stirring. The median diameter was found to become constant at 4.1± 1.4 nm after 6 hours of stirring. The relatively high standard deviation of measured length data the reflects the somewhat skewed nature of the corresponding histogram. Since the sample distribution in the histogram shows positive skewness, we found out that a Gaussian distribution correlated well with the experimental data. Therefore, each length measurement analysis was based on a Gaussian fit of each histogram, with three replicates (sample size=150) at different stirring and aging time intervals (Appendix B and Appendix C). The appropriate number of bins of the histogram for sample sizes of 150 observations, the number of bins varied between 7-12 bins to maximize R^2.[197] These distributions correlated well with the experimental length data at all stirring and aging time intervals, with R^2 values >0.90 for each reaction time. The initial length of self-assembled nanocrystal arrays is 41.8± 1.7 nm after addition of the base. The crystal growth was observed along the long axes of nanocrystals, reaching up to 114.5± 4.7 nm at 4 hours stirring time. Furthermore, nanowire lengths increased to 160.8± 6.0 nm over a twenty-four-hour aging study at 5 ^{0}C.

We report a new model to describe nanowire crystal growth kinetics in this sol-gel reaction. For this study, the reaction rates can be expressed as changes in concentrations of the reactants (A) or products (B) per unit time. For example, the rate law for any order of reaction can be represented, as in equation 2.

Rate = $k[A]^x$; ……(2)

where, x is the order of the reaction with respect to A and k is the rate constant.[111]

In our case, we assume that the nanowire volume is proportional to the concentration of $Cu(OH)_2$ in the growing nanowire. According to the reaction equations in step 4, the condensation of $[Cu(OH)_2]_n$ nanocrystals to self-assembled nanocrystal arrays should reflect second order kinetics, with respect to $Cu(OH)_2$, with the form of

$$\frac{d[Cu(OH)2]}{dt} = k[Cu(OH)_2]^2 \text{……(3)}$$

We observed that the polycondensation and crystal growth of $Cu(OH)_2$ nanowires in *step 5* supports zeroth order kinetics. We tested various kinetic models with our condensation experimental data, e.g., for second order kinetics in the condensation phase, over stirring times of 5-50 min. The linear form of second order equation can be expressed as

$$^1/_{V_t} = -kt + {}^1/_{V_0} \text{……(4)}$$

where, k is the rate constant, V_t and V_0 are the nanowire volumes at stirring times t and t_0, respectively.

The linear form of zeroth order equation is

$$V_t = kt + V_0 \text{……(5)}$$

Assuming nanowire diameter is constant during the polycondensation, the zeroth order equation for polycondensation and crystal growth is

$$L_t - L_0 = 4kt/\pi D^2 \text{……(6)}$$

where, L_t is the length of nanowire at time t, L_0 is the length of nanowire at time=0, k is the rate constant, and D is the nanowire diameter.

Here, the observed R^2 values for linear fittings are relatively low at 0.739 and 0.904, for second order and zeroth order of reactions, respectively (Figure 29 (a) and (b)). Also, the plotted experimental data appears to be curvilinear. The lack of fit of the models to the data is larger and the R^2 values are lower than expected to support these simple kinetic models.

Figure 29: Linear Fitting of The Experimental Data For (a) Second Order Reaction (0-50 Min Stirring) and (b) Zeroth Order Reaction (50-365 Min Stirring) To Test The Developed Kinetic Model.

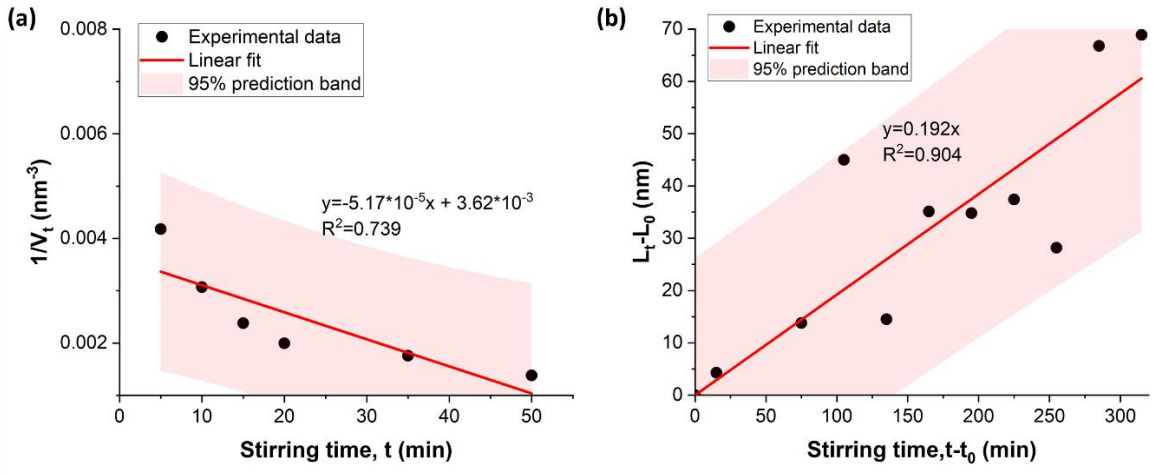

Let's consider other types of growth behaviors found in Nature. For example, cooperative growth processes, such as peptide aggregation and protein fibrillation by monomeric polymerization, exhibit sigmoidal behavior.[204–206] Schreck and Yuan also report that their proposed kinetic model for the self-aggregation of proteins, which considers average fibril lengths as a function of time, shows sigmoidal-like behavior.[207] This sigmoidal growth curve is characterized by (1) an initial lag or nucleation phase, (2) an elongation or growth phase, and (3) a stationary or saturation phase.[206] Any nucleation-controlled aggregation model exhibit these three characteristics, i.e., an initial lag phase of molecular organization and then a linear phase of rapid growth, which is followed by a saturation phase at the end of the growth period. Therefore, we modified our second order and zeroth order models to incorporate this type of sigmoidal Boltzmann behavior, which has the form of $y=A_2+\frac{(A_1-A_2)}{1+\exp\left(\frac{t-t_0}{dt}\right)}$ .....(7)

where, A_1 is final value of growth parameter, A_2 is initial value of growth parameter , t_0 is center of linear growth phase , dt = time constant, 1/ dt is the maximum growth rate.[208]

The proposed Sigmoidal Boltzmann second order kinetic equation for the self-assembled nanoarrays formation as presented in Scheme 4.3.1, stated in eq 8.

$$1/V_t = 1/V_f + \{\frac{(1/V_0 - 1/V_f)}{1+e^{(t-t_0)R}}\} \quad \text{.....(8)}$$

where, V_t is the volume at time t, V_0 is the initial volume of individual nanowire, V_f is the final volume of individual nanowire, t is time, t_0 is the lag time (fitting parameter of linear growth phase) and R is the growth rate (time^{-1})

The proposed Sigmoidal Boltzmann zeroth order kinetic equation for the polymeric network $Cu(OH)_2$ nanowire formation from self-assembled nano arrays, as presented in Figure 23, stated in eq 11.

$$(Cu(OH)_2\ NWs)_t = (Cu(OH)_2\ NWs)_f + \frac{(self-assembled\ nanoarrays)_0 - (Cu(OH)_2\ NWs)_f)}{1+e^{(t-t_0)R}} \text{ ..(9)}$$

$$(\pi.(\frac{D}{2})^2.L)_t = (\pi.(\frac{D}{2})^2.L)_f + \frac{(\pi.(\frac{D}{2})^2.L)_0 - (\pi.(\frac{D}{2})^2.L)_f)}{1+e^{(t-t_0)R}} \text{.....(10)}$$

$$L_t = L_f + \{\frac{L_0 - L_f}{1+e^{(t-t_0)R}} \text{.....(11)}$$

where, L_t is the length at time t, L_0 is the initial length of individual nanowire, L_f is the final length of individual nanowire, t is time, t_0 is the lag time (fitting parameter of linear growth phase) and R is the growth rate (time^{-1}).

The Sigmoidal Boltzmann curve fitting of the experimental data for both second and zeroth order kinetics for the stirring time studies are shown in Figure 30. The derived Boltzmann fitting expression was applied to the experimental data of initial and final lengths of $Cu(OH)_2$ NWs. Here, the values of R^2 of for these Boltzmann fittings increased to 0.936 and 0.944 for second order and zeroth order of reactions, respectively. We observed a maximum growth rate (R) for this second order reaction to be 0.243 min^{-1} and for the zeroth order reaction to be 0.019 min^{-1}, respectively. In each case, the condensation and polycondensation steps explains the

presence of a lag phase of $Cu(OH)_2$ molecules organization until the system achieves critical aggregation concentration, then rapid nanowire growth proceeds until most of the $Cu(OH)_2$ nanocrystals in the system are consumed. Finally, nanowire growth reaches a saturation phase when no $Cu(OH)_2$ is available to further react.

During the early phase, the second order condensation rates are systematically higher under basic conditions compared to other orders of reaction due to the large amount of unbounded –OH groups in the reaction.[201] In our sol-gel system, we can see that condensation second order rate are higher than the polycondensation zeroth order rate during stirring (Figure 30). All observed data were positioned within the 95% confidence band (±2σ) of the Boltzmann fit. The higher R^2 value and level of confidence compared to previous linear models gives support for this proposed kinetic model. Furthermore, we attempted first, second and zeroth order models separately to fit our experimental data for the whole stirring period, considering there is only one chemical process occurs during the stirring time. However, the R^2 value for each phase appears to be lower than the R^2 value for the composite three-phase process. Therefore, these data further support our hypothesis that the assembly reaction proceeds via three consecutive chemical processes during the stirring time studies in the sol-gel synthesis, i.e., via hydrolysis, condensation, and polymerization.

The diameter evolution of $Cu(OH)_2$ nanowires was studied at different stirring time intervals. A linear fit of median nanowire diameters does not exactly match with experimental data, as it shows a slight growth during the initial stirring time (Figure 31). Therefore, we proceeded with a more in-depth analysis using HR-TEM to gain a deeper understanding of the crystal growth mechanism.

Figure 30: Sigmoidal Boltzmann Curve Fitting of The Experimental Data During Stirring For (a) Second Order Reaction (5-50 Min Stirring) and (b) Zeroth Order Reaction (50-365 Min Stirring) To Test the Developed Sigmoidal Boltzmann Kinetic Model.

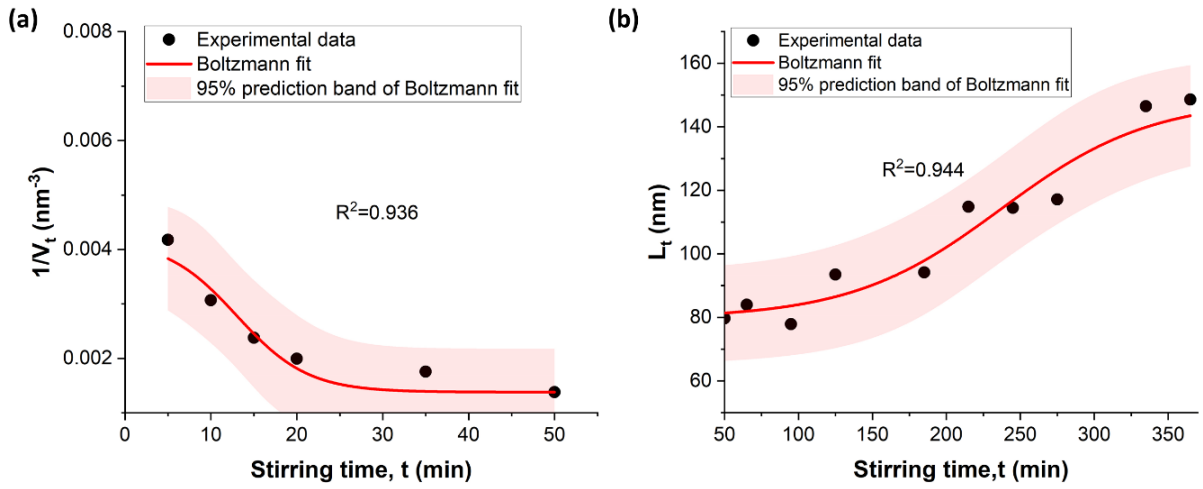

Figure 31: The Linear Fitting of Median Diameter for Stirring Time Intervals (The Error Bars Represent Actual Experimental Standard Deviation (1σ)

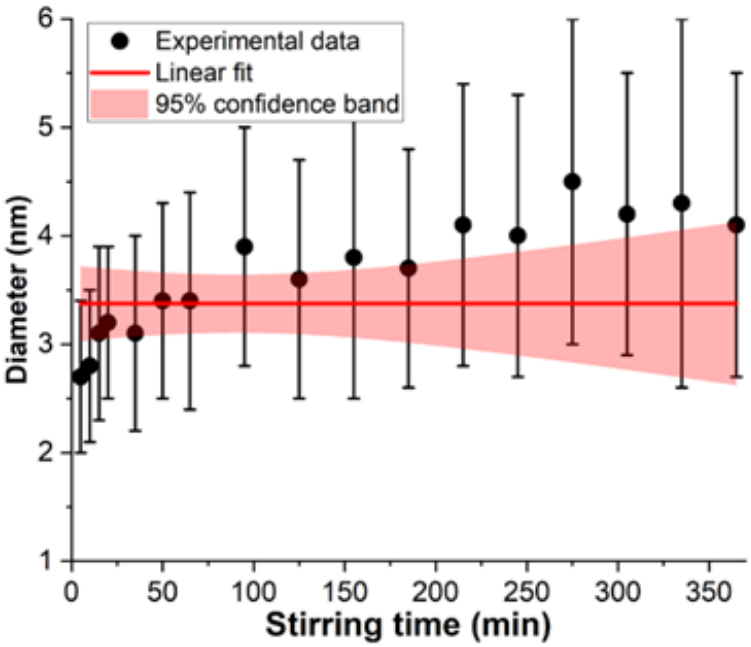

Our previous study reported the preferential growth of $Cu(OH)_2$ NWs along the [020] direction using time-dependent powder XRD analysis.[200] Figure 32 (a) shows HR-TEM images of $Cu(OH)_2$ NW growth, with several truncated nanocrystals attached together via a common crystallographic direction, after stirring for 1 hr. This observation provides strong support for nanowire growth by an OA mechanism along the [020] direction. The grain edges are clearly visible and demonstrate the coalescence and growth of nanocrystals by an OA mechanism. Moreover, it is noteworthy that most of these particles are similar in size and produce nanowires of relatively constant diameter. The perfect crystal alignment after 4 hours by sharing the same crystallographic orientation with a single crystalline Fast Fourier Transform (FFT) pattern (inset in Figure 32 (c)), demonstrates the OA crystal growth mechanism. confirming We also observe a few incorporated defects, such as twins and stacking faults after stirring for 4 hours. Such incorporated defects are characteristic features of growth processes that follow an OA mechanism.[114,209] For example, defects may form by misoriented attachment in the necking regions. After 24 h aging, the HR-TEM image further supports the perfect alignment of self-assembled nanocrystals that make the nanowire through the OA mechanism and the FFT image (in-set) confirms the single crystal uniformity (Figure 33 (a)). The elemental distribution map obtained from the STEM/EDS analysis in Figure 33 (b-d) further confirms the presence of Cu and O in the synthesized nanowires after 24 h aging and their purity. The HR- TEM lattice spacing analysis was performed using FFT method, computed with ImageJ software.[210] The lattice d-spacing measured from the HR-TEM images in every synthesis time has the cell constant of 2.3 Å along the a-axis, evidencing $Cu(OH)_2$. Therefore, these results support our hypothesis on the OA mechanism based sol-gel thesis to fabricate ultrathin $Cu(OH)_2$ NWs.

Figure 32: HR-TEM Images that Show Crystallographic Orientations of Nanocrystals During the Synthesis of $Cu(OH)_2$ NWs at 1 Hour and 4 Hours Stirring Time Intervals.

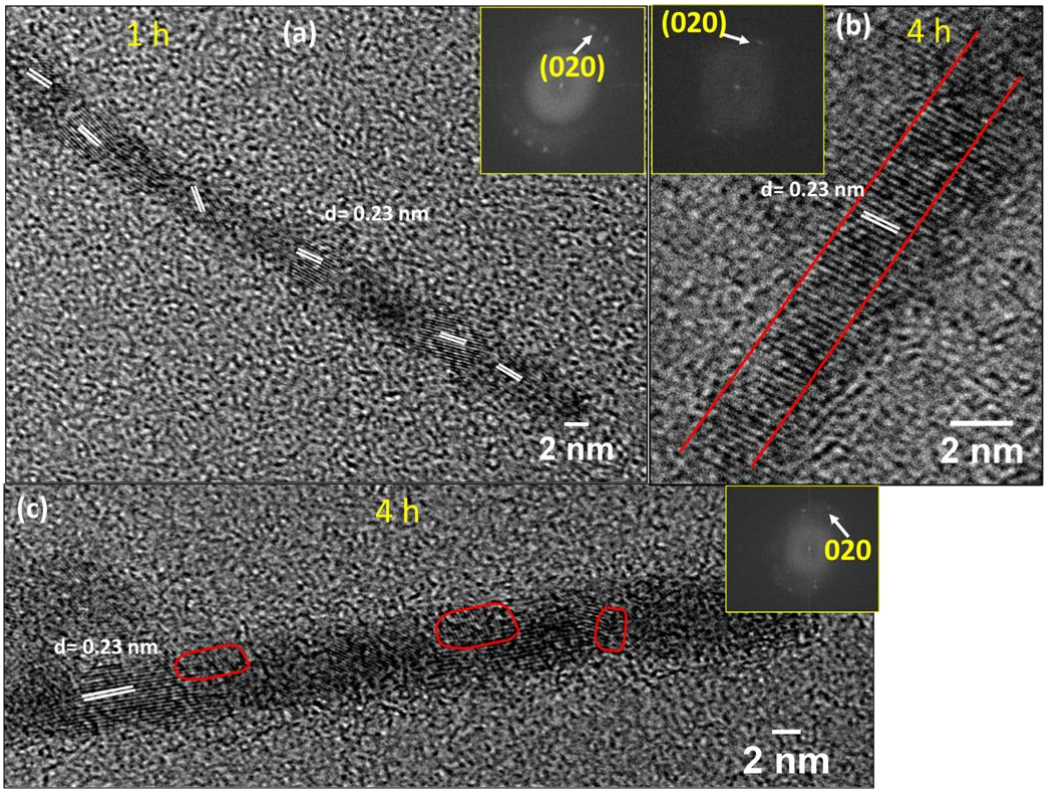

Figure 33:(a) HR-TEM Images at 24 h Aging and Their STEM/EDS Analysis Images of (b) HAADF-STEM With Its Elemental Mapping (c) Cu and (d) O

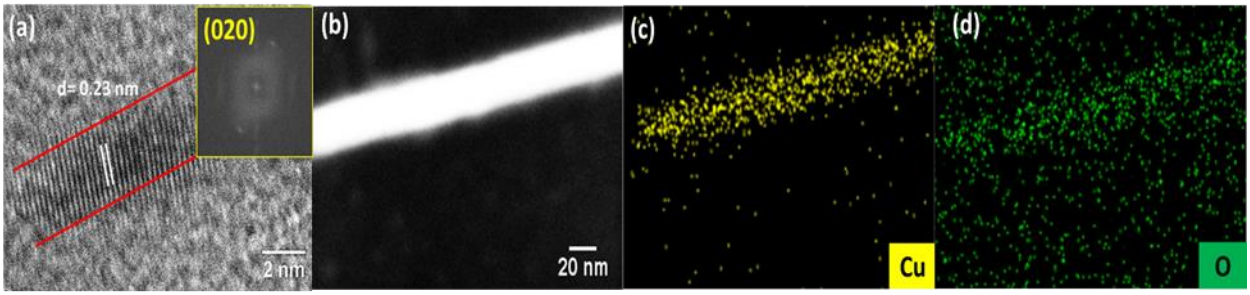

Figure 34: (a) Sigmoidal Boltzmann Curve Fitting of The Experimental Data for Zeroth Order Reaction (b) Linear Fitting of Diameter Analysis During Aging Time Intervals (Error Bars Represent the Experimental Uncertainty (1σ)).

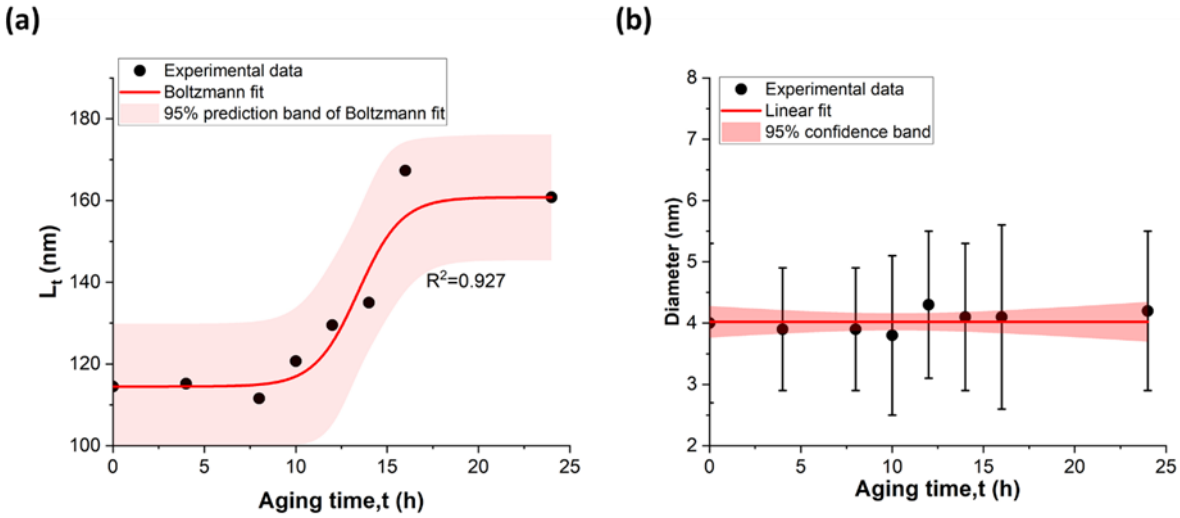

Similarly, we tested the Sigmoidal Boltzmann curve fitting of the experimental data during aging time intervals using zeroth order kinetics for the polycondensation and the crystal growth of nanowires as our experimental data follows Sigmoidal behavior (Fig 34 (a)). We observed an R^2 of 0.927 for fitting the data to a Sigmoidal Boltzmann fitting. Additionally, we observed that all the experimental values stayed within the 95% confidence band. Therefore, this result supports zeroth order kinetics during aging. From this model, we estimated a maximum growth rate, R, of 0.842 h^{-1}. Based on the data shown in Figure 34 (b), we found that the median $Cu(OH)_2$ nanowire diameter was 4.02 nm and independent of aging time. This diameter evolution analysis further supports an OA growth mechanism. In each kinetic models, we tested the models with Pearson's simple correlation (r) and *P* value, which reflects the degree of alignment between the model and observed data, in table 10. The actual *p* values are $p < 0.01$ and confirms this Sigmoidal association are statistically significant.

Table 10: Pearson's correlation (r) and P-values of each Sigmoidal kinetic models

Time interval	Sigmoidal order of reaction kinetics	R^2	r	*P*	Significancy of results
Stirring (5-50 min)	Second order	0.936	0.967	0.001616	Significant
Stirring (50-365 min)	Zeroth order	0.944	0.971	0.000010	Significant
Aging (0-24 h)	Zeroth order	0.927	0.963	0.000123	Significant

4.4 Conclusion

In conclusion, this in-situ TEM study provides a foundational understanding of the crystal growth mechanisms and chemical kinetics of the $Cu(OH)_2$ nanowire growth from crystalline nanoparticles. This work provides new insights into anisotropic nanowire formation in a sol-gel system. Specifically, we observed nanocrystal formation, via in situ monitoring of $Cu(OH)_2$ sols, and their self-assembly into colloidal pre-nanowires aggregates. Subsequently, we observed the directed self-assembly and OA crystal growth via condensation followed by poly condensation to form a nanowire using an HR-TEM. We propose a novel sigmoidal growth model for the oriented attachment of anisotropic nanowires using HR-TEM. We estimated sigmoidal second order and zero order reaction rates for condensation and polycondensation processes, respectively, during stirring, sigmoidal second order rate of 0.243 min^{-1} and sigmoidal zero order rate of 0.019 min^{-1}, respectively. During the aging process, we estimated the sigmoidal zeroth order growth rate for the polycondensation and crystal growth rate of $Cu(OH)_2$ nanowires to be 0.842 h^{-1}.

Thus, our work achieves a significant milestone in the application of real time imaging of anisotropic nanowires to the testing of various rate limiting growth processes and mechanistic

options. It demonstrates this imaging approach's value in developing foundational understanding and guiding principles for the fabrication of deep 1D nanostructures.

Table 11: Summary of kinetic growth rates of sigmoidal growth model for the oriented attachment of anisotropic nanowires in the sol-gel process.

Time interval	Stage of sol-gel process	Sigmoidal order of reaction kinetics	Maximum growth rate	R^2
Stirring (5-50 min)	Condensation	Second order	0.243 min^{-1}	0.936
Stirring (50-365 min)	Polycondensation	Zeroth order	0.019 min^{-1}	0.944
Aging (0-24 h)	Polycondensation & crystal growth	Zeroth order	0.842 h^{-1}	0.927

For this study, we applied this real-time near atomic scale imaging to elucidate the growth mechanism and to develop a robust process for fabricating sub 4 nm nanowires using OA attachment without using any surfactants. This work demonstrates that an 'enhanced' OA informed approach offers an effective strategy to fabricate size-controlled anisotropic nanowires. We believe that extensions of this work could further expand into the understanding of crystal growth processes for other self-assembled 1D nanomaterials and novel supramolecular structures, such as certain classes of designed bionanomaterials.

CHAPTER V: CRYSTAL GROWTH OF ULTRATHIN COPPER HYDROXIDE NANOWIRES IN THE PRESENCE OF PHOSPHOLIPID

5.1 Introduction

Advances in nanotechnology have attracted extensive research interest in the size and shape-controlled growth of one-dimensional (1D) nanostructured materials. These anisotropic nanostructures demonstrate considerable advantages over isotropic structures improved charge transport properties and electrochemical properties, enhanced catalytic properties, optical properties and electrical properties for different applications.[211] Oriented attachment (OA) is the main crystal growth mechanism that explains the self-assembly of nanocrystals to form anisotropic structures at the nanoscale by sharing a common crystallographic orientation.[6,7] Up to date, the OA process was demonstrated for the formation of various 1D nanostructures including nanorods, nanowires, and nanotubes. OA-based crystal growth is governed by thermodynamics as the result of reduction in the surface energy of crystal facets.[6,12] Therefore, surfactant adhesion or adsorption onto specific crystal facets, with different binding affinities to the growing nanocrystals, modulates the total crystal surface energy of the nanostrucure.[139] Hence, the crystal surface energy and the growth rate drive the nanocrystal shape evolution and the final shape of the nanostructure.

In the past few decades, extensive investigations have been devoted to the development of metal/metal oxide nanocrystals with tailored architectures utilizing different surfactants. For example, strong adsorption of alkylamines onto [001] crystal plane induces the formation of disk shaped Co nanocrystals.[212] Carboxylic acids adsorption to the anatase TiO_2 nanocrystals along the {001} crystal facet has resulted in the formation of TiO_2 nanorods by reducing the growth rate along [001] direction.[140,213] Another example demonstrated that cetyltrimethylammonium tosylate (CTAT) exhibits an affinity to adsorb on the [011] crystal plane to form long wormlike micelles in water that leads to the formation of silver nanorods.[214] To synthesize Cu_2O

nanooctahedrons, polyvinylpyrrolidone (PVP) was used since it preferentially adsorbs on the [111] crystal facet.[215] Halder and Ravishankar reported the formation of OA-based gold nanowires by adhesion of oleylamine along {111} facets.[216] The selective adsorption of cetyltrimethylammonium bromide (CTAB) on the {100} crystal planes resulted in the penta-twinned gold nanorods formation.[217] These examples provide general key strategies in shape control by selecting different surfactants in the synthesis of different nanocrystals. Surfactants also can influence the crystal growth kinetics by strongly interacting with nanocrystal seeds. Recently, more attention has opened towards the controlled synthesis of metal hydroxide/oxide nanowires with the rational utilization of bioinspired materials.

The adsorption of soluble organic biomolecules on crystal faces can alter the surface energy in OA-based crystal growth.[14] Specific biomolecules such as proteins, proteolipids, phospholipids, collagen, and carbohydrates can control the nucleation, growth, the size, and the orientation of crystals.[15] A phospholipid is a type of lipid and the most important component in cell membranes. The bilayer membrane is a self-assembled nanostructure that maintains the integrity of the membrane. Phospholipids can be anionic, cationic, zwitterionic or non-ionic depending on their overall molecular charge. These amphiphiles are composed of hydrophilic and hydrophobic segments. The driving force for their self-assembly is the hydrophobic-hydrophilic repulsion between the polar head group and fatty acid tail. The polar head of amphiphiles enables them to coordinate with metals at the metal hydroxide interface in a relatively strong manner. The metal coordination strength strongly depends on the functional groups of the amphiphile's polar head, their number, shape, and position of the functional group in the molecule.[145] By varying the type and the concentration of surfactants provide tools for tuning the crystallographic orientation and the crystal growth rate of anisotropic nanostructures While a few studies report about nanocrystal shape evolution based on the use of surfactants, even less is understood about how the facile controlled synthesis of ultrathin metal hydroxide nanowires impacts the evolution of nanocrystal growth.

This work describes the fabrication of ultrathin $Cu(OH)_2$ nanowires, using the sol-gel method followed by directed self-assembly of nanocrystals, in the presence of two different concentrations of zwitterionic phospholipid, DPPC, as a surfactant in an $H_2O/CHCl_3$ solvent system. Our hypothesis is that the surface energy induced adsorption of phospholipids on to copper hydroxide nanocrystals will focus high crystal surface energy at the ends and induce directional growth at the oil/water interface for the fabrication of ultrathin nanowires. The crystal planes of synthesized nanowires were identified by X-Ray Diffraction (XRD) analysis and their crystal lattice spacing was measured using high-resolution transmission electron microscopy (HR-TEM) imaging. The elemental composition and oxidation states of synthesized nanowires was investigated using X-ray photoelectron spectroscopy (XPS) analysis. Phospholipid assisted ultrathin copper hydroxide nanowires provide an example of how to evolve anisotropic nanostructures by fine tuning the crystal facet energy of nanocrystal seeds.

5.2 Materials and Methodology

5.2.1 Chemicals and materials

Copper(Ⅱ)acetate monohydrate (98-102.0 % powder) was purchased from Alfa Aesar. Sodium hydroxide (98 % purity) and chloroform (99.8 %, ACS spectrophotometric grade) were purchased from Sigma Aldrich, while DPPC (1,2-dipalmitoyl-sn-glycero-3-phosphocholine, >99%) was purchased from Avanti Polar Lipids. They used as received without any purification otherwise specified.

5.2.2 Synthesis of ultrathin copper hydroxide nanowires in the presence of DPPC

To a 10 mL volumetric flask, copper(Ⅱ)acetate monohydrate ($Cu(CH_3COO)_2.H_2O$, 40 mg, 0.2 mmol) was dissolved in 10 mL deionized (DI) water to make 0.02 M Cu^{+2} homogeneous stock solution. Separately, to a 10 mL volumetric flask, sodium hydroxide (NaOH, 40 mg, 1.0 mmol) was dissolved in 10 mL of DI water to form a homogenous solution. To a 20 mL glass vial, 100 µL of $CHCl_3$ and 150 µL of DPPC (10 mg/mL) was added and mixed well. Then Cu^{+2}

precursor solution (10 mL) taken from the freshly prepared stock solution was added into the vial containing DPPC. The ratio of Cu^{2+} moles to DPPC moles is 100:1. While it was stirring gently in a magnetic stirrer, the base, NaOH (10 mL) from the freshly prepared stock solution was added drop wise using a glass syringe over 5 minutes (rate of 2 mL/min) at 25 °C in a water bath to yield a blueish milky color suspension. The synthesis was done for 4 hours stirring at 500 rpm using a Corning PC-620D magnetic stirrer in a water bath at 25 °C temperature. The blueish green suspension with the milky layer in the bottom was yielded. Then it was kept for 24 h aging at 5 ^{0}C and the reaction mixture was changed from blueish green to green color.

The green suspension was centrifuged and washed with DI water three times to remove salts and leftover starting materials. Without air drying, the wet green solid was resuspended in DI water (~1 mL) and transferred to a glass vial. Then immediately the suspension was drop-casted on Si wafer and performed the morphology and composition analysis (TEM, SEM and XPS). Another replicate was synthesized and after 24 h aging and washed, the suspension was freeze dried and prepared the powder sample to calculate the yield. XRD and FTIR were performed for powder sample.

In a separate reaction, to have a different concentration of phospholipid, Cu^{2+} moles to DPPC moles ratio 59:1, 250 µL of DPPC was added into the Cu^{+2} precursor solution (10 mL) and followed the same procedure.

5.2.3 Investigation of UV-vis spectroscopy analysis during the synthesis

UV-Vis analysis was performed at different stirring and 24 h aging time intervals. The solution (1 mL) was collected from the vial at each time interval to conduct UV-vis analysis and after the analysis, the solution was discarded. Therefore, the total volume was changed during the study. The peak fitting was performed to do the quantitative analysis of maximum peak wavelength for the distorted UV-vis spectrum, having higher absorbance in shorter wavelengths as a function of time. The peak wavelength was reported after fitting each spectrum with a

single Gaussian peak with the background subtraction using a polynomial curve.[179] The regression coefficients of all the fitted curves were maintained at ≥0.999 precision.

5.2.4 Characterization

The morphology was observed using transmission electron microscopy (TEM Carl Zeiss Libra 120) at 120 keV and crystal lattice spacings were observed HR-TEM (JEOL 2100PLUS) with STEM/EDS capability at 200 keV. The surface morphology was performed using scanning electron microscopy (Zeiss Auriga FIB/FESEM) for as prepared samples on the Si substrate without sputter coating for any additional conductive layer on it. The UV-Vis analysis of samples was determined using ultraviolet-visible spectroscopy (Varian Cary 6000i). The atomic concentrations and binding energies of all the elements present in the nanowires were obtained from X-ray photoelectron spectroscopy (XPS-Escalab Xi+ Thermo Scientific electron spectrometer). The powder XRD analysis was conducted using Cu Ka radiation (40 kV, 40 mA, k=1.54 °A) with a speed of 90 s on the X-ray diffractometer (XRD, Agilent technologies Gemini).

Figure 35: Experimental Setup for the Synthesis of $Cu(OH)_2$-DPPC Nanowires

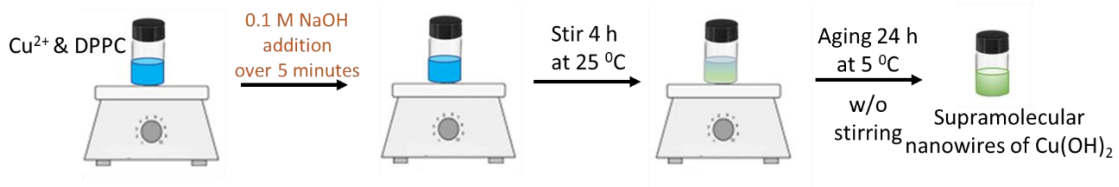

5.3 Results and discussion

The sol–gel process is a wet-chemical technique widely employed for the fabrication of size and shape-controlled nanostructures. Starting from a metal salt as the precursor and catalyzed by base or acid forms an integrated network (or gel) of either discrete particles or network polymers. This method became popular to make different inorganic oxides, organic-inorganic hybrids, and composites. It provides various advantages such as high yield, better reproducibility, low operation temperature and low-cost method of highly stoichiometric and homogeneous products. The nonhydrolytic sol–gel process pathways follow when organic solvents as reagents in the medium and the oxygen atoms are originated from the organic O-

donor in the products.[99,103–105] Our group recently reported a facile sol-gel approach to prepare shape-controlled ZnO nanostructures, which combines a solvent polarity driven self-assembly and solvothermal crystal growth process.[22] During that study, we demonstrated that the solvent acts as a surfactant and adsorbs onto the surfaces of the growing crystallites to control their nanocrystal growth and final morphology. Moreover, our previous study presented a facile sol-gel route with directed colloidal nanocrystal self-assembly to prepare ultrathin $Cu(OH)_2$/CuO nanowires in a surfactant free aqueous solution.[200] It suggested that the OA crystal growth mechanism is responsible for the $Cu(OH)_2$ nanowire formation. This suggestion is based on our time-dependent studies of nanocrystal formation, growth, and nanowire self-assembly by imaging under HR-TEM. The time-dependent powder XRD traces demonstrated OA directed crystal growth along the [001] crystal facet in the nanowires. Specially, this work focuses on providing a demonstration of surfactant assisted controlled crystal growth of $Cu(OH)_2$ nanowires. We used the similar reaction route, parameters and conditions that we used to fabricate ultrathin $Cu(OH)_2$ nanowires in water to study their morphology and crystal growth direction. The sol-gel route to prepare ultrathin $Cu(OH)_2$ nanowires in the presence of DPPC is summarized in Figure 36.

Figure 36: The Sol-gel Route for the Formation of $Cu(OH)_2$-DPPC Nanowires

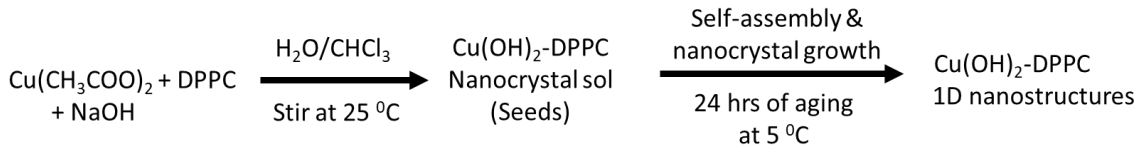

Figure 37: UV-visible Absorption Spectra taken at Different Time Intervals During the Reaction (In Water) at 25 ^{0}C and It Is Constant During the Reaction.

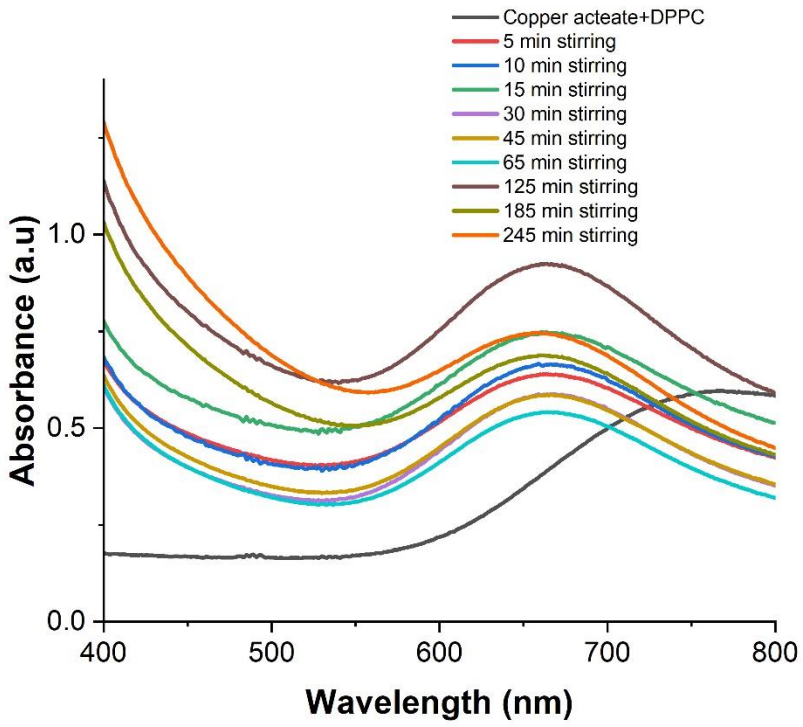

The time dependent UV-vis spectra shows that the absorption band shifted to a shorter wavelength region at ~669 nm from the wavelength of initial copper acetate and DPPC solution at 769 nm (Figure 37). This observed absorption maximum shift from 769 nm to 669 nm supports the evidence for changes in the electronic structure after adding NaOH at all stirring time intervals. We performed peak fittings to test whether there is an actual peak shift at different stirring times for the synthesis of $Cu(OH)_2$ NWs in the presence of phospholipids. The quantitative analysis of peak wavelength was determined by single Gauss peak fitting of the distorted UV-vis spectra at different time intervals, as shown in Appendix D. The average wavelength 669.5±1.6 nm, as shown in Table 12. The maximum absorbance of $Cu(OH)_2$ nanowire is 660 nm[178]. Therefore, with the presence of DPPC, it represents an ~10 nm blue shift compared to the absorption maximum for $Cu(OH)_2$ nanowires. This absorption band shift

supports the evidence of changes of electronic structure of $Cu(OH)_2$ nanowires after adsorption of DPPC.

Table 12: Summary of Gauss peak fitting analysis at different time intervals.

Sample	Peak wavelength after Gauss fitting (nm)	SD (±nm)
5 min stirring	669.0	0.1
10 min stirring	669.0	0.1
15 min stirring	667.7	0.1
30 min stirring	669.1	0.1
45 min stirring	669.0	0.1
65 min stirring	668.9	0.1
125 min stirring	667.1	0.1
185 min stirring	672.0	0.1
245 min stirring	671.3	0.1
24 hours aging	671.4	0.1
Average	669.5	
SD	1.6	

After aging the system for 24 hours, TEM images in Figure 38 (a) show the fully grown nanowires that exhibit stacks of hair like wires. SEM images in Figure 38 (b) also demonstrate the stacks of very thin hair like continuous wires after post-synthesis aging for 24 h. The individual nanowire with smooth surfaces, which have an average diameter of 5.6 nm [±2σ] is shown in Figure 38 (c). Therefore, both TEM and SEM images confirm the formation of nanowires. The HR-TEM lattice spacing analysis was performed using a Fast Fourier Transform (FFT) method, computed with ImageJ software.[210] The lattice d-spacing measured from the HR-TEM images (Figure 38 (d)) has a cell constant of 2.3 Å along the a-axis. Further, it confirms an

oriented attachment crystal growth mechanism, showing uniform distribution of lattice orientation along the nanowire. The respective FFT pattern (in Figure 38 (f)), confirming single crystalline nanowires grown along [*020*] crystal facet (along the lattice cell axis-*b*).

Figure 38: TEM Images of $Cu(OH)_2$–DPPC Nanowires After 24 h Aging and Washed (a) Stacks of Nanowires (b) SEM Images of $Cu(OH)_2$–DPPC Nanowires After 24 h Aging, Washed and Without Sputter Coating (c) Individual Nanowire at 120 kV (d) HR-TEM Images at 200 kV Representation of Lattice Spacing and Perfect Crystallographic Orientation of $Cu(OH)_2$–DPPC Nanowires (e) Its Respective SAED Pattern and (f) Its Respective FFT.

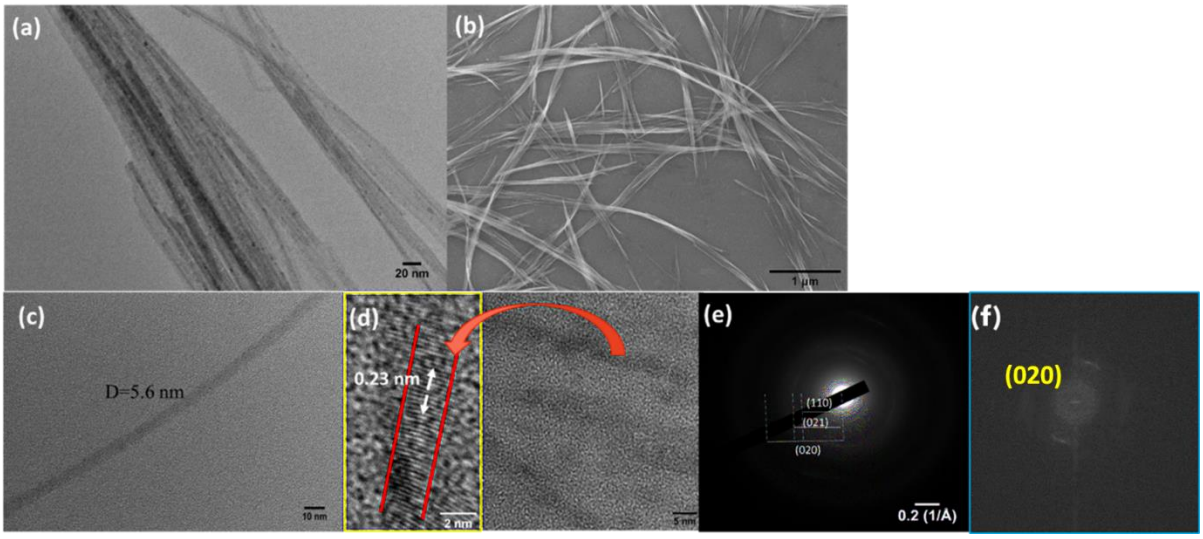

To investigate the elemental composition and oxidation states of synthesized nanowires, X-ray photoelectron spectroscopy (XPS) analysis was conducted, as shown in Figure 39. The XPS survey spectra confirm the presence of Cu, P, C, N, and O and the atomic ratio of Cu^{2+} to DPPC (Table 13) is found to be 1: 1, indexing the $Cu(OH)_2$–DPPC empirical formula to $C_{40}H_{82}NO_{10}PCu$. Two major peaks in the binding energy spectrum of Cu *2p* were observed at 935.6 eV and 955.6 eV. These peaks were attributed to the binding energy states for Cu $2p_{1/2}$ and Cu $2p_{3/2}$ of Cu–O bonds in $Cu(OH)_2$.[181] The presence of two less intense satellite peaks along with two major peaks indicate the presence of Cu(II) ions.[181] Furthermore, we observed

two peaks for P *2p* at 130.2 eV and 133.1 eV, supporting the presence of a phosphate group associated with the nanowires. There is a well-resolved major peak for O *1s* at 531 eV, with a larger FWHM at 4.12 eV, which supports the oxygen chemical bonding state of O^{2-} for the hydroxide.[218] The weak peak for O *1s* at 529.5 eV suggests the existence of oxygen ions, which has lower electron density than O^{2-} in metal hydroxides. This may be the characteristic weak peak of O^{-} anions from the phosphate group of DPPC that adsorbed onto the nanowire. Therefore, the elemental compositional and oxidation states analysis conducted using XPS confirms the presence of Cu, P, C, N and their oxidation states supports the adsorption of DPPC in $Cu(OH)_2$ nanowires.

Figure 39: (a) XPS Survey of $Cu(OH)_2$-DPPC NWs and Binding Energy Spectra of (b) Cu *2p* (c) O *1s* (d) N *1s* (e) C *1s* (f) P *2p*

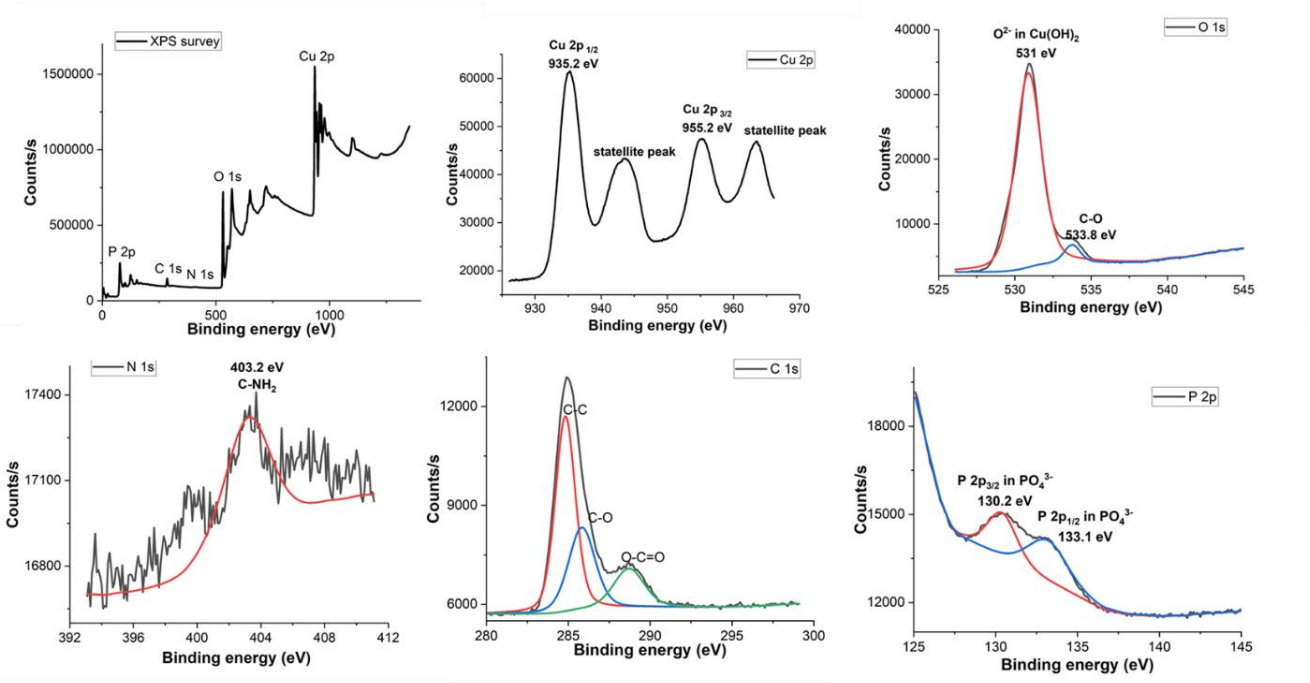

Table 13: Summary of FWHM and weight ratio of elements in the synthesized $Cu(OH)_2$-DPPC nanowires

Sample	Peak	Position BE (eV) ±0.10 eV	FWHM(eV) ±0.20 eV	Atomic Con. (%)
$Cu(OH)_2$-DPPC NWs	Cu $2p_{1/2}$; Cu $2p_{3/2}$	935.6, 955.6	5.70	29.90
	O 1s	531, 529.5	4.12	57.15
	P $2p_{1/2}$; P $2p_{3/2}$	133.1, 130.2	3.50	0.67
	C 1s	284.8, 287.6	4.57	12.08
	N 1s	Weak	1.93	0.19

Figure 40: FTIR Analysis of (a) $Cu(OH)_2$–DPPC Nanowires After 24 h Aging, Washed, and Freeze-dried Powder (b) $Cu(OH)_2$ Nanowires

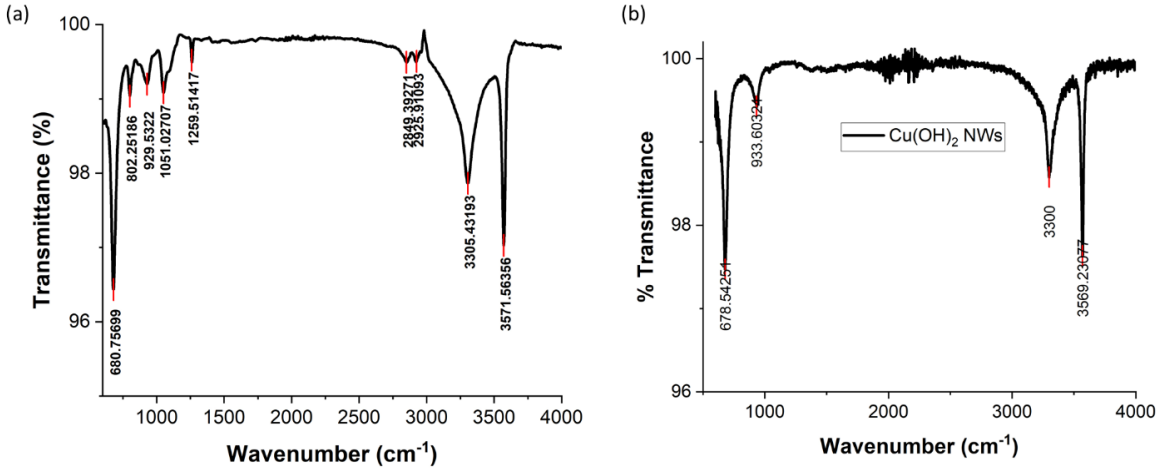

As depicted in Figure 40(a), the FTIR spectrum of synthesized nanowires showed the presence of characteristic peaks of PO_2 stretching at 1051 and 1259 cm^{-1}, P-O stretching at 802 cm^{-1} and CH_2 stretching at 2849 and 2926 cm^{-1}. [219] The two characteristic peaks at 3300 and 3569 cm^{-1} coming from the $Cu(OH)_2$ nanowires synthesized in DI water suggests the stretching modes of hydroxyl groups in the $Cu(OH)_2$ (Figure 40(b)) and they can observe in the synthesized nanowires in the presence of DPPC phospholipids.[220] The sharp peaks at 678-680 cm^{-1} suggest

the presence of Cu-O stretching from both nanowires, which is typically present in the fingerprint region.[220]

Figure 41: The XRD Pattern of (a) Synthesized $Cu(OH)_2$–DPPC Nanowires (b) $Cu(OH)_2$ Nanowires.

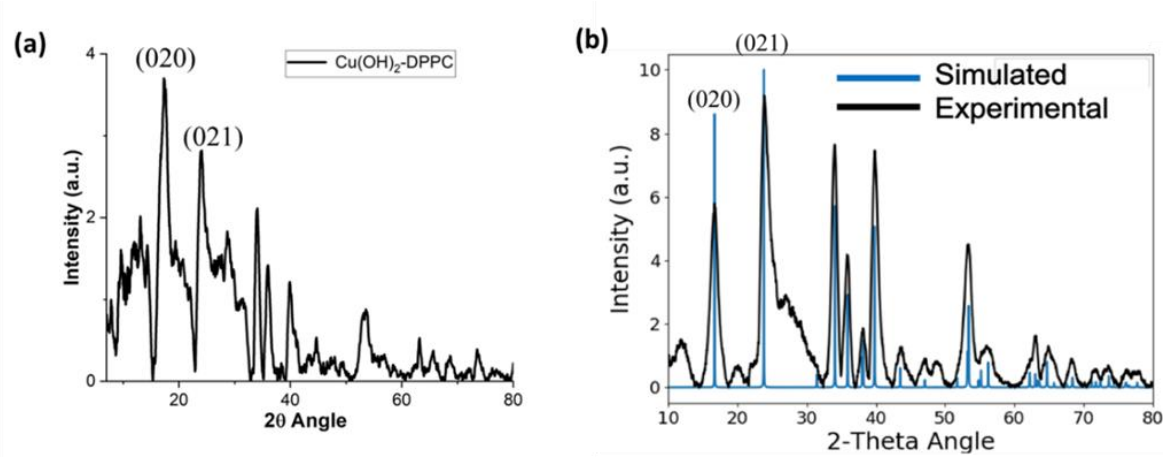

Our previous study reported that the XRD powder diffraction pattern of $Cu(OH)_2$ nanowires exhibits six main diffraction planes; [020], [021], [002], [130], [150], and [152], indexing the orthorhombic crystal unit cell, which exactly matches with the previous literature.[180,200] The XRD pattern of $Cu(OH)_2$-DPPC NWs (Figure 41 (a)) have a similar set of six main diffraction peaks. We can observe that there is a change in the prominent growth of crystallographic direction at [020] plane, while decreasing the intensities of all other crystal planes. We have identified the growth of the [020] crystal diffraction plane along with the [021] plane in $Cu(OH)_2$ nanowires from the time dependent XRD traces, as shown in Figure 41 (b). Wang and Nancollas report that the phosphate adsorption crystal plane is [010].[221] This may be the reason for switching the intensities of crystal planes between [020] and [021] of the synthesized nanowires in the presence of phospholipids. Therefore, by introducing DPPC into the synthesis of $Cu(OH)_2$ nanowires, which acts as a surfactant, we suggest that the adsorption of phosphate group into high energy crystal facet of $Cu(OH)_2$ nanowires can change the crystal growth rate of the nanowires.

5.4 Conclusion

In summary, this study demonstrated tunable nanocrystal facets with the surfactant assisted crystal growth to make ultrathin $Cu(OH)_2$-DPPC nanowires. The time dependent UV-vis spectra supports that the synthesized $Cu(OH)_2$ nanowires in the presence of DPPC has red shifted its absorption band to 669.5 nm from 660 nm in the DI water. It evidences the changes of the electronic structure of $Cu(OH)_2$ after adsorption of DPPC. The HR-TEM, and respective SAED and FFT analysis confirms the OA directed crystal growth process for the formation of single crystalline nanowires with uniform distribution of lattice orientation along [*020*] crystal facet (the lattice cell axis-*b*). The XPS compositional analysis of synthesized nanowires have shown that the atomic ratio of Cu^{2+} to DPPC is 1: 1 and their oxidation states support the adsorption of DPPC on $Cu(OH)_2$ nanowires. The FTIR spectrum also supports the presence of characteristic peaks for PO_2 stretching, Cu-O stretching, and for hydroxyl groups in the $Cu(OH)_2$ synthesized nanowires. The experimental powder XRD pattern exhibits six main diffraction planes for $Cu(OH)_2$ nanowires and the crystal growth of synthesized nanowires in the presence of phospholipids along [*020*] plane is prominent. Thus, our OA-directed crystal growth approach provides a surfactant assisted controlled crystal growth process for fabricating ultrathin 1D nanowires. This work offers a promising and novel strategy to control the crystal plane and growth rate of metal hydroxide/oxide nanowires by selecting a suitable surfactant.

CHAPTER VI: CONCLUSIONS AND FUTURE DIRECTIONS

6.1 Conclusions

The overall goal of this dissertation was to investigate the nanocrystal growth mechanism and kinetics to prepare ultrathin 1D-metal hydroxide/oxide nanowires, and in-situ self-assembly with phospholipids that offers the size and shape-controlled synthesis of 1D nanostructures. This work offers following significant contributions to different concepts.

- Demonstrated a novel, facile and greener sol-gel synthesis method to fabricate ultrathin $Cu(OH)_2$/CuO nanowires.
- Provided new insights on guiding principles for the fabrication of sub 4 nm nanowires without using any surfactants in a sol-gel system.
- Introduced a novel kinetic model for $Cu(OH)_2$ nanowires that considers the directed growth of the length.
- Extended the prediction of the crystal growth processes for the crystal facet selective fabrication of novel supramolecular structures of $Cu(OH)_2$-decorated phospholipids.

There is enough literature about fabrication of different types of metal hydroxide/oxide nanowires using different synthesis approaches. However, the fabrication of ultrathin crystalline metal hydroxide/oxide nanowires that can be scalable and reproducible using chemical routes are rarely reported. Consequently, this work focused on the scalable and environmentally benign fabrication of ultrathin $Cu(OH)_2$/CuO nanowires via a low temperature sol-gel synthesis method. While this study demonstrates feasibility, more work is needed to enable the robust controlled synthesis of ultrathin copper hydroxide/oxide nanowires. Until recently, the guiding principles that control nanowire size and shape were poorly understood and rarely explored. Therefore, this study demonstrates the governing crystal growth mechanism to produce anisotropic nanowires and calculates the kinetic rates by introducing new kinetic models to for 1D copper hydroxide/oxide nanowire syntheses in a sol-gel system.

Aim 1: We successfully fabricated $Cu(OH)_2$ nanowires using a versatile wet chemical synthesis method. We also investigated the oriented attachment crystal growth mechanism of $Cu(OH)_2$ nanocrystals for the formation of nanowires. Here, we introduced a facile environmentally benign base-catalyzed sol-gel approach, augmenting oriented attachment crystal growth directed self-assembly of colloidal nanocrystals to make ultrathin $Cu(OH)_2$ and CuO nanowires. After the 24 hrs of aging of synthesis, the fully grown ultrathin $Cu(OH)_2$ nanowires show an average length of 172.2±98.3 nm and a diameter of 4.2± 1.3 nm. The high standard deviation of length implies the wide length distribution of nanowires. We identified the oriented attachment mechanism that governs the crystal growth of $Cu(OH)_2$ nanowires, using time-dependent studies of TEM. The time dependent powder XRD traces and SAED patterns of TEM showed the crystallinity of produced nanowires. Also, XRD analysis revealed the packing pattern of $Cu(OH)_2$ nanowires, which were indexed to an orthorhombic crystal unit cell. The powder XRD traces analysis confirms crystal growth of OA directed $Cu(OH)_2$ nanowires progress along the [020] and [021] crystal facets. Our XPS analysis established the composition and oxidation states of Cu and O. It confirms the formation of highly pure $Cu(OH)_2$ nanowires. Upon annealing, ultrathin $Cu(OH)_2$ nanowires transformed into CuO nanowires. The length of CuO nanowires is ten times higher than the length of $Cu(OH)_2$ nanowires. XRD analysis of CuO nanowires revealed the crystal growth along the crystal facets of the [002] and [111] reflection planes. Overall, we demonstrated an OA-directed crystal growth approach to make ultrathin 1D $Cu(OH)_2$ nanowires. Therefore, this works offers significant guidance to prepare size-and shape-controlled copper hydroxide/oxide 1D nanostructures with tailored properties, which may be extended to other metal hydroxide/oxide 1D nanostructures.

Further, time dependent HR-TEM imaging demonstrates nanocrystal seeds and nanowires formation. We successfully observed the nanocrystal seeds, with diameters of 1−3 nm, after adding the base. This imaging captured the progression of the nanocrystal seed self-assembly process. It also showed neck formation between nanocrystals that aligns with the

specific crystallographic order and the gradual formation of smoother surfaces to make nanowires.

We introduced new Sigmoidal Boltzmann kinetic models to explain this sol-gel reaction process, such as hydrolysis and sol formation, condensation, polycondensation, and gel formation. We report the growth rates for corresponding chemical processes in this dissertation. This work provides a significant contribution to our fundamental understanding of the mechanism and growth kinetics for size and shape controlled anisotropic 1 D crystalline nanowires.

Aim 2: We investigated the crystal growth mechanism of $Cu(OH)_2$ nanowires in the presence of different concentrations of phospholipids. This work demonstrated the fabrication of supramolecular $Cu(OH)_2$ nanowire structures decorated with phospholipids. Time dependent UV-vis spectra showed the absorption band of synthesized nanowires red shifted to 669.5±1.6 nm compared to $Cu(OH)_2$ nanowires at 662.4±1.6 nm. It demonstrates changes in the electronic structure after adsorption of DPPC phospholipid. Furthermore, the OA crystal growth process shows perfect crystallographic orientation of the nanowire. The compositional and oxidation states were analyzed using XPS for the produced nanowires. It confirms the presence of Cu, P, C, N and their oxidation states, supporting the formation of $Cu(OH)_2$-DPPC nanowires. The experimental powder XRD pattern exhibits six main diffraction planes of the $Cu(OH)_2$ nanowires. However, the intensities of two main crystal plane directions have switched and the prominent crystal planes is [020] plane after the adsorption of DPPC on to $Cu(OH)_2$ nanowires. We successfully demonstrated crystal-facet tunable nanocrystal seeds with surfactant assisted controlled crystal growth to make ultrathin $Cu(OH)_2$-DPPC nanowires. This work provides a promising guide to control the crystal plane and growth rate of copper hydroxide/oxide nanowires by selecting a suitable biomolecules, surfactants, or polymers.

6.2 Recommendations for Future Research

This dissertation has uncovered interesting phenomena that can lead to miniature devices such as electronic, optical, and electrochemical devices, fulfilling the growing demand of controlled fabrication of functional nanomaterials. This chapter emphasizes some of the future directions and opportunities that can pursue for controlled nanowire fabrication with tailored properties for different applications.

6.2.1. Fabrication of ultrathin $Cu(OH)_2$ nanowires and supramolecular structures of $Cu(OH)_2$ -DPPC nanowires

In our work, we fabricated only one type of binary transition metal hydroxide/oxide nanowire and demonstrated the in situ self-assembly with one phospholipid. Future work suggests studies of other types of binary transition metal oxides nanowires and their interactions with other biomolecules/surfactants/polymers to make size and shape-controlled nanowires. Not only different binary transition metal oxides, but also different types of tertiary and quaternary transition metal hydroxides/oxides can be explored to synthesize ultrathin nanowires. Also, we can optimize our sol-gel synthetic route to make nanowires with specific length ranges in a reduced time. Furthermore, we can investigate other facile wet chemical routes to fabricate these nanowires. These nanowires can be tested for use in a diverse range of industrial applications. In our 2020 published journal article in Nanoscale advances, we reported the electrical and optical properties of synthesized $Cu(OH)_2$ and CuO nanowires. This work showed the suitability for potential optoelectronic devices. Further, it could be expanded to include the analysis of electrochemical properties, and other possible properties for different applications.

6.2.2 Investigation of the crystal growth mechanism and kinetics of ultrathin $Cu(OH)_2$ and $Cu(OH)_2$ -DPPC nanowires

We investigated the nanowire crystal growth mechanism using time-dependent TEM/HR-TEM. Future directions could include studies of the crystal defects of $Cu(OH)_2$ nanowires during the synthesis. We used only one specific temperature in our sol-gel route

during stirring and aging time intervals. Varying reaction temperatures may reveal additional kinetics and morphological changes in the nanostructures. These promising avenues, when combined with different biomolecules, can yield further changes in morphology, crystal growth rates, and crystal plane attachment preferences. Furthermore, it can be expanded to better understand how their electrical, catalytic, optical, or suitable properties vary with different biomolecule concentrations. This line of research will enable new capabilities and options to fabricate different nanostructure morphologies, with desired properties and with the aid of selective surfactants.

REFERENCES

(1) Cademartiri, L.; Ozin, G. A. Ultrathin Nanowires-A Materials Chemistry Perspective. *Adv. Mater.* **2009**, *21* (9), 1013–1020.

(2) Zhang, H.; Penn, R. L.; Lin, Z.; Cölfen, H. Nanocrystal Growth via Oriented Attachment. *CrystEngComm* **2014**, *16* (8), 1407.

(3) Kirchner, H. O. K. Coarsening of Grain-Boundary Precipitates. *Metall. Trans.* **1971**, *2* (10), 2861–2864.

(4) Xue, X.; Penn, R. L.; Leite, E. R.; Huang, F.; Lin, Z. Crystal Growth by Oriented Attachment: Kinetic Models and Control Factors. *CrystEngComm* **2014**, *16* (8), 1419.

(5) Zhang, J.; Huang, F.; Lin, Z. Progress of Nanocrystalline Growth Kinetics Based on Oriented Attachment. *Nanoscale* **2010**, *2* (1), 18–34.

(6) Penn, R. L. Imperfect Oriented Attachment: Dislocation Generation in Defect-Free Nanocrystals. *Science* **1998**, *281* (5379), 969–971.

(7) Penn, R. L.; Banfield, J. F. Oriented Attachment and Growth, Twinning, Polytypism, and Formation of Metastable Phases; Insights from Nanocrystalline TiO_2. *Am. Mineral.* **1998**, *83* (9–10), 1077–1082.

(8) Gao, X.; Zhu, H.; Pan, G.; Ye, S.; Lan, Y.; Wu, F.; Song, D. Preparation and Electrochemical Characterization of Anatase Nanorods for Lithium-Inserting Electrode Material. *J. Phys. Chem. B* **2004**, *108* (9), 2868–2872.

(9) Mirzaei, A.; Lee, J.-H.; Majhi, S. M.; Weber, M.; Bechelany, M.; Kim, H. W.; Kim, S. S. Resistive Gas Sensors Based on Metal-Oxide Nanowires. *J. Appl. Phys.* **2019**, *126* (24), 241102.

(10) Zhang, G.; Xiao, X.; Li, B.; Gu, P.; Xue, H.; Pang, H. Transition Metal Oxides with One-Dimensional/One-Dimensional-Analogue Nanostructures for Advanced Supercapacitors. *J. Mater. Chem. A* **2017**, *5* (18), 8155–8186.

(11) Li, Y.; Yang, X.-Y.; Feng, Y.; Yuan, Z.-Y.; Su, B.-L. One-Dimensional Metal Oxide Nanotubes, Nanowires, Nanoribbons, and Nanorods: Synthesis, Characterizations, Properties and Applications. *Crit. Rev. Solid State Mater. Sci.* **2012**, *37* (1), 1–74.

(12) Ning, J.; Men, K.; Xiao, G.; Zou, B.; Wang, L.; Dai, Q.; Liu, B.; Zou, G. Synthesis of Narrow Band Gap SnTe Nanocrystals: Nanoparticles and Single Crystal Nanowires via Oriented Attachment. *CrystEngComm* **2010**, *12* (12), 4275.

(13) Dasgupta, N. P.; Sun, J.; Liu, C.; Brittman, S.; Andrews, S. C.; Lim, J.; Gao, H.; Yan, R.; Yang, P. 25th Anniversary Article: Semiconductor Nanowires - Synthesis, Characterization, and Applications. *Adv. Mater.* **2014**, *26* (14), 2137–2184.

(14) Limo, M. J.; Sola-Rabada, A.; Boix, E.; Thota, V.; Westcott, Z. C.; Puddu, V.; Perry, C. C. Interactions between Metal Oxides and Biomolecules: From Fundamental Understanding to Applications. *Chem. Rev.* **2018**, *118* (22), 11118–11193.

(15) Veis, A. MATERIALS SCIENCE: Enhanced: A Window on Biomineralization. *Science* **2005**, *307* (5714), 1419–1420.

(16) Song, R.-Q.; Cölfen, H. Additive Controlled Crystallization. *CrystEngComm* **2011**, *13* (5), 1249.

(17) Lenglet, M. Iono-Covalent Character of the Metal–Oxygen Bonds in Oxides: A Comparison of Experimental and Theoretical Data. *Act. Passive Electron. Compon.* **2004**, *27* (1), 1–60.

(18) Guo, T.; Yao, M.-S.; Lin, Y.-H.; Nan, C.-W. A Comprehensive Review on Synthesis Methods for Transition-Metal Oxide Nanostructures. *CrystEngComm* **2015**, *17* (19), 3551–3585.

(19) Goodwin, D. W. *Transition Metal Oxides. Crystal Chemistry, Phase Transition and Related Aspects. NBS 49* by C. N. R. Rao and G. V. Subba Rao. *Acta Crystallogr. B* **1975**, *31* (12), 2943–2943.

(20) Yang, Q.; Lu, Z.; Liu, J.; Lei, X.; Chang, Z.; Luo, L.; Sun, X. Metal Oxide and Hydroxide Nanoarrays: Hydrothermal Synthesis and Applications as Supercapacitors and Nanocatalysts. *Prog. Nat. Sci. Mater. Int.* **2013**, *23* (4), 351–366.

(21) Pacholski, C.; Kornowski, A.; Weller, H. Self-assembly of ZnO: From Nanodots to Nanorods. *Angew. Chem. Int. Ed.* **2002**, *41* (7), 1188–1191.

(22) Davis, K.; Yarbrough, R.; Froeschle, M.; White, J.; Rathnayake, H. Band Gap Engineered Zinc Oxide Nanostructures *via* a Sol–Gel Synthesis of Solvent Driven Shape-Controlled Crystal Growth. *RSC Adv.* **2019**, *9* (26), 14638–14648.

(23) Chaurasiya, N.; Kumar, U.; Sikarwar, S.; Yadav, B. C.; Yadawa, P. K. Synthesis of TiO2 Nanorods Using Wet Chemical Method and Their Photovoltaic and Humidity Sensing Applications. *Sens. Int.* **2021**, *2*, 100095.

(24) Jayachandran, M.; Rose, A.; Maiyalagan, T.; Poongodi, N.; Vijayakumar, T. Effect of Various Aqueous Electrolytes on the Electrochemical Performance of α-MnO2 Nanorods as Electrode Materials for Supercapacitor Application. *Electrochimica Acta* **2021**, *366*, 137412.

(25) Liang, H.; Meng, F.; Lamb, B. K.; Ding, Q.; Li, L.; Wang, Z.; Jin, S. Solution Growth of Screw Dislocation Driven α-GaOOH Nanorod Arrays and Their Conversion to Porous $ZnGa_2O_4$ Nanotubes. *Chem. Mater.* **2017**, *29* (17), 7278–7287.

(26) Murphy, C. J.; Jana, N. R. Controlling the Aspect Ratio of Inorganic Nanorods and Nanowires. *Adv. Mater.* **2002**, *14* (1), 80–82.

(27) Decher, G. Fuzzy Nanoassemblies: Toward Layered Polymeric Multicomposites. *science* **1997**, *277* (5330), 1232–1237.

(28) Pascual, J. I.; Mendez, J.; Gomez-Herrero, J.; Baro, A. M.; Garcia, N.; Landman, U.; Luedtke, W. D.; Bogachek, E. N.; Cheng, H.-P. Properties of Metallic Nanowires: From Conductance Quantization to Localization. *Science* **1995**, *267* (5205), 1793–1795.

(29) Arutyunov, K. Yu. Negative Magnetoresistance of Ultra-Narrow Superconducting Nanowires in the Resistive State. *Phys. C Supercond.* **2008**, *468* (4), 272–275.

(30) Dresselhaus, M. S.; Chen, G.; Tang, M. Y.; Yang, R. G.; Lee, H.; Wang, D. Z.; Ren, Z. F.; Fleurial, J.-P.; Gogna, P. New Directions for Low-Dimensional Thermoelectric Materials. *Adv. Mater.* **2007**, *19* (8), 1043–1053.

(31) Teng, X.; Han, W.-Q.; Ku, W.; Hücker, M. Synthesis of Ultrathin Palladium and Platinum Nanowires and a Study of Their Magnetic Properties. *Angew. Chem.* **2008**, *120* (11), 2085–2088.

(32) Marcus, P.; Mansfeld, F. B. *Analytical Methods in Corrosion Science and Engineering*; CRC press, 2005.

(33) Hou, H.; Zhu, Y.; Hu, Q. 3D Cu(OH) $_2$ Hierarchical Frameworks: Self-Assembly, Growth, and Application for the Removal of TSNAs. *J. Nanomater.* **2013**, *2013*, 1–8.

(34) Du, G. H.; Van Tendeloo, G. Cu(OH)2 Nanowires, CuO Nanowires and CuO Nanobelts. *Chem. Phys. Lett.* **2004**, *393* (1–3), 64–69.

(35) Huang, L. S.; Yang, S. G.; Li, T.; Gu, B. X.; Du, Y. W.; Lu, Y. N.; Shi, S. Z. Preparation of Large-Scale Cupric Oxide Nanowires by Thermal Evaporation Method. *J. Cryst. Growth* **2004**, *260* (1–2), 130–135.

(36) Mageshwari, K.; Sathyamoorthy, R. Flower-Shaped CuO Nanostructures: Synthesis, Characterization and Antimicrobial Activity. *J. Mater. Sci. Technol.* **2013**, *29* (10), 909–914.

(37) Dubal, D. P.; Gund, G. S.; Lokhande, C. D.; Holze, R. CuO Cauliflowers for Supercapacitor Application: Novel Potentiodynamic Deposition. *Mater. Res. Bull.* **2013**, *48* (2), 923–928.

(38) Xiang, J. Y.; Tu, J. P.; Zhang, L.; Zhou, Y.; Wang, X. L.; Shi, S. J. Self-Assembled Synthesis of Hierarchical Nanostructured CuO with Various Morphologies and Their

Application as Anodes for Lithium Ion Batteries. *J. Power Sources* **2010**, *195* (1), 313–319.

(39) Jisen, W.; Jinkai, Y.; Jinquan, S.; Ying, B. Synthesis of Copper Oxide Nanomaterials and the Growth Mechanism of Copper Oxide Nanorods. *Mater. Des.* **2004**, *25* (7), 625–629.

(40) Cao, M.; Hu, C.; Wang, Y.; Guo, Y.; Guo, C.; Wang, E. A Controllable Synthetic Route to Cu, Cu2O, and CuO Nanotubes and Nanorods. *Chem. Commun.* **2003**, No. 15, 1884.

(41) Yao, W.-T.; Yu, S.-H.; Zhou, Y.; Jiang, J.; Wu, Q.-S.; Zhang, L.; Jiang, J. Formation of Uniform CuO Nanorods by Spontaneous Aggregation: Selective Synthesis of CuO, Cu_2O, and Cu Nanoparticles by a Solid−Liquid Phase Arc Discharge Process. *J. Phys. Chem. B* **2005**, *109* (29), 14011–14016.

(42) Zarate, R. A.; Hevia, F.; Fuentes, S.; Fuenzalida, V. M.; Zúñiga, A. Novel Route to Synthesize CuO Nanoplatelets. *J. Solid State Chem.* **2007**, *180* (4), 1464–1469.

(43) Bello, A.; Dodoo-Arhin, D.; Makgopa, K.; Fabiane, M.; Manyala, N. Surfactant Assisted Synthesis of Copper Oxide (CuO) Leaf-like Nanostructures for Electrochemical Applications. *Am J Mater Sci* **2014**, *4*, 64–73.

(44) Zhang, J.; Liu, J.; Peng, Q.; Wang, X.; Li, Y. Nearly Monodisperse Cu_2O and CuO Nanospheres: Preparation and Applications for Sensitive Gas Sensors. *Chem. Mater.* **2006**, *18* (4), 867–871.

(45) Shaikh, J. S.; Pawar, R. C.; Moholkar, A. V.; Kim, J. H.; Patil, P. S. CuO–PAA Hybrid Films: Chemical Synthesis and Supercapacitor Behavior. *Appl. Surf. Sci.* **2011**, *257* (9), 4389–4397.

(46) Jiang, X.; Herricks, T.; Xia, Y. CuO Nanowires Can Be Synthesized by Heating Copper Substrates in Air. *Nano Lett.* **2002**, *2* (12), 1333–1338.

(47) Hansen, B. J.; Lu, G.; Chen, J. Direct Oxidation Growth of CuO Nanowires from Copper-Containing Substrates. *J. Nanomater.* **2008**, *2008*, 1–7.

(48) Chen, J. T.; Zhang, F.; Wang, J.; Zhang, G. A.; Miao, B. B.; Fan, X. Y.; Yan, D.; Yan, P. X. CuO Nanowires Synthesized by Thermal Oxidation Route. *J. Alloys Compd.* **2008**, *454* (1–2), 268–273.

(49) Mema, R.; Yuan, L.; Du, Q.; Wang, Y.; Zhou, G. Effect of Surface Stresses on CuO Nanowire Growth in the Thermal Oxidation of Copper. *Chem. Phys. Lett.* **2011**, *512* (1–3), 87–91.

(50) Kaur, M.; Muthe, K. P.; Despande, S. K.; Choudhury, S.; Singh, J. B.; Verma, N.; Gupta, S. K.; Yakhmi, J. V. Growth and Branching of CuO Nanowires by Thermal Oxidation of Copper. *J. Cryst. Growth* **2006**, *289* (2), 670–675.

(51) Xu, C. H.; Woo, C. H.; Shi, S. Q. Formation of CuO Nanowires on Cu Foil. *Chem. Phys. Lett.* **2004**, *399* (1–3), 62–66.

(52) Raksa, P.; Gardchareon, A.; Chairuangsri, T.; Mangkorntong, P.; Mangkorntong, N.; Choopun, S. Ethanol Sensing Properties of CuO Nanowires Prepared by an Oxidation Reaction. *Ceram. Int.* **2009**, *35* (2), 649–652.

(53) Lu, C.; Qi, L.; Yang, J.; Zhang, D.; Wu, N.; Ma, J. Simple Template-Free Solution Route for the Controlled Synthesis of $Cu(OH)_2$ and CuO Nanostructures. *J. Phys. Chem. B* **2004**, *108* (46), 17825–17831.

(54) Wang, W.; Lan, C.; Li, Y.; Hong, K.; Wang, G. A Simple Wet Chemical Route for Large-Scale Synthesis of Cu(OH)2 Nanowires. *Chem. Phys. Lett.* **2002**, *366* (3–4), 220–223.

(55) Wen, X.; Zhang, W.; Yang, S.; Dai, Z. R.; Wang, Z. L. Solution Phase Synthesis of $Cu(OH)_2$ Nanoribbons by Coordination Self-Assembly Using Cu_2S Nanowires as Precursors. *Nano Lett.* **2002**, *2* (12), 1397–1401.

(56) Song, X.; Sun, S.; Zhang, W.; Yu, H.; Fan, W. Synthesis of $Cu(OH)_2$ Nanowires at Aqueous−Organic Interfaces. *J. Phys. Chem. B* **2004**, *108* (17), 5200–5205.

(57) Zhang, P.; Zhang, L.; Zhao, G.; Feng, F. A Highly Sensitive Nonenzymatic Glucose Sensor Based on CuO Nanowires. *Microchim. Acta* **2012**, *176* (3–4), 411–417.

(58) Wang, F.; Richards, V. N.; Shields, S. P.; Buhro, W. E. Kinetics and Mechanisms of Aggregative Nanocrystal Growth. *Chem. Mater.* **2014**, *26* (1), 5–21.

(59) Whitehead, C. B.; Özkar, S.; Finke, R. G. LaMer's 1950 Model of Particle Formation: A Review and Critical Analysis of Its Classical Nucleation and Fluctuation Theory Basis, of Competing Models and Mechanisms for Phase-Changes and Particle Formation, and Then of Its Application to Silver Halide, Semiconductor, Metal, and Metal-Oxide Nanoparticles. *Mater. Adv.* **2021**, *2* (1), 186–235.

(60) Sangwal, K. *Nucleation and Crystal Growth: Metastability of Solutions and Melts*; John Wiley & Sons, Inc.: Hoboken, NJ, USA, 2018.

(61) He, W.; Wen, K.; Niu, Y. *Nanocrystals from Oriented-Attachment for Energy Applications*; SpringerBriefs in Energy; Springer International Publishing: Cham, 2018.

(62) Ribeiro, C.; Lee, E. J. H.; Giraldi, T. R.; Longo, E.; Varela, J. A.; Leite, E. R. Study of Synthesis Variables in the Nanocrystal Growth Behavior of Tin Oxide Processed by Controlled Hydrolysis. *J. Phys. Chem. B* **2004**, *108* (40), 15612–15617.

(63) Ribeiro, C.; Lee, E. J. H.; Longo, E.; Leite, E. R. A Kinetic Model to Describe Nanocrystal Growth by the Oriented Attachment Mechanism. *ChemPhysChem* **2005**, *6* (4), 690–696.

(64) Moldovan, D.; Yamakov, V.; Wolf, D.; Phillpot, S. R. Scaling Behavior of Grain-Rotation-Induced Grain Growth. *Phys. Rev. Lett.* **2002**, *89* (20), 206101.

(65) Leite, E. R.; Giraldi, T. R.; Pontes, F. M.; Longo, E.; Beltran, A.; Andres, J. Crystal Growth in Colloidal Tin Oxide Nanocrystals Induced by Coalescence at Room Temperature. *Appl. Phys. Lett.* **2003**, *83* (8), 1566–1568.

(66) Li, D.; Nielsen, M. H.; Lee, J. R.; Frandsen, C.; Banfield, J. F.; De Yoreo, J. J. Direction-Specific Interactions Control Crystal Growth by Oriented Attachment. *Science* **2012**, *336* (6084), 1014–1018.

(67) Penn, R. L. Kinetics of Oriented Aggregation. *J. Phys. Chem. B* **2004**, *108* (34), 12707–12712.

(68) de Jonge, N.; Houben, L.; Dunin-Borkowski, R. E.; Ross, F. M. Resolution and Aberration Correction in Liquid Cell Transmission Electron Microscopy. *Nat. Rev. Mater.* **2019**, *4* (1), 61–78.

(69) Nielsen, M. H.; Lee, J. R. I.; Hu, Q.; Yong-Jin Han, T.; De Yoreo, J. J. Structural Evolution, Formation Pathways and Energetic Controls during Template-Directed Nucleation of CaCO3. *Faraday Discuss.* **2012**, *159*, 105.

(70) Nielsen, M. H.; Aloni, S.; De Yoreo, J. J. In Situ TEM Imaging of CaCO3 Nucleation Reveals Coexistence of Direct and Indirect Pathways. *Science* **2014**, *345* (6201), 1158–1162.

(71) Liu, Y.; Lin, X.-M.; Sun, Y.; Rajh, T. In Situ Visualization of Self-Assembly of Charged Gold Nanoparticles. *J. Am. Chem. Soc.* **2013**, *135* (10), 3764–3767.

(72) Shi, F.; Li, F.; Ma, Y.; Zheng, F.; Feng, R.; Song, C.; Tao, P.; Shang, W.; Deng, T.; Wu, J. In Situ Transmission Electron Microscopy Study of Nanocrystal Formation for Electrocatalysis. *ChemNanoMat* **2019**, *5* (12), 1439–1455.

(73) Woehl, T. Refocusing *in Situ* Electron Microscopy: Moving beyond Visualization of Nanoparticle Self-Assembly To Gain Practical Insights into Advanced Material Fabrication. *ACS Nano* **2019**, *13* (11), 12272–12279.

(74) Wang, Y.; Peng, X.; Abelson, A.; Zhang, B.-K.; Qian, C.; Ercius, P.; Wang, L.-W.; Law, M.; Zheng, H. In Situ TEM Observation of Neck Formation during Oriented Attachment of PbSe Nanocrystals. *Nano Res.* **2019**, *12* (10), 2549–2553.

(75) Wei, W.; Zhang, H.; Wang, W.; Dong, M.; Nie, M.; Sun, L.; Xu, F. Observing the Growth of Pb_3O_4 Nanocrystals by in Situ Liquid Cell Transmission Electron Microscopy. *ACS Appl. Mater. Interfaces* **2019**, *11* (27), 24478–24484.

(76) Jin, B.; Liu, Z.; Tang, R. Recent Experimental Explorations of Non-Classical Nucleation. *CrystEngComm* **2020**, *22* (24), 4057–4073.

(77) Liu, C.; Ou, Z.; Zhou, S.; Chen, Q. Nonclassical Crystallization Observed by Liquid-Phase Transmission Electron Microscopy. In *ACS Symposium Series*; Zhang, X., Ed.; American Chemical Society: Washington, DC, 2020; Vol. 1358, pp 115–146.

(78) Patel, V. K.; b, S. High-Performance Nanothermite Composites Based on Aloe-Vera-Directed CuO Nanorods. *ACS Appl. Mater. Interfaces* **2013**, *5* (24), 13364–13374.

(79) Sundar, S.; Venkatachalam, G.; Kwon, S. Biosynthesis of Copper Oxide (CuO) Nanowires and Their Use for the Electrochemical Sensing of Dopamine. *Nanomaterials* **2018**, *8* (10), 823.

(80) Zhang, Z.; Tang, Z.; Kotov, N. A.; Glotzer, S. C. Simulations and Analysis of Self-Assembly of CdTe Nanoparticles into Wires and Sheets. *Nano Lett.* **2007**, *7* (6), 1670–1675.

(81) Pradhan, N.; Xu, H.; Peng, X. Colloidal CdSe Quantum Wires by Oriented Attachment. *Nano Lett.* **2006**, *6* (4), 720–724.

(82) O'Sullivan, C.; Gunning, R. D.; Sanyal, A.; Barrett, C. A.; Geaney, H.; Laffir, F. R.; Ahmed, S.; Ryan, K. M. Spontaneous Room Temperature Elongation of CdS and Ag_2S Nanorods via Oriented Attachment. *J. Am. Chem. Soc.* **2009**, *131* (34), 12250–12257.

(83) Polleux, J.; Pinna, N.; Antonietti, M.; Niederberger, M. Growth and Assembly of Crystalline Tungsten Oxide Nanostructures Assisted by Bioligation. *J. Am. Chem. Soc.* **2005**, *127* (44), 15595–15601.

(84) Wang, J.; Li, X.; Teng, C.; Xia, Y.; Xu, J.; Xie, D.; Xiang, L.; Komarneni, S. Ligand-Directed Rapid Formation of Ultralong ZnO Nanowires by Oriented Attachment for UV Photodetectors. *J. Mater. Chem. C* **2016**, *4* (24), 5755–5765.

(85) Ramgir, N.; Datta, N.; Kaur, M.; Kailasaganapathi, S.; Debnath, A. K.; Aswal, D. K.; Gupta, S. K. Metal Oxide Nanowires for Chemiresistive Gas Sensors: Issues, Challenges and Prospects. *Colloids Surf. Physicochem. Eng. Asp.* **2013**, *439*, 101–116.

(86) Shen, G.; Chen, P.-C.; Ryu, K.; Zhou, C. Devices and Chemical Sensing Applications of Metal Oxide Nanowires. *J Mater Chem* **2009**, *19* (7), 828–839.

(87) Zhou, S.; Liu, L.; Lou, S.; Wang, Y.; Chen, X.; Yuan, H.; Hao, Y.; Yuan, R.; Li, N. Room-Temperature Ferromagnetism of Diamagnetically-Doped ZnO Aligned Nanorods Fabricated by Vapor Reaction. *Appl. Phys. A* **2011**, *102* (2), 367–371.

(88) Wang; Song, J.; Summers, C. J.; Ryou, J. H.; Li, P.; Dupuis, R. D.; Wang, Z. L. Density-Controlled Growth of Aligned ZnO Nanowires Sharing a Common Contact: A Simple, Low-Cost, and Mask-Free Technique for Large-Scale Applications. *J. Phys. Chem. B* **2006**, *110* (15), 7720–7724.

(89) Jimenez-Cadena, G.; Comini, E.; Ferroni, M.; Vomiero, A.; Sberveglieri, G. Synthesis of Different ZnO Nanostructures by Modified PVD Process and Potential Use for Dye-Sensitized Solar Cells. *Mater. Chem. Phys.* **2010**, *124* (1), 694–698.

(90) Thangala, J.; Vaddiraju, S.; Malhotra, S.; Chakrapani, V.; Sunkara, M. K. A Hot-Wire Chemical Vapor Deposition (HWCVD) Method for Metal Oxide and Their Alloy Nanowire Arrays. *Thin Solid Films* **2009**, *517* (12), 3600–3605.

(91) Filipič, G.; Cvelbar, U. Copper Oxide Nanowires: A Review of Growth. *Nanotechnology* **2012**, *23* (19), 194001.

(92) Qin, Y.; Li, X.; Wang, F.; Hu, M. Solvothermally Synthesized Tungsten Oxide Nanowires/Nanorods for NO2 Gas Sensor Applications. *J. Alloys Compd.* **2011**, *509* (33), 8401–8406.

(93) Qurashi, A.; Tabet, N.; Faiz, M.; Yamzaki, T. Ultra-Fast Microwave Synthesis of ZnO Nanowires and Their Dynamic Response Toward Hydrogen Gas. *Nanoscale Res. Lett.* **2009**, *4* (8), 948.

(94) Thiagarajan, S.; Sanmugam, A.; Vikraman, D. Facile Methodology of Sol-Gel Synthesis for Metal Oxide Nanostructures. In *Recent Applications in Sol-Gel Synthesis*; Chandra, U., Ed.; InTech, 2017.

(95) Sztaberek, L.; Mabey, H.; Beatrez, W.; Lore, C.; Santulli, A. C.; Koenigsmann, C. Sol–Gel Synthesis of Ruthenium Oxide Nanowires To Enhance Methanol Oxidation in Supported Platinum Nanoparticle Catalysts. *ACS Omega* **2019**, *4* (10), 14226–14233.

(96) Ebelmen. Untersuchungen über die Verbindungen der Borsäure und Kieselsäure mit Aether. *Ann. Chem. Pharm.* **1846**, *57* (3), 319–355.

(97) Danks, A. E.; Hall, S. R.; Schnepp, Z. The Evolution of 'Sol–Gel' Chemistry as a Technique for Materials Synthesis. *Mater. Horiz.* **2016**, *3* (2), 91–112.

(98) Stöber, W.; Fink, A.; Bohn, E. Controlled Growth of Monodisperse Silica Spheres in the Micron Size Range. *J. Colloid Interface Sci.* **1968**, *26* (1), 62–69.

(99) Livage, J.; Henry, M.; Sanchez, C. Sol-Gel Chemistry of Transition Metal Oxides. *Prog. Solid State Chem.* **1988**, *18* (4), 259–341.

(100) Zha, J.; Roggendorf, H. Sol-Gel Science, the Physics and Chemistry of Sol-Gel Processing, Ed. by C. J. Brinker and G. W. Scherer, Academic Press, Boston 1990, Xiv, 908 Pp., Bound?ISBN 0-12-134970-5. *Adv. Mater.* **1991**, *3* (10), 522–522.

(101) Sui, R.; Charpentier, P. Synthesis of Metal Oxide Nanostructures by Direct Sol–Gel Chemistry in Supercritical Fluids. *Chem. Rev.* **2012**, *112* (6), 3057–3082.

(102) Tseng, T. K.; Lin, Y. S.; Chen, Y. J.; Chu, H. A Review of Photocatalysts Prepared by Sol-Gel Method for VOCs Removal. *Int. J. Mol. Sci.* **2010**, *11* (6), 2336–2361.

(103) Mutin, P. H.; Vioux, A. Nonhydrolytic Processing of Oxide-Based Materials: Simple Routes to Control Homogeneity, Morphology, and Nanostructure. *Chem. Mater.* **2009**, *21* (4), 582–596.

(104) Vioux, A. Nonhydrolytic Sol−Gel Routes to Oxides. *Chem. Mater.* **1997**, *9* (11), 2292–2299.

(105) Schubert, U. Chemistry and Fundamentals of the Sol–Gel Process. *Sol-Gel Handb.* **2015**, 1–28.

(106) Foo, K. L.; Hashim, U.; Muhammad, K.; Voon, C. H. Sol–Gel Synthesized Zinc Oxide Nanorods and Their Structural and Optical Investigation for Optoelectronic Application. *Nanoscale Res. Lett.* **2014**, *9* (1), 429.

(107) Ahn, S.-E.; Ji, H. J.; Kim, K.; Kim, G. T.; Bae, C. H.; Park, S. M.; Kim, Y.-K.; Ha, J. S. Origin of the Slow Photo response in an Individual Sol-Gel Synthesized ZnO Nanowire. *Appl. Phys. Lett.* **2007**, *90* (15), 153106.

(108) Woo, K.; Lee, H. J.; Ahn, J.-P.; Park, Y. S. Sol–Gel Mediated Synthesis of Fe2O3 Nanorods. *Adv. Mater.* **2003**, *15* (20), 1761–1764.

(109) Kadhim, I. H.; Abu Hassan, H. Hydrogen Gas Sensing Based on SnO2 Nanostructure Prepared by Sol–Gel Spin Coating Method. *J. Electron. Mater.* **2017**, *46* (3), 1419–1426.

(110) Dhanasekaran, V.; Soundaram, N.; Kim, S.-I.; Chandramohan, R.; Mantha, S.; Saravanakumar, S.; Mahalingam, T. Optical, Electrical and Microstructural Studies of Monoclinic CuO Nanostructures Synthesized by a Sol–Gel Route. *New J. Chem.* **2014**, *38* (6), 2327.

(111) House, J. E. *Principles of Chemical Kinetics*; Academic Press, 2007.

(112) Joesten, R.; Fisher, G. Kinetics of Diffusion-Controlled Mineral Growth in the Christmas Mountains (Texas) Contact Aureole. *GSA Bull.* **1988**, *100* (5), 714–732.

(113) Huang, F.; Zhang, H.; Banfield, J. F. Two-Stage Crystal-Growth Kinetics Observed during Hydrothermal Coarsening of Nanocrystalline ZnS. *Nano Lett.* **2003**, *3* (3), 373–378.

(114) Zhang, J.; Lin, Z.; Lan, Y.; Ren, G.; Chen, D.; Huang, F.; Hong, M. A Multistep Oriented Attachment Kinetics: Coarsening of ZnS Nanoparticle in Concentrated NaOH. *J. Am. Chem. Soc.* **2006**, *128* (39), 12981–12987.

(115) Zhang, J.; Wang, Y.; Zheng, J.; Huang, F.; Chen, D.; Lan, Y.; Ren, G.; Lin, Z.; Wang, C. Oriented Attachment Kinetics for Ligand Capped Nanocrystals: Coarsening of Thiol-PbS Nanoparticles. *J. Phys. Chem. B* **2007**, *111* (6), 1449–1454.

(116) Zhuang, Z.; Zhang, J.; Huang, F.; Wang, Y.; Lin, Z. Pure Multistep Oriented Attachment Growth Kinetics of Surfactant-Free SnO2 Nanocrystals. *Phys. Chem. Chem. Phys.* **2009**, *11* (38), 8516.

(117) Huang, F.; Zhang, H.; Banfield, J. F. The Role of Oriented Attachment Crystal Growth in Hydrothermal Coarsening of Nanocrystalline ZnS. *J. Phys. Chem. B* **2003**, *107* (38), 10470–10475.

(118) Wang, Y.; Zhang, J.; Yang, Y.; Huang, F.; Zheng, J.; Chen, D.; Yan, F.; Lin, Z.; Wang, C. NaOH Concentration Effect on the Oriented Attachment Growth Kinetics of ZnS. *J. Phys. Chem. B* **2007**, *111* (19), 5290–5294.

(119) Lee, E. J. H.; Ribeiro, C.; Longo, E.; Leite, E. R. Growth Kinetics of Tin Oxide Nanocrystals in Colloidal Suspensions under Hydrothermal Conditions. *Chem. Phys.* **2006**, *328* (1–3), 229–235.

(120) Gunning, R. D.; O'Sullivan, C.; Ryan, K. M. A Multi-Rate Kinetic Model for Spontaneous Oriented Attachment of CdS Nanorods. *Phys. Chem. Chem. Phys.* **2010**, *12* (39), 12430–12435.

(121) Zhan, H.; Yang, X.; Wang, C.; Liang, C.; Wu, M. Multiple Growth Stages and Their Kinetic Models of Anatase Nanoparticles under Hydrothermal Conditions. *J. Phys. Chem. C* **2010**, *114* (34), 14461–14466.

(122) Yin, S.; Huang, F.; Zhang, J.; Zheng, J.; Lin, Z. The Effects of Particle Concentration and Surface Charge on the Oriented Attachment Growth Kinetics of CdTe Nanocrystals in H_2O. *J. Phys. Chem. C* **2011**, *115* (21), 10357–10364.

(123) Segets, D.; Hartig, M. A. J.; Gradl, J.; Peukert, W. A Population Balance Model of Quantum Dot Formation: Oriented Growth and Ripening of ZnO. *Chem. Eng. Sci.* **2012**, *70*, 4–13.

(124) Xue, X.; Huang, Y.; Zhuang, Z.; Huang, F.; Lin, Z. Temperature-Sensitive Growth Kinetics and Photoluminescence Properties of CdS Quantum Dots. *CrystEngComm* **2013**, *15* (24), 4963.

(125) Huang, Y.; Zhuang, Z.; Xue, X.; Zheng, J.; Lin, Z. Growth Kinetics Study Revealing the Role of the MPA Capping Ligand on Adjusting the Growth Modes and PL Properties of CdTe QDs. *CrystEngComm* **2014**, *16* (8), 1547–1552.

(126) Wolff, A.; Hetaba, W.; Wißbrock, M.; Löffler, S.; Mill, N.; Eckstädt, K.; Dreyer, A.; Ennen, I.; Sewald, N.; Schattschneider, P.; Hütten, A. Oriented Attachment Explains Cobalt Ferrite Nanoparticle Growth in Bioinspired Syntheses. *Beilstein J. Nanotechnol.* **2014**, *5*, 210–218.

(127) Hazarika, S.; Mohanta, D. Oriented Attachment (OA) Mediated Characteristic Growth of Gd2O3 Nanorods from Nanoparticle Seeds. *J. Rare Earths* **2016**, *34* (2), 158–165.

(128) Chen, Z.; Han, C.; Wang, F.; Gao, C.; Liu, P.; Ding, Y.; Zhang, S.; Yang, M. Precise Control of Water Content on the Growth Kinetics of ZnO Quantum Dots. *J. Cryst. Growth* **2019**, *511*, 65–72.

(129) Dalmaschio, C. J.; Ribeiro, C.; Leite, E. R. Impact of the Colloidal State on the Oriented Attachment Growth Mechanism. *Nanoscale* **2010**, *2* (11), 2336.

(130) Tran, R.; Xu, Z.; Radhakrishnan, B.; Winston, D.; Sun, W.; Persson, K. A.; Ong, S. P. Surface Energies of Elemental Crystals. *Sci. Data* **2016**, *3* (1), 160080.

(131) Lee, A. Y.; Erdemir, D.; Myerson, A. S. Crystals and Crystal Growth. In *Handbook of Industrial Crystallization*; Myerson, A. S., Erdemir, D., Lee, A. Y., Eds.; Cambridge University Press, 2019; pp 32–75.

(132) Martin, J. W.; Doherty, R. D.; Cantor, B. *Stability of Microstructure in Metallic Systems*, 2nd ed.; Cambridge University Press, 1997.

(133) Khan, M. A. S.; Ganguly, B. Can Surface Energy Be a Parameter to Define Morphological Change of Rock-Salt Crystals with Additives? A First Principles Study. *CrystEngComm* **2013**, *15* (14), 2631.

(134) Venables, J. A. *Introduction to Surface and Thin Film Processes*, 1st ed.; Cambridge University Press, 2000.

(135) Chernov, A. A. *Modern Crystallography III*; Cardona, M., Fulde, P., Queisser, H.-J., Series Eds.; Springer Series in Solid-State Sciences; Springer Berlin Heidelberg: Berlin, Heidelberg, 1984; Vol. 36.

(136) Penn, R. L.; Banfield, J. F. Morphology Development and Crystal Growth in Nanocrystalline Aggregates under Hydrothermal Conditions: Insights from Titania. *Geochim. Cosmochim. Acta* **1999**, *63* (10), 1549–1557.

(137) Xiao, J.; Qi, L. Surfactant-Assisted, Shape-Controlled Synthesis of Gold Nanocrystals. *Nanoscale* **2011**, *3* (4), 1383–1396.

(138) Bakshi, M. S. How Surfactants Control Crystal Growth of Nanomaterials. *Cryst. Growth Des.* **2016**, *16* (2), 1104–1133.

(139) *Controlled Nanofabrication: Advances and Applications*, 0 ed.; Ru-Shi, L., Ed.; Jenny Stanford Publishing, 2012.

(140) Jun, Y.; Casula, M. F.; Sim, J.-H.; Kim, S. Y.; Cheon, J.; Alivisatos, A. P. Surfactant-Assisted Elimination of a High Energy Facet as a Means of Controlling the Shapes of TiO2 Nanocrystals. *J. Am. Chem. Soc.* **2003**, *125* (51), 15981–15985.

(141) Dinh, C.-T.; Nguyen, T.-D.; Kleitz, F.; Do, T.-O. Shape-Controlled Synthesis of Highly Crystalline Titania Nanocrystals. *ACS Nano* **2009**, *3* (11), 3737–3743.

(142) Pinna, N.; Niederberger, M. Surfactant-Free Nonaqueous Synthesis of Metal Oxide Nanostructures. *Angew. Chem. Int. Ed.* **2008**, *47* (29), 5292–5304.

(143) Yahiro, J.; Oaki, Y.; Imai, H. Biomimetic Synthesis of Wurtzite ZnO Nanowires Possessing a Mosaic Structure. *Small* **2006**, *2* (10), 1183–1187.

(144) Oaki, Y.; Imai, H. Biomimetic Morphological Design for Manganese Oxide and Cobalt Hydroxide Nanoflakes with a Mosaic Interior. *J Mater Chem* **2007**, *17* (4), 316–321.

(145) Bandyopadhyay, P.; Jana, R.; Bhattacharyya, K.; Lebedev, O. I.; Dutta, U.; Sarkar, U.; Datta, A.; Seikh, M. M. Interaction of a Bioactive Molecule with Surfaces of Nanoscale Transition Metal Oxides: Experimental and Theoretical Studies. *New J. Chem.* **2019**, *43* (42), 16621–16628.

(146) Lombardo, D.; Kiselev, M. A.; Magazù, S.; Calandra, P. Amphiphiles Self-Assembly: Basic Concepts and Future Perspectives of Supramolecular Approaches. *Adv. Condens. Matter Phys.* **2015**, *2015*, 1–22.

(147) Patwardhan, S. V.; Patwardhan, G.; Perry, C. C. Interactions of Biomolecules with Inorganic Materials: Principles, Applications and Future Prospects. *J. Mater. Chem.* **2007**, *17* (28), 2875.

(148) Guajardo-Pacheco, M. J.; Morales-Sánchez, J. E.; González-Hernández, J.; Ruiz, F. Synthesis of Copper Nanoparticles Using Soybeans as a Chelant Agent. *Mater. Lett.* **2010**, *64* (12), 1361–1364.

(149) Gunalan, S.; Sivaraj, R.; Venckatesh, R. Aloe Barbadensis Miller Mediated Green Synthesis of Mono-Disperse Copper Oxide Nanoparticles: Optical Properties. *Spectrochim. Acta. A. Mol. Biomol. Spectrosc.* **2012**, *97*, 1140–1144.

(150) Aher, Y. B.; Jain, G. H.; Patil, G. E.; Savale, A. R.; Ghotekar, S. K.; Pore, D. M.; Pansambal, S. S.; Deshmukh, K. K. Biosynthesis of Copper Oxide Nanoparticles Using Leaves Extract of Leucaena Leucocephala L. and Their Promising Upshot against Diverse Pathogens. *Int. J. Mol. Clin. Microbiol.* **2017**, *7* (1), 776–786.

(151) Chand Mali, S.; Raj, S.; Trivedi, R. Biosynthesis of Copper Oxide Nanoparticles Using Enicostemma Axillare (Lam.) Leaf Extract. *Biochem. Biophys. Rep.* **2019**, *20*, 100699.

(152) Ansilin, S.; Nair, J. K.; Aswathy, C.; Rama, V.; Peter, J.; Persis, J. J. Green Synthesis and Characterisation of Copper Oxide Nanoparticles Using Azadirachta Indica (Neem) Leaf Aqueous Extract. *J. Nanosci. Technol.* **2016**, 221–223.

(153) Asemani, M.; Anarjan, N. Green Synthesis of Copper Oxide Nanoparticles Using Juglans Regia Leaf Extract and Assessment of Their Physico-Chemical and Biological Properties. *Green Process. Synth.* **2019**, *8* (1), 557–567.

(154) ROHIT, G.; SHAKILA, B. A.; GINO, A. K. Synthesis of Copper Oxide Nanoparticles Using Desmodium Gangeticum Aqueous Root Extract. **2015**.

(155) Sivaraj, R.; Rahman, P. K. S. M.; Rajiv, P.; Narendhran, S.; Venckatesh, R. Biosynthesis and Characterization of Acalypha Indica Mediated Copper Oxide Nanoparticles and Evaluation of Its Antimicrobial and Anticancer Activity. *Spectrochim. Acta. A. Mol. Biomol. Spectrosc.* **2014**, *129*, 255–258.

(156) Singh, S.; Kumar, N.; Kumar, M.; Jyoti; Agarwal, A.; Mizaikoff, B. Electrochemical Sensing and Remediation of 4-Nitrophenol Using Bio-Synthesized Copper Oxide Nanoparticles. *Chem. Eng. J.* **2017**, *313*, 283–292.

(157) Barragan, J. T.; Kogikoski Jr, S.; da Silva, E. T.; Kubota, L. T. Insight into the Electro-Oxidation Mechanism of Glucose and Other Carbohydrates by CuO-Based Electrodes. *Anal. Chem.* **2018**, *90* (5), 3357–3365.

(158) Nwanya, A. C.; Ndipingwi, M. M.; Mayedwa, N.; Razanamahandry, L. C.; Ikpo, C. O.; Waryo, T.; Ntwampe, S. K. O.; Malenga, E.; Fosso-Kankeu, E.; Ezema, F. I.; Iwuoha, E. I.; Maaza, M. Maize (Zea Mays L.) Fresh Husk Mediated Biosynthesis of Copper Oxides: Potentials for Pseudo Capacitive Energy Storage. *Electrochimica Acta* **2019**, *301*, 436–448.

(159) Cuevas, R.; Durán, N.; Diez, M. C.; Tortella, G. R.; Rubilar, O. Extracellular Biosynthesis of Copper and Copper Oxide Nanoparticles by *Stereum Hirsutum*, a Native White-Rot Fungus from Chilean Forests. *J. Nanomater.* **2015**, *2015*, 1–7.

(160) Hassan, S. E.-D.; Fouda, A.; Radwan, A. A.; Salem, S. S.; Barghoth, M. G.; Awad, M. A.; Abdo, A. M.; El-Gamal, M. S. Endophytic Actinomycetes Streptomyces Spp Mediated Biosynthesis of Copper Oxide Nanoparticles as a Promising Tool for Biotechnological Applications. *JBIC J. Biol. Inorg. Chem.* **2019**, *24* (3), 377–393.

(161) V Singh, A.; Patil, R.; Anand, A.; Milani, P.; Gade, W. N. Biological Synthesis of Copper Oxide Nano Particles Using Escherichia Coli. *Curr. Nanosci.* **2010**, *6* (4), 365–369.

(162) Reza Ghorbani, H. Biosynthesis of Copper Oxide Nanoparticles Using Extract of E.Coli. *Orient. J. Chem.* **2015**, *31* (1), 515–517.

(163) Gu, H.; Chen, X.; Chen, F.; Zhou, X.; Parsaee, Z. Ultrasound-Assisted Biosynthesis of CuO-NPs Using Brown Alga Cystoseira Trinodis: Characterization, Photocatalytic AOP, DPPH Scavenging and Antibacterial Investigations. *Ultrason. Sonochem.* **2018**, *41*, 109–119.

(164) Fawcett, D.; Verduin, J. J.; Shah, M.; Sharma, S. B.; Poinern, G. E. J. A Review of Current Research into the Biogenic Synthesis of Metal and Metal Oxide Nanoparticles via Marine Algae and Seagrasses. *J. Nanosci.* **2017**, *2017*, 1–15.

(165) Kumar, C. S. *Transmission Electron Microscopy Characterization of Nanomaterials*; Springer Science & Business Media, 2013.

(166) Smith, D. J. Chapter 1. Characterization of Nanomaterials Using Transmission Electron Microscopy. In *Nanoscience & Nanotechnology Series*; Kirkland, A. I., Haigh, S. J., Eds.; Royal Society of Chemistry: Cambridge, 2015; pp 1–29.

(167) Nellist, P. D. The Principles of STEM Imaging. In *Scanning Transmission Electron Microscopy*; Pennycook, S. J., Nellist, P. D., Eds.; Springer New York: New York, NY, 2011; pp 91–115.

(168) Thangala, J.; Chen, Z.; Chin, A.; Ning, C.-Z.; Sunkara, M. K. Phase Transformation Studies of Metal Oxide Nanowires. *Cryst. Growth Des.* **2009**, *9* (7), 3177–3182.

(169) Kuntsche, J.; Horst, J. C.; Bunjes, H. Cryogenic Transmission Electron Microscopy (Cryo-TEM) for Studying the Morphology of Colloidal Drug Delivery Systems. *Int. J. Pharm.* **2011**, *417* (1–2), 120–137.

(170) Liu, L.; Nakouzi, E.; Sushko, M. L.; Schenter, G. K.; Mundy, C. J.; Chun, J.; De Yoreo, J. J. Connecting Energetics to Dynamics in Particle Growth by Oriented Attachment Using Real-Time Observations. *Nat. Commun.* **2020**, *11* (1), 1045.

(171) Zhu, C.; Liang, S.; Song, E.; Zhou, Y.; Wang, W.; Shan, F.; Shi, Y.; Hao, C.; Yin, K.; Zhang, T.; Liu, J.; Zheng, H.; Sun, L. In-Situ Liquid Cell Transmission Electron Microscopy Investigation on Oriented Attachment of Gold Nanoparticles. *Nat. Commun.* **2018**, *9* (1), 421.

(172) Song, M.; Zhou, G.; Lu, N.; Lee, J.; Nakouzi, E.; Wang, H.; Li, D. Oriented Attachment Induces Fivefold Twins by Forming and Decomposing High-Energy Grain Boundaries. *Science* **2020**, *367* (6473), 40–45.

(173) Luo, L.-B.; Wang, X.-H.; Xie, C.; Li, Z.-J.; Lu, R.; Yang, X.-B.; Lu, J. One-Dimensional CuO Nanowire: Synthesis, Electrical, and Optoelectronic Devices Application. *Nanoscale Res. Lett.* **2014**, *9* (1).

(174) Gudiksen, M. S.; Lauhon, L. J.; Wang, J.; Smith, D. C.; Lieber, C. M. Growth of Nanowire Superlattice Structures for Nanoscale Photonics and Electronics. *Nature* **2002**, *415* (6872), 617–620.

(175) Huang, M. H. Room-Temperature Ultraviolet Nanowire Nanolasers. *Science* **2001**, *292* (5523), 1897–1899.

(176) Niederberger, M.; Cölfen, H. Oriented Attachment and Mesocrystals: Non-Classical Crystallization Mechanisms Based on Nanoparticle Assembly. *Phys Chem Chem Phys* **2006**, *8* (28), 3271–3287.

(177) Zheng, H.; Smith, R. K.; Jun, Y. -w.; Kisielowski, C.; Dahmen, U.; Alivisatos, A. P. Observation of Single Colloidal Platinum Nanocrystal Growth Trajectories. *Science* **2009**, *324* (5932), 1309–1312.

(178) Li, Y.; Li, Y.; Huang, L.; Bin, Q.; Lin, Z.; Yang, H.; Cai, Z.; Chen, G. Molecularly Imprinted Fluorescent and Colorimetric Sensor Based on TiO2@Cu(OH)2 Nanoparticle Autocatalysis for Protein Recognition. *J. Mater. Chem. B* **2013**, *1* (9), 1256.

(179) Antonov, L.; Nedeltcheva, D. Resolution of Overlapping UV–Vis Absorption Bands and Quantitative Analysis. *Chem. Soc. Rev.* **2000**, *29* (3), 217–227.

(180) Cui, S.; Liu, X.; Sun, Z.; Du, P. Noble Metal-Free Copper Hydroxide as an Active and Robust Electrocatalyst for Water Oxidation at Weakly Basic PH. *ACS Sustain. Chem. Eng.* **2016**, *4* (5), 2593–2600.

(181) Yu, F.; Li, F.; Zhang, B.; Li, H.; Sun, L. Efficient Electrocatalytic Water Oxidation by a Copper Oxide Thin Film in Borate Buffer. *ACS Catal.* **2015**, *5* (2), 627–630.

(182) Lu, C.; Du, J.; Su, X.-J.; Zhang, M.-T.; Xu, X.; Meyer, T. J.; Chen, Z. Cu (II) Aliphatic Diamine Complexes for Both Heterogeneous and Homogeneous Water Oxidation Catalysis in Basic and Neutral Solutions. *Acs Catal.* **2016**, *6* (1), 77–83.

(183) Durando, M.; Morrish, R.; Muscat, A. J. Kinetics and Mechanism for the Reaction of Hexafluoroacetylacetone with CuO in Supercritical Carbon Dioxide. *J. Am. Chem. Soc.* **2008**, *130* (49), 16659–16668.

(184) Alivisatos, A. P. Perspectives on the Physical Chemistry of Semiconductor Nanocrystals. *J. Phys. Chem.* **1996**, *100* (31), 13226–13239.

(185) Lee, E. J. H.; Ribeiro, C.; Longo, E.; Leite, E. R. Oriented Attachment: An Effective Mechanism in the Formation of Anisotropic Nanocrystals. *J. Phys. Chem. B* **2005**, *109* (44), 20842–20846.

(186) De Yoreo, J. J.; Gilbert, P. U. P. A.; Sommerdijk, N. A. J. M.; Penn, R. L.; Whitelam, S.; Joester, D.; Zhang, H.; Rimer, J. D.; Navrotsky, A.; Banfield, J. F.; Wallace, A. F.;

Michel, F. M.; Meldrum, F. C.; Colfen, H.; Dove, P. M. Crystallization by Particle Attachment in Synthetic, Biogenic, and Geologic Environments. *Science* **2015**, *349* (6247), aaa6760–aaa6760.

(187) De Yoreo, J. J.; Chung, S.; Friddle, R. W. In Situ Atomic Force Microscopy as a Tool for Investigating Interactions and Assembly Dynamics in Biomolecular and Biomineral Systems. *Adv. Funct. Mater.* **2013**, *23* (20), 2525–2538.

(188) Shin, S.-H.; Chung, S.; Sanii, B.; Comolli, L. R.; Bertozzi, C. R.; De Yoreo, J. J. Direct Observation of Kinetic Traps Associated with Structural Transformations Leading to Multiple Pathways of S-Layer Assembly. *Proc. Natl. Acad. Sci.* **2012**, *109* (32), 12968–12973.

(189) Herrmann, J.; Li, P.-N.; Jabbarpour, F.; Chan, A. C. K.; Rajkovic, I.; Matsui, T.; Shapiro, L.; Smit, J.; Weiss, T. M.; Murphy, M. E. P.; Wakatsuki, S. A Bacterial Surface Layer Protein Exploits Multistep Crystallization for Rapid Self-Assembly. *Proc. Natl. Acad. Sci.* **2020**, *117* (1), 388–394.

(190) Madras, G.; McCoy, B. J. Distribution Kinetics Theory of Ostwald Ripening. *J. Chem. Phys.* **2001**, *115* (14), 6699–6706.

(191) Voorhees, P. W. The Theory of Ostwald Ripening. *J. Stat. Phys.* **1985**, *38* (1–2), 231–252.

(192) Baldan, A. Review Progress in Ostwald Ripening Theories and Their Applications to Nickel-Base Superalloys Part I: Ostwald Ripening Theories. *J. Mater. Sci.* **2002**, *37* (11), 2171–2202.

(193) Murphy, C. J.; Jana, N. R. Controlling the Aspect Ratio of Inorganic Nanorods and Nanowires. *Adv. Mater.* **2002**, *14* (1), 80–82.

(194) Maurer, J. H. M.; González-García, L.; Reiser, B.; Kanelidis, I.; Kraus, T. Templated Self-Assembly of Ultrathin Gold Nanowires by Nanoimprinting for Transparent Flexible Electronics. *Nano Lett.* **2016**, *16* (5), 2921–2925.

(195) Nikolaev, K. G.; Ermolenko, Y. E.; Offenhäusser, A.; Ermakov, S. S.; Mourzina, Y. G. Multisensor Systems by Electrochemical Nanowire Assembly for the Analysis of Aqueous Solutions. *Front. Chem.* **2018**, *6*, 256.

(196) Jun, Y.; Casula, M. F.; Sim, J.-H.; Kim, S. Y.; Cheon, J.; Alivisatos, A. P. Surfactant-Assisted Elimination of a High Energy Facet as a Means of Controlling the Shapes of TiO_2 Nanocrystals. *J. Am. Chem. Soc.* **2003**, *125* (51), 15981–15985.

(197) Ishikawa, K. *Guide to Quality Control*; New York : Asian productivity organization, 1982.

(198) Lee, D. K.; In, J.; Lee, S. Standard Deviation and Standard Error of the Mean. *Korean J. Anesthesiol.* **2015**, *68* (3), 220.

(199) Bevington, P. R.; Robinson, D. K. *Data Reduction and Error Analysis for the Physical Sciences*, 3rd ed.; McGraw-Hill: Boston, 2003.

(200) Pathiraja, G.; Yarbrough, R.; Rathnayake, H. Fabrication of Ultrathin CuO Nanowires Augmenting Oriented Attachment Crystal Growth Directed Self-Assembly of Cu(OH)2 Colloidal Nanocrystals. *Nanoscale Adv* **2020**.

(201) Brinker, C. J.; Scherer, G. W. *Sol-Gel Science: The Physics and Chemistry of Sol-Gel Processing*; Academic press, 2013.

(202) Oswald, H. R.; Reller, A.; Schmalle, H. W.; Dubler, E. Structure of Copper(II) Hydroxide, Cu(OH)2. *Acta Crystallogr. C* **1990**, *46* (12), 2279–2284.

(203) Liao, H.-G.; Cui, L.; Whitelam, S.; Zheng, H. Real-Time Imaging of Pt3Fe Nanorod Growth in Solution. *Science* **2012**, *336* (6084), 1011–1014.

(204) Brichtová, E. Studies on the Physical Stability of a C-Terminally Amidated Variant of GLP-1, University of Cambridge, 2019.

(205) Morris, A. M.; Watzky, M. A.; Finke, R. G. Protein Aggregation Kinetics, Mechanism, and Curve-Fitting: A Review of the Literature. *Biochim. Biophys. Acta BBA - Proteins Proteomics* **2009**, *1794* (3), 375–397.

(206) Almeida, Z. L.; Brito, R. M. M. Structure and Aggregation Mechanisms in Amyloids. *Molecules* **2020**, *25* (5), 1195.

(207) Schreck, J. S.; Yuan, J.-M. A Kinetic Study of Amyloid Formation: Fibril Growth and Length Distributions. *J. Phys. Chem. B* **2013**, *117* (21), 6574–6583.

(208) Bullen, C.; Zijlstra, P.; Bakker, E.; Gu, M.; Raston, C. Chemical Kinetics of Gold Nanorod Growth in Aqueous CTAB Solutions. *Cryst. Growth Des.* **2011**, *11* (8), 3375–3380.

(209) Huang, F.; Banfield, J. F. Size-Dependent Phase Transformation Kinetics in Nanocrystalline ZnS. *J. Am. Chem. Soc.* **2005**, *127* (12), 4523–4529.

(210) Noblet, T.; Dreesen, L.; Hottechamps, J.; Humbert, C. A Global Method for Handling Fluorescence Spectra at High Concentration Derived from the Competition between Emission and Absorption of Colloidal CdTe Quantum Dots. *Phys. Chem. Chem. Phys.* **2017**, *19* (39), 26559–26565.

(211) Garnett, E.; Mai, L.; Yang, P. Introduction: 1D Nanomaterials/Nanowires. *Chem. Rev.* **2019**, *119* (15), 8955–8957.

(212) Puntes, V. F.; Zanchet, D.; Erdonmez, C. K.; Alivisatos, A. P. Synthesis of Hcp-Co Nanodisks. *J. Am. Chem. Soc.* **2002**, *124* (43), 12874–12880.

(213) Sellschopp, K.; Heckel, W.; Gäding, J.; Schröter, C. J.; Hensel, A.; Vossmeyer, T.; Weller, H.; Müller, S.; Vonbun-Feldbauer, G. B. Shape-Controlling Effects of Hydrohalic and Carboxylic Acids in TiO_2 Nanoparticle Synthesis. *J. Chem. Phys.* **2020**, *152* (6), 064702.

(214) Ni, C.; Hassan, P. A.; Kaler, E. W. Structural Characteristics and Growth of Pentagonal Silver Nanorods Prepared by a Surfactant Method. *Langmuir* **2005**, *21* (8), 3334–3337.

(215) Sun, S.; Zhang, X.; Yang, Q.; Liang, S.; Zhang, X.; Yang, Z. Cuprous Oxide (Cu2O) Crystals with Tailored Architectures: A Comprehensive Review on Synthesis,

Fundamental Properties, Functional Modifications and Applications. *Prog. Mater. Sci.* **2018**, *96*, 111–173.

(216) Halder, A.; Ravishankar, N. Ultrafine Single-Crystalline Gold Nanowire Arrays by Oriented Attachment. *Adv. Mater.* **2007**, *19* (14), 1854–1858.

(217) Murphy, C. J.; Sau, T. K.; Gole, A. M.; Orendorff, C. J.; Gao, J.; Gou, L.; Hunyadi, S. E.; Li, T. Anisotropic Metal Nanoparticles: Synthesis, Assembly, and Optical Applications. *J. Phys. Chem. B* **2005**, *109* (29), 13857–13870.

(218) Dupin, J.-C.; Gonbeau, D.; Vinatier, P.; Levasseur, A. Systematic XPS Studies of Metal Oxides, Hydroxides and Peroxides. *Phys. Chem. Chem. Phys.* **2000**, *2* (6), 1319–1324.

(219) Derenne, A.; Claessens, T.; Conus, C.; Goormaghtigh, E. Infrared Spectroscopy of Membrane Lipids. In *Encyclopedia of Biophysics*; Roberts, G. C. K., Ed.; Springer Berlin Heidelberg: Berlin, Heidelberg, 2013; pp 1074–1081.

(220) Pramanik, A.; Maiti, S.; Mahanty, S. Metal Hydroxides as a Conversion Electrode for Lithium-Ion Batteries: A Case Study with a $Cu(OH)_2$ Nanoflower Array. *J Mater Chem A* **2014**, *2* (43), 18515–18522.

(221) Wang, L.; Nancollas, G. H. Calcium Orthophosphates: Crystallization and Dissolution. *Chem. Rev.* **2008**, *108* (11), 4628–4669.

APPENDIX A: SINGLE GAUSS PEAK FITTING AT DIFFERENT TIME INTERVALS BY MAINTAINING THE 0.999 OF PRECISION REGRESSION COEFFICIENT

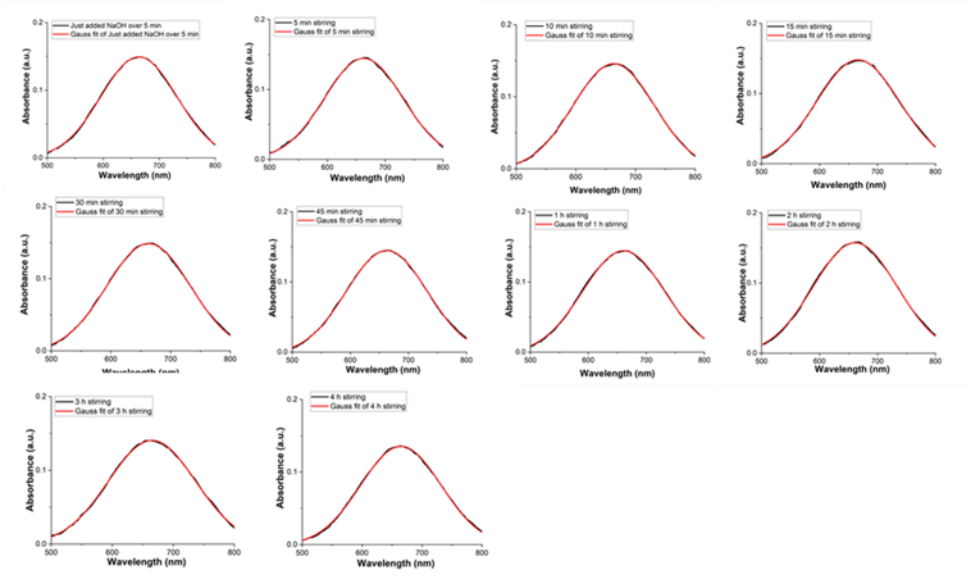

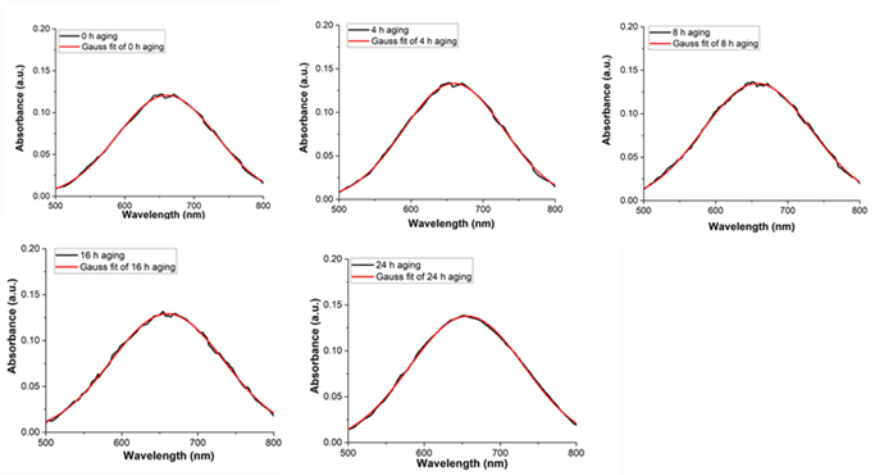

APPENDIX B: GAUSSIAN DISTRIBUTION FITTING OF 150 INDIVIDUAL NWS LENGTH MEASUREMENTS (THREE REPLICATES INCLUDING 50 INDIVIDUAL NANOWIRES IN EACH REPLICATE) AT (A) JUST ADDED NAOH OVER 5 MIN (B) 5 MIN (C) 10 MIN (D) 15 MIN (E) 30 MIN (F) 45 MIN (G) 1 HOUR (H) 1½ HOURS (I) 2 HOURS (J) 3 HOURS (K) 3½ HOURS (L) 4 HOURS (M) 4½ HOURS (N) 5½ HOURS (O) 6 HOURS STIRRING TIME INTERVALS

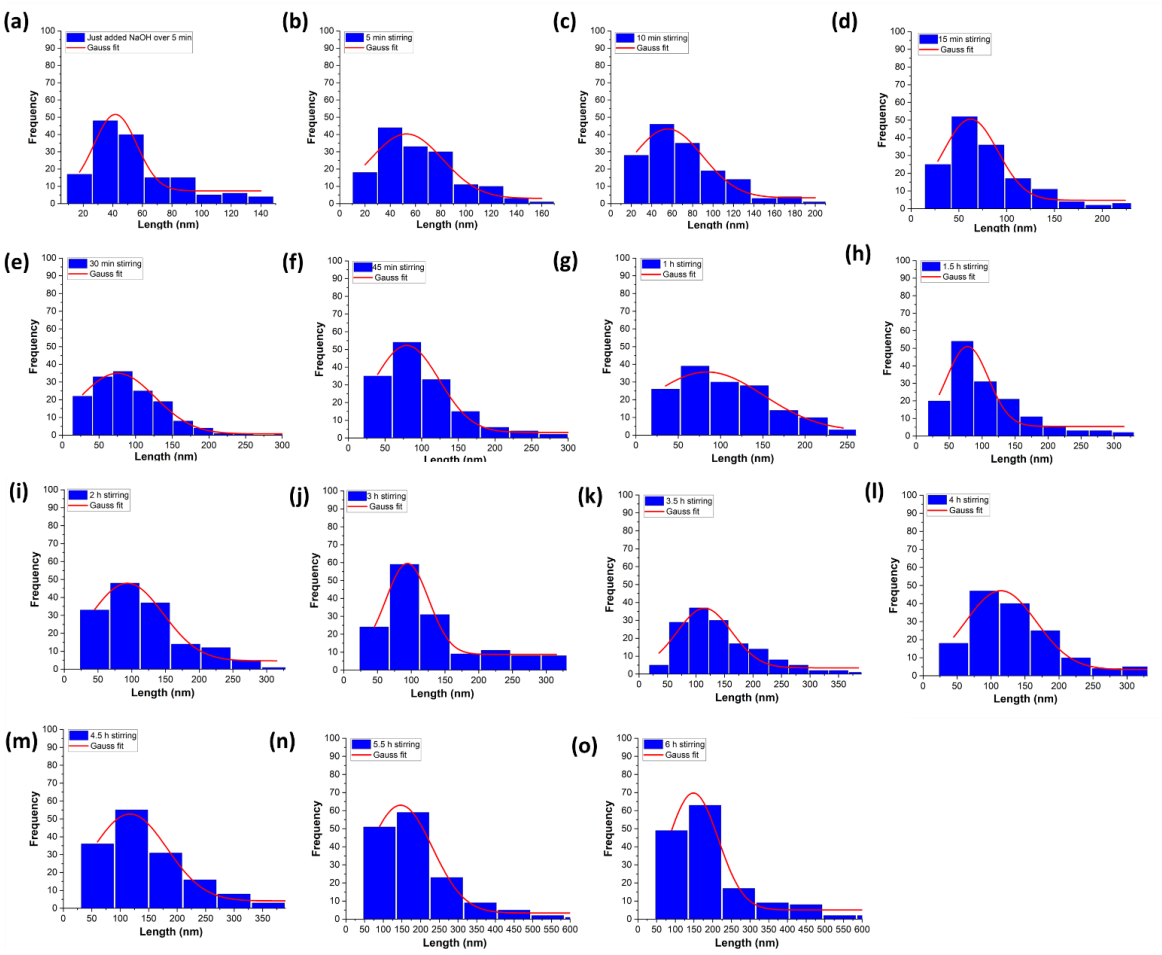

APPENDIX C: GAUSSIAN DISTRIBUTION FITTING OF 150 INDIVIDUAL NWS LENGTH MEASUREMENTS (THREE REPLICATES INCLUDING 50 INDIVIDUAL NANOWIRES IN EACH REPLICATE) AT (A) 4 HOURS (B) 8 HOURS (C) 10 HOURS (D) 12 HOURS (E) 14 HOURS (F) 16 HOURS (G) 24 HOURS AGING TIME INTERVALS

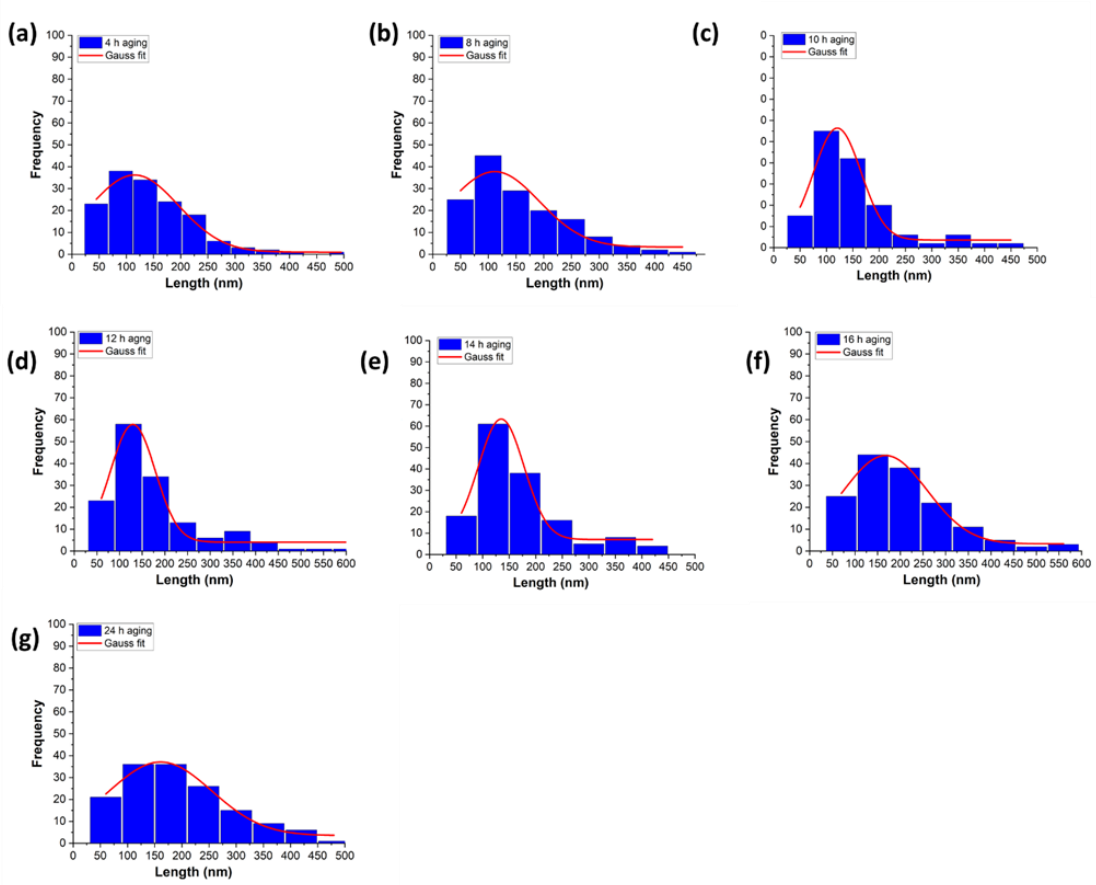

APPENDIX D: SINGLE GAUSS PEAK FITTING AT DIFFERENT TIME INTERVALS BY MAINTAINING THE 0.999 OF PRECISION REGRESSION COEFFICIENT